

ENERGETICS OF CONTROL MOMENT GYROSCOPES
IN ROBOTIC JOINT ACTUATION

A Dissertation

Presented to the Faculty of the Graduate School
of Cornell University

In Partial Fulfillment of the Requirements for the Degree of
Doctor of Philosophy

by

Daniel Brown

May 2009

© 2009 Daniel Brown

ENERGETICS OF CONTROL MOMENT GYROSCOPES IN ROBOTIC JOINT ACTUATION

Daniel Brown, Ph. D.

Cornell University 2009

Control moment gyros (CMGs) are an energy-efficient means of reactionless actuation currently used for attitude control in some spacecraft. In this work, CMGs are compared to direct-drive actuation for robotic applications. Torque, power, and energy of the gimbal motor are calculated using principles of angular momentum and virtual power.

Scissored-pair CMGs produce output torque along the joint axis, facilitating comparison with joint motors. A mechanical coupling enforcing scissored-pair symmetry eliminates undesirable gyroscopic reaction torques and accompanying power costs while simplifying analysis. Strictly controlling CMG rotor speed doubles the CMGs' energy costs, whereas implementing minimal rotor speed control while assuming constant rotor speed reduces the energy costs without compromising the analyses. A single-link robot actuated with scissored-pair CMGs uses the same energy as direct drive for a large range of gimbal inertias and maximum gimbal angles. The transverse rate of the robot base does not affect this result if angular momentum is conserved about the joint axis.

The equations of motion for an n-link robot with CMGs are presented in a recursive form. A two-link robot with orthogonal joint axes and axisymmetric bodies reduces to two, independent, single-link robots. In contrast, a two-link robot with parallel joint axes favors CMGs when the joints rotate with opposite sign, e.g. reaching motions. Direct drive is preferred when the joints act in unison, e.g. throwing motions. Conceptually, CMGs and direct drive may be analyzed as idealized body and

joint torques, respectively. The mappings from actuator torques and velocities to generalized torques and velocities explain differences in power cost between the two actuation methods. A proposed power-optimal robot includes both types of actuation. The optimal distribution of joint and body torques for two- and three-link planar robots is calculated and applied to a three-link robot tracing a closed triangle. The combined actuation method easily outperforms the others in a Monte Carlo simulation. A planar robot with joint motors and CMGs currently in development illustrates the design of a CMG-actuated robot.

BIOGRAPHICAL SKETCH

Daniel Brown received a Bachelor of Science with University Honors degree from Brigham Young University, Magna Cum Laude, in August 2004. He majored in Mechanical Engineering with a minor in Mathematics. His Honors thesis was titled *Testing Performance Characteristics of Layered Compliant Centrifugal Clutches*. He was granted a Master of Science degree by Cornell University in Mechanical Engineering in January 2008.

ACKNOWLEDGMENTS

The author thanks his family, and especially his wife Eliza, for supporting his education. He is also grateful to his advisor, Dr. Mason Peck, for providing a fascinating area of research, maintaining a focus on the final dissertation, and exploring the implications of the results of this research. Dr. Brown enjoyed discussing angular momentum of robots with Professor Moon and is grateful for Professor Ruina's insights on negative work. He appreciates the help, critical analysis, and enthusiasm of fellow graduate student Michele Carpenter. Ian Livingston and Albert Soto worked extensively on the testbed, motivating both the work on CMG control and the testbed example. Justin Fishbone greatly assisted with the three-link robot simulations. The author acknowledges his funding sources: Cornell University, the National Science Foundation through the Integrative Graduate Education and Research Traineeship, and the Mechanical and Aerospace Engineering Department.

TABLE OF CONTENTS

BIOGRAPHICAL SKETCH.....	iii
ACKNOWLEDGMENTS.....	iv
TABLE OF CONTENTS.....	v
LIST OF FIGURES.....	vii
LIST OF TABLES.....	viii
LIST OF SYMBOLS.....	ix
CHAPTER I. Introduction.....	11
CHAPTER II. CMG Dynamics.....	16
A. Single CMG.....	17
B. Scissored-Pair CMGs.....	21
1. Scissored Pair Analysis.....	24
2. Scissored Pair Simulations.....	33
3. Scissored Pair Conclusions.....	36
CHAPTER III. Analysis and Control of Rotor Speed.....	37
A. Energy cost of constant-speed rotor control.....	39
B. Zero rotor torque.....	41
1. Gimbal torque.....	41
2. CMG output torque.....	42
3. Change in rotor speed.....	42
4. Error in spacecraft rate.....	43
5. Rotor speed conclusions.....	44
C. Control Laws for Single-Link Robot.....	45
D. Rotor Speed Conclusions.....	53
CHAPTER IV. Single-Link Robot Arm.....	54
E. Single-Link Analysis.....	54
1. Joint-torque-driven robot.....	54
2. CMG-driven robot.....	55
3. Joint-motor and CMG power.....	56
F. Sizing CMGs in a Scissored Pair.....	57
4. Gimbal torque and torque amplification.....	60
5. Gimbal acceleration.....	64
6. Power contributors.....	64
G. Single-Link Simulations.....	67
1. Trajectory generation.....	68
2. Gimbal inertia and maximum gimbal angle.....	69
3. Transverse Rate.....	71
CHAPTER V. Two-Link Robot Arm.....	75
A. Multilink Robot Dynamics.....	76
1. Joint motor actuation.....	78
2. CMG actuated robot.....	80
A. Two Link Simulations.....	82
1. Link rate and CMG size.....	82
2. Orthogonal joint axes.....	84
3. Parallel joint axes.....	85
CHAPTER VI. Energetics of Robot Actuation Using Joint and Body Torques.....	87
A. Equations of Motion and Power.....	89
4. Torques.....	90
5. Angular Velocity.....	93
6. Power.....	93

7. Energy.....	98
B. Simulations.....	99
8. Two-link robot.....	99
9. Three-Link Robot.....	101
C. Discussion.....	105
CHAPTER VII. Case Study: CMG Testbed.....	107
A. Requirements.....	108
B. Design.....	111
C. Conclusions.....	114
CHAPTER VIII. Conclusion.....	116
Appendix A. Summary of Key Equations.....	122

LIST OF FIGURES

Figure 1. Free-body diagram of single-link robot.	12
Figure 2. Brennan’s gyroscope for monorail.	14
Figure 3. Reaction wheel and CMG principals of operation.	17
Figure 4. CMG vectors and scalars defined.	20
Figure 5. Geared scissored pair	21
Figure 6. Scissored-pair kinematics.	24
Figure 7. Applied torque on a scissored pair.	25
Figure 8. Nondimensional power of scissored pairs.	28
Figure 9. Scissored-pair array momentum cube.	30
Figure 10. Commanded spacecraft angle, rate, and acceleration.	32
Figure 11. Rotor speed constant in N frame.	37
Figure 12. Single-link body controlled by gimbal angle.	45
Figure 13. Valid single-link robot configurations in determining the bound on gimbal rate.	55
Figure 14. Maximum robot angular velocity vs. robot inertia under limited gimbal torque.	58
Figure 15. Relative error in \dot{P}_{rel}	62
Figure 16. Joint trajectory.	64
Figure 17. Gimbal inertia and maximum gimbal angle effect on CMG energy use. ...	65
Figure 18. Transverse rate.	67
Figure 19. Energy ratio plotted against transverse rate.	68
Figure 20. Joint topologies. a) Orthogonal joint axes. b) Parallel joint axes.	70
Figure 21. Free-body diagram of a two-link robot. a. Joint torque. b. Body torque. ...	71
Figure 22. Code structure for n -link robot with joint motors showing recursive dependence.	73
Figure 23. Performance of CMGs on robot arm with orthogonal joint axes.	80
Figure 24. Joint-angle command product as an indicator of performance for parallel joint axes.	81
Figure 25. The total power cost as a function of the local joint power.	92
Figure 26. The difference in energy used by joint torques and body torques.	95
Figure 27. Benefits of combined actuation for two-link robot.	96
Figure 28. The closed path followed by the robot.	97
Figure 29. Energy cost of different actuation methods.	99
Figure 30. Robot built by Cornell CMG team.	101
Figure 31. Two links mechanically assembled.	104
Figure 32. Front view of testbed link.	104
Figure 33. Rotor sizing for testbed.	106
Figure 34. Joint and gimbal angle trajectories for testbed simulation.	108
Figure 35. Testbed torques.	109

LIST OF TABLES

Table 1. Maximum torque and power for geared and independent scissored pairs.	35
Table 2. Parameters for single-link simulation.....	70
Table 3. Parameter value ranges for two-link simulations.	83
Table 4. Contrasting joint-torque and body-torque actuation.	95
Table 5. Parameters used for the two-link simulations. The links are identical. Inertia is taken about the center of mass.	99
Table 6. Optimal distribution between joint and body torques.	103
Table 7. Three-link robot results for Monte Carlo simulation.	104
Table 8. Testbed requirements	108
Table 9. Physical parameters inherited from the CMG team. CMG inertia is half the inertia of the scissored pair.	111
Table 10. Robot trajectory parameters.	113
Table 11. Summary of design tools.	117
Table 12. Pros and cons of CMG-driven robotic joints.....	119

LIST OF SYMBOLS

Vectors

\mathbf{H}_x	Angular momentum of body x , including actuator momentum where applicable, taken about its center of mass or its joint axis as indicated
$\boldsymbol{\omega}^{X/Y}$	Angular velocity of frame X with respect to frame Y
\mathbf{h}_r	Approximate angular momentum, $\mathbf{I}_r \cdot \boldsymbol{\omega}^{R/G}$
$\boldsymbol{\tau}_x$	Torque produced by actuator x
\mathbf{r}_i	Body-fixed location of the i th link's center of mass
\mathbf{R}_i	Inertial location of the i th link's center of mass
\mathbf{v}_i	Inertial velocity of the i th link's center of mass
\mathbf{a}_i	Inertial acceleration of the i th link's center of mass
$\hat{\mathbf{h}}$	Direction of rotor's spin axis
$\hat{\mathbf{g}}$	Direction of the gimbal axis
$\hat{\mathbf{t}}$	Direction of desired output torque; along the joint axis for revolute joints
$\hat{\mathbf{n}}$	Unit vector normal to $\hat{\mathbf{t}}$ and $\hat{\mathbf{g}}$

Dyadics

\mathbf{I}_x	Inertia of body x about its center of mass or an inertially fixed point on the joint axis if indicated, including actuator inertia where applicable
$\mathbf{1}$	Unit dyadic

Scalars

I_x	Inertia of body or component x about a specified axis; about the joint axis if not indicated for a general body or independent of frame for \mathbf{I}_{cmg} .
h_r	Magnitude of the approximate rotor angular momentum, $\mathbf{h}_r \cdot \hat{\mathbf{h}}$
ϕ	Gimbal angle
α	Angle between $\boldsymbol{\omega}^{X/Y}$ and $\hat{\mathbf{t}}$ in the plane perpendicular to $\hat{\mathbf{g}}$
k_{OA}	Output-axis stiffness
P	Power
\tilde{P}	Non-dimensional power to compare geared and independent scissored pairs
\tilde{P}	Non-dimensional power to compare joint motors and CMGs
E	Energy
θ	Joint angle
Ω	Rotor speed
K	Proportional control gain

Reference frames

N	Newtonian (inertial)
B	Body fixed
G	Gimbal fixed
R	Rotor fixed

Subscripts

<i>g</i>	Gimbal
<i>r</i>	Rotor
<i>sp</i>	Scissored-pair CMG
<i>ind</i>	Independent CMGs in a scissored-pair
<i>cmg</i>	CMG
<i>c</i>	CMG-driven robot link (when a distinction is required, as for \mathbf{H}_c vs. \mathbf{H}_{cmg})
<i>b</i>	Body or link
<i>j</i>	Joint-motor
<i>sc</i>	Spacecraft
<i>rel</i>	Relative to joint-torque actuated robot, as in $P_{rel} = P_{cmg}/P_j$
<i>i,k,m</i>	Indexing variables

Derivatives

\dot{x}	Time derivative of the scalar x
$\frac{^Y d}{dt}(\mathbf{x})$	Time derivative of the vector \mathbf{x} taken in frame Y, $\frac{^Y d}{dt}(\mathbf{x})$

CHAPTER I. INTRODUCTION

Attitude control of satellites may be accomplished with internal momentum control when external torques such as those imparted by the gravity gradient, magnetic torquers, or thrusters are inappropriate for the mission requirements. Control moment gyroscopes (CMGs) provide internal momentum for attitude control without expending propellant. Thus they contribute to reduced launch mass and longer spacecraft life. CMGs have important flight heritage controlling large space structures such as Skylab, ISS, and MIR, all of which demand very high torques. CMG's ability to produce large torques in a small package also has applications for smaller satellites with greater agility [*Lappas et al.*, 2005; *Lappas et al.*, 2002; *Wie et al.*, 2002]. Recently smaller CMGs for use on small satellites have been explored [*Lappas et al.*, 2002; *Wie et al.*, 2002]. This research aims to encourage further development of small CMGs by highlighting their potential application to robotics. The primary motivation for this study is the prospect of using CMGs for reactionless actuation to reduce or eliminate the disturbances imparted by traditional joint motors and reduce the associated demands on the spacecraft attitude control system [*Carpenter and Peck*, in review].

The motion of a robot arm in space imparts reaction forces and torques onto the spacecraft base, resulting in nonlinear coupling between the base motion and the robot motion. These effects become more pronounced as the size of the robot increases relative to the base and as robot accelerations increase. When the coupling between the robot and base spacecraft is small, control schemes used for terrestrially based robot arms may be used (see, e.g., [*Murray et al.*, 1994; *Craig*, 2005]). Other alternative control schemes include compensating for the robot motion with the spacecraft thrusters and attitude controller [*Longman et al.*, 1987] or path planning of

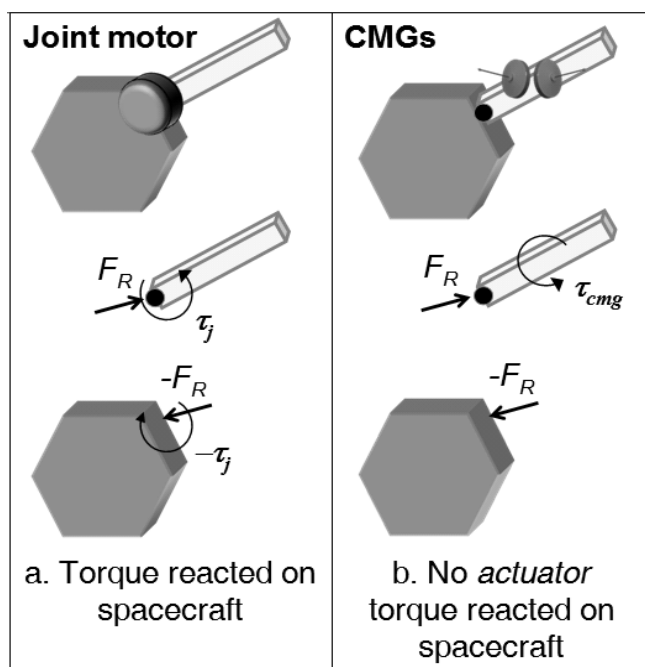


Figure 1. Free-body diagram of single-link robot.

a. Joint-motor torque is reacted onto the base. b. Reactionless body torque moves the robot arm without reacting a torque onto the base. Motion of the robot's center of mass may cause other constraint forces to react against the base.

both the robot and the spacecraft [Nakamura and Mukherjee, 1991]. For a recent review of dynamics and control of free-flying robots in space, see [Moosavian and Papadopoulos, 2007].

An alternative approach is to reduce or eliminate the coupling between the spacecraft and the robot through reactionless actuation. In this paper, robotic actuation that does not impart a torque about the joint axis is termed reactionless actuation. A reactionless robot helps decouple the attitude control system (ACS) from the dynamics of the robotic arm. In Figure 1a, the joint motor creates a torque between the robot and spacecraft that increases demands on the ACS. In contrast, the CMG-driven robot in Figure 1b eliminates the torque coupling about the joint axis. With reactionless actuation, system-level pointing accuracy can be improved by reducing the known

disturbances created by a robotic arm. For such a configuration, rapid robotic movements do not impart low-frequency disturbances that might excite structural vibrations. Furthermore, the agility required of a specific subsystem need not be applied to the satellite as a whole. Reaction wheel assemblies (RWAs), clever gear design, and CMGs are all possible reactionless actuators [Billing-Ross and Wilson, 1988]. A RWA-driven robot, such as the one described in [Carpenter and Peck, 2008; Osuka et al., 1994], can be energetically costly as compared to CMGs [Carpenter and Peck, 2008]. The work in [Carpenter and Peck, in review] demonstrates the reduced reaction torques on the spacecraft from the robot when CMGs are used in place of direct drive motors for joint actuation. Other relevant work in the literature include a proposed bifocal relay telescope that uses CMG attitude control on one member, and connects the other member with a joint motor [Romano and Agrawal, 2004]. CMGs have also been proposed for vibration and slew control of a large truss [Yang et al., 1995]. Comparisons of RWAs and CMGs have previously shown the power benefits of using CMGs, both in attitude control and specifically for robotic applications [Peck, 2005; Van Riper and Liden, 1971]. A comparison of CMGs with joint motors has not been previously published.

Although the actuator reaction torques reflected onto the spacecraft through the joint axis are eliminated with reactionless actuation, the reaction forces and torques attributable to the motion of the robot arm from D'Alembert's principle are not (F_R in Figure 1). Mitigating vibrations from the rapidly spinning rotors adds complexity to the design of CMGs. Friction losses may make CMGs an inefficient choice for a generally quiescent system. Furthermore, reactionless actuators have much greater restrictions on the end-effector forces and torques than typical joint motors because persistent torques will saturate both and CMGs. Therefore, the pros and cons of

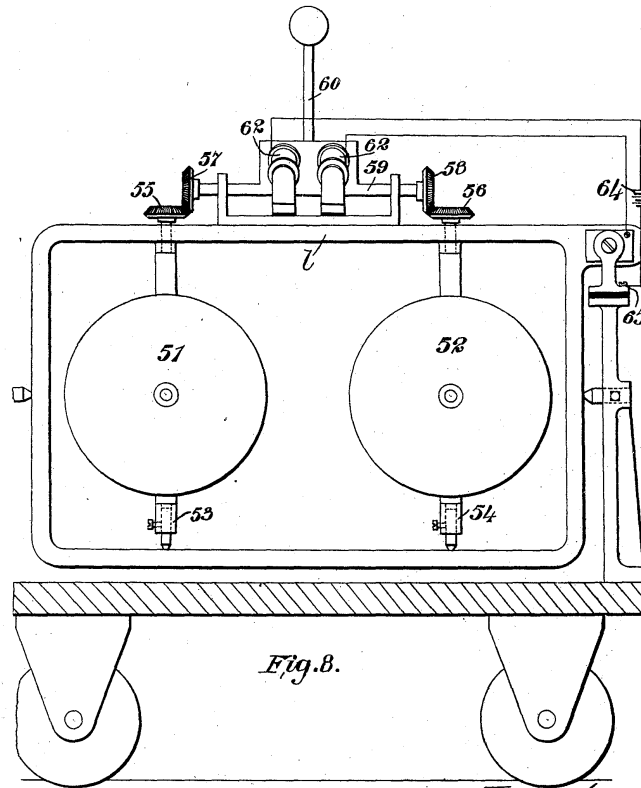


Figure 2. Brennan's gyroscope for monorail.

Gearing between the two rotors directs the gyroscopic torque along the axis of the train, righting the train when tipping, from [Brennan, 1905].

reactionless actuation must be weighed against the pros and cons of traditional joint actuation in choosing robot-arm architectures for specific applications.

Scissored pairs of CMGs, also referred to as V-gyros or twin-gyros [Havill and Ratcliff, 1964] have been suggested for CMG-actuated robots [Carpenter and Peck, 2008]. Scissored-pair CMGs were introduced over a century ago. Brennan used two counter-rotating flywheels with gearing between their gimbals to provide symmetric stabilization of a monorail vehicle around left or right turns [Brennan, 1905; Brennan, 1903] (Figure 2). The Skylab-era Astronaut Maneuvering Research Vehicle used scissored pairs for attitude control of astronauts during extravehicular activities [Cunningham and Driskill, 1972; Murtagh et al., 1974]. These devices have also been

studied as gyrodampers of large space structures [Yang *et al.*, 1995; Aubrun and Margulies, 1979]. Scissored-pair CMGs could also be used to rapidly maneuver a payload with less power than rapidly maneuvering the entire spacecraft [Peck *et al.*, 2005].

This dissertation is organized as follows. CHAPTER II reviews CMG dynamics and contributes an analysis of the power benefits of mechanically connecting a scissored pair. CHAPTER III provides new results on the energy costs of using a constant speed rotor. In CHAPTER IV, CMGs are compared to joint motors in terms of power used during a given motion of a single-link robot. CHAPTER V introduces the dynamics of an n -link robot and compares joint-motor and CMG power for two-link robots. CHAPTER VI generalizes the results of CHAPTER V to draw parallels with a broad class of actuators and includes results for a robot with both joint- and body-torque actuators. CHAPTER VI describes how this work contributes to the design of a planar testbed of a CMG-driven robot arm.

CHAPTER II. CMG DYNAMICS

CMGs belong to a broader class of actuators that use momentum to control the attitude or position of a body. Simply stated, a spinning body resists change in both the magnitude and the direction of spin, i.e., the change in angular momentum is equal to the applied moments. The embedded momentum of a spinning rotor mounted on a body can be used to produce an internal torque that causes the body to rotate in such a way that the net body-plus-rotor angular momentum stays constant. A body that uses momentum to control orientation can reorient without propellant and without changing its net angular momentum, valuable features in spacecraft applications. Typically either a fixed-axis, variable-speed rotor (reaction wheel) or a gimbaled-axis, constant-speed rotor (CMG), or both (including variable-speed CMGs [*Schaub et al.*, 1998]) provide the momentum. Linear momentum actuators have also been considered for controlling micron-scale systems [*Koh et al.*, 2002] but are not considered here.

A reaction wheel assembly (RWA) governs its momentum by changing only its rotor speed. The spin axis is fixed to the satellite. The approximate energy cost of using an RWA of inertia I_r is the change in the kinetic energy of the rotor from the initial to final wheel speeds.

$$\Delta E_r = \frac{1}{2} I_r (\omega_2^2 - \omega_1^2) \quad (1)$$

The initial and final speeds of the rotor (ω_1, ω_2) are taken relative to an inertial reference frame. Even if RW efficiency is improved by recovering some of the energy stored in the rotor, maximum power requirements limit the torque that may be applied by the reaction wheel. In spite of the high energy cost, reaction wheels have been used extensively due to their simplicity, reliability, and strong flight heritage. In contrast, the CMG uses a constant-speed rotor with angular momentum \mathbf{h}_r , rotated about a

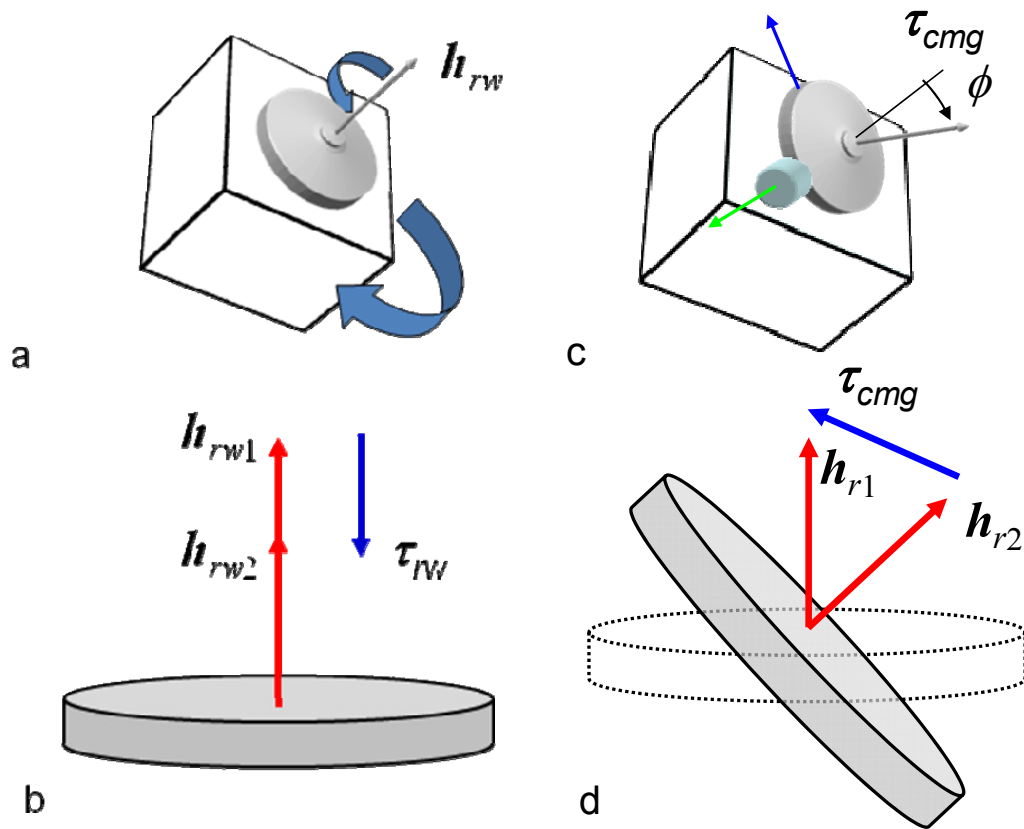


Figure 3. Reaction wheel and CMG principles of operation.

a. Torque on the reaction wheel in one direction produces a torque on the satellite in the opposite direction. b. The reaction wheel torque is generated by changing the speed of the rotor. c. Rotation of the gimbal causes a torque on the satellite perpendicular to the gimbal torque and the rotor momentum. d. CMG torque is generated by changing the direction of the rotor's angular momentum vector.

gimbal axis to change the angular momentum and produce a torque, τ_{cmg} , as shown in Figure 4. Its rotor's kinetic energy changes only insignificantly (e.g. in response to low-speed base motions). A CMG does use at least as much energy as the change in the satellite body's kinetic energy, but still much less than would be used by an RWA. Comparisons of RWAs and CMGs have previously shown the power benefits of using CMGs over RWAs, both in attitude control [Lappas *et al.*, 2005; Van Riper and Liden, 1971] and specifically for robotic applications [Carpenter and Peck, 2008]; the former

references tested physical models and the latter reference compares simulation results. This paper is the first comparison of CMGs with joint motors for robotic applications. In this work, as well as in the simulations reported in [Carpenter and Peck, 2008], the startup and standby power of CMGs are not considered. Omitting startup and standby power does not invalidate previous comparisons with reaction wheels that must also maintain a nonzero nominal speed to avoid excessive zero crossings but does highlight a key advantage of joint-motor actuation, which draw near zero power in a quiescent state.

A. Single CMG

This section develops the equations of motion for a single CMG to obtain an expression for the gimbal torque. The gimbal torque is combined with gimbal velocity in later sections to determine power used by the CMGs. Similar equations have been developed elsewhere [Carpenter and Peck, 2008; Schaub and Junkins, 2003], but the following first-principles derivations clarify the assumptions made in this work and help establish notation. Principles of angular momentum determine the applied gimbal torque, the output torque onto the body, and the torque necessary to maintain rotor speed.

Consider a control moment gyro attached to a body, e.g. attached to a segment of a robot arm. The CMG's angular-momentum vector about its center of mass, \mathbf{H}_{cmg} , is the sum of the momentum of the gimbal and the rotor:

$$\begin{aligned}
 \mathbf{H}_{cmg} &= \mathbf{I}_g \cdot \boldsymbol{\omega}^{G/N} + \mathbf{I}_r \cdot \boldsymbol{\omega}^{R/N} \\
 &= \mathbf{I}_g \cdot (\boldsymbol{\omega}^{G/B} + \boldsymbol{\omega}^{B/N}) + \mathbf{I}_r \cdot (\boldsymbol{\omega}^{R/G} + \boldsymbol{\omega}^{G/B} + \boldsymbol{\omega}^{B/N}) \\
 &= \mathbf{I}_{cmg} \cdot (\boldsymbol{\omega}^{G/B} + \boldsymbol{\omega}^{B/N}) + \mathbf{h}_r
 \end{aligned} \tag{2}$$

where the total CMG inertia is $\mathbf{I}_{cmg} = \mathbf{I}_g + \mathbf{I}_r$, and the term $\mathbf{I}_r \cdot \boldsymbol{\omega}^{R/G} = \mathbf{h}_r$.

The torque produced by the CMG onto the spacecraft or robot link, $\boldsymbol{\tau}_{cmg}$, is found by taking the time derivative in the N frame.

$$\boldsymbol{\tau}_{cmg} = -\dot{\mathbf{H}}_{cmg}^N \quad (3)$$

where the time derivative of an arbitrary vector \mathbf{x} taken in frame Y is written

$$\dot{\mathbf{x}}^Y = \frac{d}{dt}(\mathbf{x})^Y \quad (4)$$

From Eq. (2),

$$\dot{\mathbf{H}}_{cmg}^N = \mathbf{I}_{cmg} \cdot \left(\ddot{\hat{\boldsymbol{\phi}}\mathbf{g}} + \boldsymbol{\omega}^{B/N} - \dot{\hat{\boldsymbol{\phi}}\mathbf{g}} \times \boldsymbol{\omega}^{B/N} \right) + (\dot{\hat{\boldsymbol{\phi}}\mathbf{g}} + \boldsymbol{\omega}^{B/N}) \times \left[\mathbf{I}_{cmg} \cdot (\dot{\hat{\boldsymbol{\phi}}\mathbf{g}} + \boldsymbol{\omega}^{B/N}) + \mathbf{h}_r \right] \quad (5)$$

where $\boldsymbol{\omega}^{G/B} = \dot{\hat{\boldsymbol{\phi}}\mathbf{g}}$. The overdot represents the time derivative of a scalar. In the case of a CMG inertia \mathbf{I}_{cmg} that is constant in any frame, as for a spherical body, the term $(\dot{\hat{\boldsymbol{\phi}}\mathbf{g}} + \boldsymbol{\omega}^{B/N}) \times \left[\mathbf{I}_{cmg} \cdot (\dot{\hat{\boldsymbol{\phi}}\mathbf{g}} + \boldsymbol{\omega}^{B/N}) \right]$ is eliminated from Eq. (5). A spherical CMG inertia closely approximates a physical system because \mathbf{I}_{cmg} consists of the rotor, the gimbal support structure, and both gimbal and rotor motors. A study of high-accuracy control algorithms or a geometrical analysis of the rotor and gimbal would require an exact \mathbf{I}_{cmg} , but a power comparison between a joint-motor-actuated robot and a CMG with a spherical \mathbf{I}_{cmg} still has value for designing more general CMGs. Furthermore, the six time-varying parameters required to describe the CMG's inertia dyadic are replaced with just one. Mathematically, the CMG inertia may be written as

$$\mathbf{I}_g + \mathbf{I}_r = \mathbf{I}_{cmg} = \mathbf{I}_{cmg} \mathbf{I} \quad (6)$$

This work also assumes that the CMG rotor and gimbal are rigid bodies. However, flexible effects of the rotor and gimbal along the $\hat{\mathbf{g}} \times \hat{\mathbf{h}}$ axis increase gimbal torque $\boldsymbol{\tau}_g$. The CMG inertia must therefore also include the output-axis stiffness k_{OA} [Liden, 1974]:

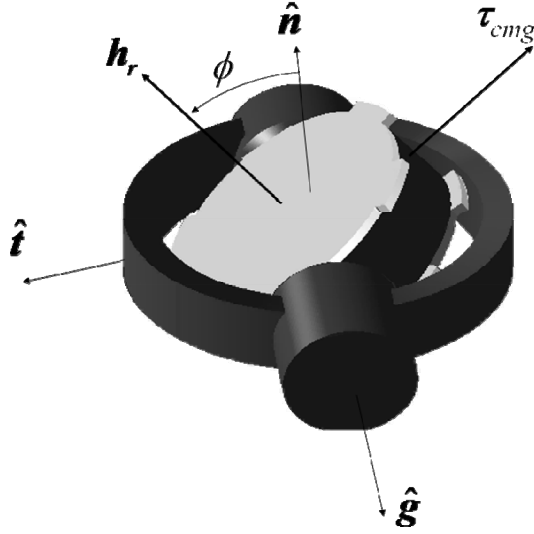


Figure 4. CMG vectors and scalars defined.

The preferred body-rotation axis \hat{t} , e.g. the joint axis for a robot arm, the gimbal axis \hat{g} , and the normal \hat{n} define the body-fixed coordinate system. When the gimbal angle ϕ is zero, the rotor angular momentum h_r is aligned with \hat{n} and the output torque τ_{cmg} is aligned with \hat{t} .

$$I_{cmg} = I_{cmg} \cdot \hat{g} + \left(h_r^2 / k_{OA} \right) \quad (7)$$

The torques acting on the CMG are the applied gimbal torque and the torque reacted onto the body. In the absence of friction, electromagnetic forces, and flexible effects, the time derivative of the CMG angular momentum equals the external torques. For a slow body rate $\omega^{B/N}$ the torque acting on the spacecraft is approximated by the gimbal rate crossed with the rotor momentum, resulting in the classic expression for gyroscopic torque (see Figure 4).

$$\tau_{cmg} = -\dot{\phi} \hat{g} \times h_r \quad (8)$$

Even for a stationary body ($\omega^{B/N} = 0$), Eq. (8) shows that the direction of τ_{cmg} is not constant because of its dependence on ϕ .

Adapting to changing CMG output torque is among the biggest challenges of CMG-based attitude-control system design because the array of CMGs can encounter singularities [Kurokawa, 2007; Margulies and Aubrun, 1978]. Singularities arise when the possible gimbal motions cannot produce the desired output torque from the array. For the robot under investigation here, the desired torque is always along the robot's joint axis. A scissored pair both constrains the torque output to act only along the joint axis and avoids the internal singularities associated with more general CMG arrays.

B. Scissored-Pair CMGs

In a scissored pair of CMGs, two CMGs with parallel gimbal axes maintain equal-magnitude and opposite-sign gimbal angles (Figure 5). Scissored pairs, also referred to as V-gyros or twin-gyros [Havill and Ratcliff, 1964] produce torque about a single axis by using antisymmetric (equal-magnitude, opposite direction) gimbal angles to cancel unwanted torque on the body. Cross coupling torques acting on the gimbal motors that result from body motion can be cancelled internally to reduce gimbal torque [Havill and Ratcliff, 1964; Brown and Peck, 2008; Liska, 1968]. Singularities occur in a scissored pair only if the commanded torque exceeds the gimbal-rate capability of the scissored pair in magnitude or if the momentum stored in the pair is at a maximum. Related saturation singularities occur in any actuator. Scissored pairs also have a simple zero-angular-momentum configuration, useful for rotor spin-up and ensuring that motion of other robot links does not induce unwanted gyroscopic torque even though the rotors spin continuously. While this paper does not explore the application of a single CMG for each link, there may be some benefit to be gained by using them in this way.

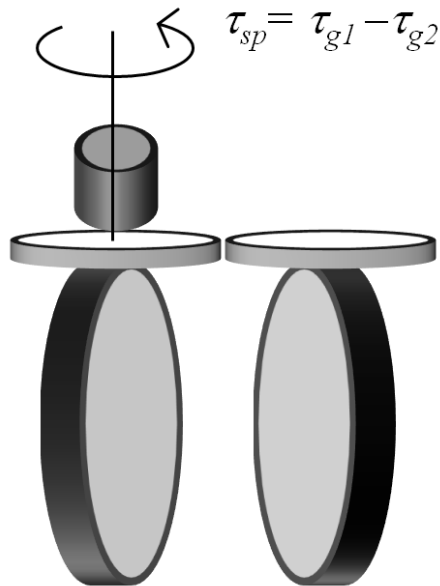


Figure 5. Geared scissored-pair CMGs.

A geared scissored pair uses a single gimbal motor with a mechanical coupling between CMGs, such as gears or a mechanical linkage, to enforce the gimbal-angle symmetry (Figure 5). An early double-gimbal CMG (DSCMG) scissored-pair concept with mechanical synchronization is described by [Liska, 1968]. In that design, each DSCMG is the central body of a universal joint with the shafts at right angles to gimbal the rotor. The shafts of each DSCMG are coupled with steel belts in lieu of gears. They reported 0.1 arcsecond pointing accuracy with their setup [Liska, 1968].

In contrast to the geared scissored pair, each CMG in a scissored pair of independently driven CMGs has its own gimbal motor. This chapter explores the benefits of using a gear to cancel workless constraint torques that would otherwise act on the independent CMGs. The gears also replace the two independent gimbal motors with a single motor, which may represent improved mass and volume efficiency in the electromechanical design. Friction and backlash in the gears are not modeled in this work, but represent a potential problem for the geared CMGs. Gears could reduce or

eliminate misalignment of the gimbal angles otherwise compensated with control system design as discussed in [Yang and Chang, 1996].

Independent scissored pairs do provide a second degree of freedom in the actuator. If the desired output torque is along more than a single axis, a pair of independent CMGs may suffice where two pairs of geared scissored pairs would otherwise be used. Independent scissored pairs are also more robust to single point failure since the loss of one CMG still leaves the other operational. A geared scissored pair has a single point of failure if the gimbal motor malfunctions.

Scissored pairs attempt to mitigate some of the difficulties associated with traditional CMGs that arise from the changing direction of the CMG output torque. Accommodating the changing output-torque direction is among the greatest challenges of CMG-based attitude-control system design because this effect can lead to internal singularities [Kurokawa, 2007]. When a CMG array is singular, it cannot produce the commanded torque. Singularities in scissored pairs occur only if the commanded torque exceeds the capability of the scissored pair in magnitude or if the momentum stored in the pair is at a maximum. Related saturation singularities occur in any actuator. Scissored pairs otherwise offer a singularity-free range of angular momentum, unlike other CMG array geometries [Elgersma et al., 2007]. Essentially, a scissored pair array provides a set of constant-direction, variable-magnitude momentum vectors, whereas typical CMG arrays provide a set of constant-magnitude, variable-direction momentum vectors. Scissored pairs also have a unique zero-angular-momentum configuration, useful for rotor spin-up and ensuring that motion of other links does not induce unwanted gyroscopic torque even though the rotors spin continuously. However, their singularity-free performance artificially limits the momentum envelope of a scissored-pair array to a single line instead of a disc by constraining the available output torque of the pair. This chapter does not investigate

the relative merits of such an array with other possible CMG arrays. Rather, the focus is on the internal torque cancellation and the resulting power savings for a geared scissored pair as compared to an independent scissored pair.

1. Scissored Pair Analysis

Although the magnitude of the rotor momentum is constant and identical for each CMG in the pair, the direction of the rotor momentum is different. Therefore $\mathbf{h}_{r1} \neq \mathbf{h}_{r2}$, where a subscript 1 or 2 is used to distinguish between the two CMGs. The torque applied by the gimbal motor on the first of the two CMGs acts only along the gimbal axis and is the dot product of $\hat{\mathbf{g}}$ and Eq. (5). The rotor momentum magnitude is identical for each CMG, but the direction is not. The gimbal torque for the i th CMG, $i \in [1, 2]$, is given by:

$$\tau_{g,i} = (-1)^{i-1} \cdot I_{cmg} \ddot{\phi} + I_{cmg} \boldsymbol{\omega}^{B/N} \cdot \hat{\mathbf{g}} + (\boldsymbol{\omega}^{B/N} \times \mathbf{h}_{r,i}) \cdot \hat{\mathbf{g}} \quad (9)$$

Figure 6 shows the gimbal angle ϕ , the body rate relative to the inertial N frame $\boldsymbol{\omega}^{B/N}$, and the rotor momentum $\mathbf{h}_{r,i}$, which is constant in the gimbal frame. The gimbal axis $\hat{\mathbf{g}}$ comes out of the page. In Figure 7, a control volume for each gimbal isolates the individual gimbal torques. Another control volume including only the single motor for the scissored pair and each of the gimbal torques shows that a gear results in a net applied torque on the scissored pair τ_{sp} equal to the difference between the two gimbal torques.

$$\tau_{sp} = \tau_{g1} - \tau_{g2} \quad (10)$$

$$\tau_{sp} = 2I_{cmg} \ddot{\phi} + [\boldsymbol{\omega}^{B/N} \times (\mathbf{h}_{r1} - \mathbf{h}_{r2})] \cdot \hat{\mathbf{g}} \quad (11)$$

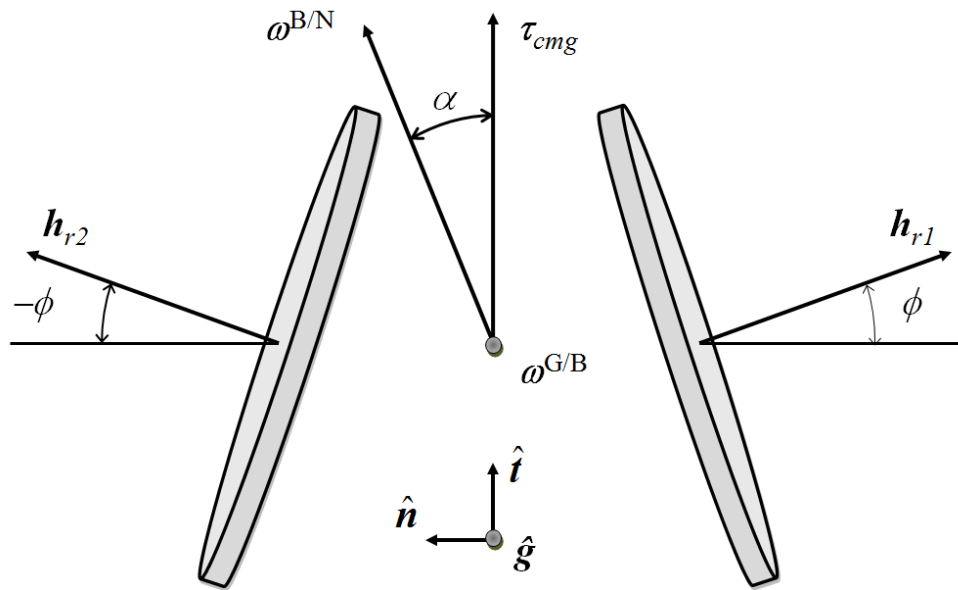


Figure 6. Scissored-pair kinematics.

The equal-magnitude, opposite sign gimbal angles cause the net change in the angular to always be aligned with the output torque axis \hat{t} , coincident with the joint axis. The unit vector triad defines the body fixed frame, and the \hat{g} axis is the same for the body and gimbal frames.

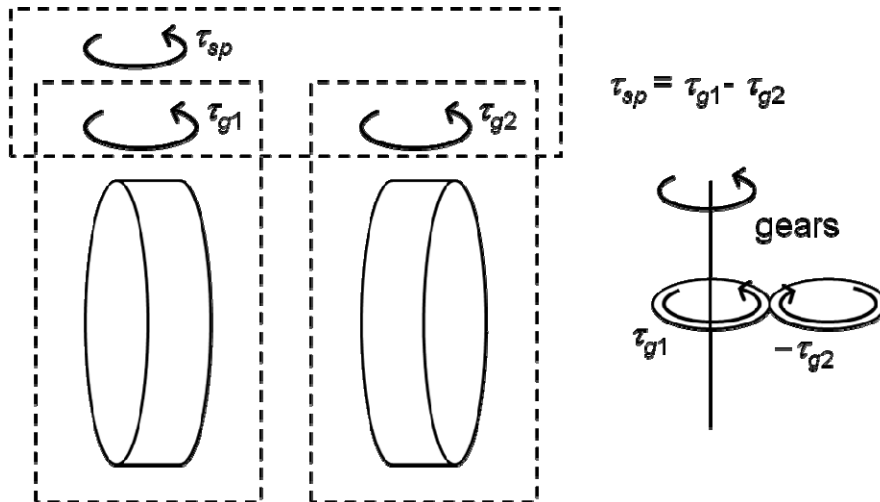


Figure 7. Applied torque on a scissored pair.

The gimbal torque on a scissored pair is equal to the difference of the individual gimbal torques. The gear changes the sign of the second gimbal torque, demonstrated by considering each CMG separately, and then balancing the torques for a massless gear train.

The unit vector $\hat{\mathbf{i}}$ as defined in Figure 6 simplifies the scalar triple product to a dot product of the body rate and the scissored-pair angular momentum.

$$\tau_{sp} = 2I_{cmg}\ddot{\phi} - \boldsymbol{\omega}^{B/N} \cdot 2h_r \cos\phi \hat{\mathbf{t}} \quad (12)$$

The first term in this expression corresponds to accelerating the gimbal. The second term accounts for the body rate and is referred to as the base-rate effect. The base-rate effect plays a significant role in energy costs of CMGs.

From the work-energy principle [Bedford and Fowler, 2005; Oh et al., 1992], the power used by the CMGs for a maneuver is the product of gimbal torque and gimbal rate. For the geared scissored pair motor, the power is

$$P_{sp} = |\tau_{sp}\dot{\phi}| \quad (13)$$

For the independent scissored pair, the power is the sum of the powers of the individual gimbal motors:

$$P_{ind} = |\tau_{g1}\dot{\phi}| + |\tau_{g2}\dot{\phi}| \quad (14)$$

where $\dot{\phi}$ for each CMG has identical magnitude. This expression neglects electromagnetic inefficiencies under the likely assumption that the gimbal torque *per se* drives the power design in an agile application. Friction losses may make CMGs an inefficient choice for a generally quiescent system. The absolute value in Eq. (13) ensures that power is independent of the sign of gimbal torque and gimbal rate. This study does not distinguish between positive or negative power since both require work from the gimbal motor. The sign would matter in a case where the spacecraft power system efficiently recovered this energy expenditure in a regenerative fashion, e.g. using the gimbal motor as a generator. In practice, such an approach may not be very efficient or may be too costly and complex. Such an architecture is not in place for

purposes of this study. Therefore these comparisons consider only the absolute value of power.

The rotor momentum h_r is usually large relative to the CMG inertia I_{cmg} and accelerations $\ddot{\phi}$, with the latter limited by the gimbal motor. Adding the assumption that gimbal acceleration does not contribute significantly to the gimbal torque greatly simplifies comparisons between the geared and independent scissored pairs.

$$I_{cmg}\ddot{\phi} \ll \boldsymbol{\omega}^{B/N} \cdot h_r \cos \hat{\phi} \hat{\mathbf{t}} \quad (15)$$

This assumption implies that the CMG inertia is small, whereas the rotor momentum is large. With this assumption, a simplified expression for net gimbal torque on a scissored pair is

$$\tau_{sp} \approx -\boldsymbol{\omega}^{B/N} \cdot 2h_r \cos \hat{\phi} \hat{\mathbf{t}} \quad (16)$$

An approximate power for the geared or the independent scissored pair is

$$P_{sp} \approx \left| \dot{\phi} \cdot \left[\boldsymbol{\omega}^{B/N} \times (\mathbf{h}_{r1} - \mathbf{h}_{r2}) \right] \cdot \hat{\mathbf{g}} \right| \quad (17)$$

$$P_{ind} \approx \left| \dot{\phi} \cdot (\boldsymbol{\omega}^{B/N} \times \mathbf{h}_{r1}) \cdot \hat{\mathbf{g}} \right| + \left| \dot{\phi} \cdot (\boldsymbol{\omega}^{B/N} \times \mathbf{h}_{r2}) \cdot \hat{\mathbf{g}} \right| \quad (18)$$

The component of $\boldsymbol{\omega}^{B/N}$ along the gimbal axis does not affect this result and is assumed to be zero without loss of generality. The projection of the body rate onto the plane normal to $\hat{\mathbf{g}}$ is represented as a magnitude $\|\boldsymbol{\omega}^{B/N}\|$ and an angle α at which the rate is oriented relative to the output axis of the scissored pair, as shown in Figure 6. The magnitude of the body rate, rotor momentum, and gimbal rate can be factored out of Eqs. (17) and (18) to define a nondimensional power P_x^* :

$$P_x^* = \frac{P_x}{\left(\|\boldsymbol{\omega}^{B/N}\| h_r \right)} \quad (19)$$

$$P_{sp}^* \approx |2 \cos \alpha \cos \phi| \quad (20)$$

$$P_{ind}^* \approx |\cos(\alpha - \phi)| + |\cos(\alpha + \phi)| \quad (21)$$

If there were no penalty for negative power, as in a lossless system that perfectly stores and returns negative power, there would be no distinction between geared and independent scissored pairs. The nondimensional power of independent and geared scissored pairs is shown for one quadrant of the gimbal-angle, body-rate-angle space in Figure 8a&b. A cyclical symmetry of P_x^* about both ϕ and α equal to $n \cdot \pi/2$, $n = \text{integer}$, is apparent from Eqs. (20) and (21), i.e. P_x^* repeats every $n \cdot \pi$ for both the gimbal angle and the body-rate angle. Normalizing by $\|\boldsymbol{\omega}^{B/N}\| \cdot h_r$ means that the power shown in Figure 8 is relevant if considered over many maneuvers in which the body-rate direction and gimbal angles are uniformly distributed. Many factors in the lifecycle of a scissored pair in space may affect the validity of comparing power equally over all gimbal angles ϕ and body-rate angles α , such as limits on the gimbal angles, biases in the pointing requirements of the robot or satellite, or control laws that favor certain gimbal angles and rates. For example, CMGs with limited gimbal angles truncate the graph at $\phi = \phi_{max}$.

When $\alpha = \phi = 0$, the origin of Figure 8a&b, the power is at a max, as expected, because the scissored pair is directly responsible for the work done on the body. When ϕ and α each approach $\pm \pi/2$, the scissored pair saturates (i.e., $\phi = \pi/2$ and the CMGs no longer provide angular momentum to the spacecraft) and the body rate is perpendicular to the output axis. At these extremes, the opposing torques add for the independent scissored pair but are canceled internally for the geared scissored pair. For $\alpha + \phi < \pi/2$ in the quadrant shown, the two require the same power. The geared scissored pair offers a clear advantage over the independent scissored pair for $\alpha + \phi > \pi/2$.

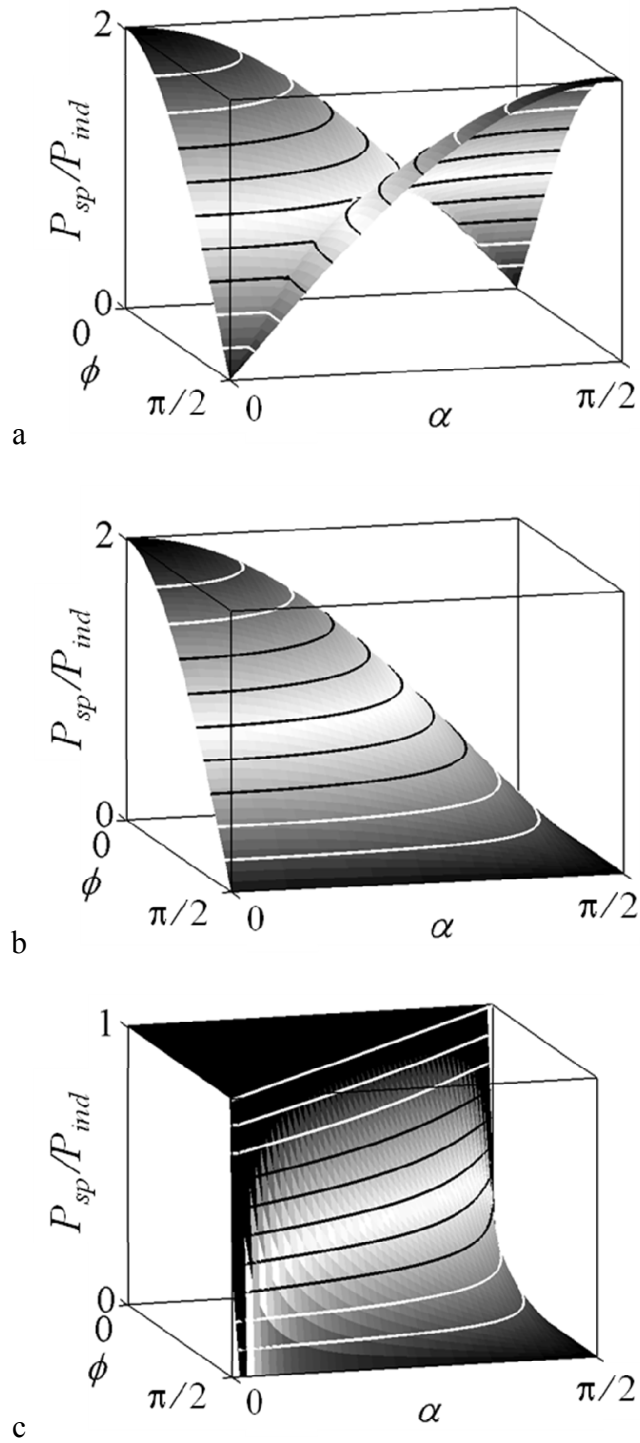


Figure 8. Nondimensional power of scissored pairs.

a) Independent scissored pairs requires full power when actively producing torque on the spacecraft (left peak) and when canceling gyroscopic torques (right peak). b) Geared scissored pair cancels the gyroscopic torques internally. c) Ratio of b to a.

The ratio of power for the geared scissored pair to power for the independent scissored pair as a function of ϕ and α is found from Eqs. (20) and (21). The body-rate magnitude, rotor momentum, and gimbal rate divide out.

$$\frac{P_{sp}}{P_{ind}} \approx \frac{|2 \cos \alpha \cos \phi|}{|\cos(\alpha - \phi)| + |\cos(\alpha + \phi)|} \quad (22)$$

The simplification from Eq. (15) removes $I_{cmg} \ddot{\phi}$ from both numerator and denominator in this equation, precluding a power ratio of zero.

This ratio is shown in Figure 8c as a function of base-rate angle α and gimbal angle ϕ . The volume of the region where the ratio is less than one represents the power savings. The integral of power is energy; therefore the volume enclosed by the surfaces in Figure 8a&b represents simplistically the total power over many maneuvers with uniformly distributed body and gimbal angles and rates. The ratio of the total enclosed volumes, found by integrating Eqs. (20) and (21), is $2/\pi$. These results do not show the contribution of $I_{cmg} \ddot{\phi}$, which adds an offset to Figure 8, dependent on the particular CMG design.

This comparison of geared and independent scissored-pair CMGs can be used to optimize the design of a CMG array and maneuver planning for power usage, and therefore agility, of a spacecraft controlled by scissored pairs. Other design considerations, e.g., total mass, motor size, fault tolerance, and complexity, are also likely impacted by this strategy but are not discussed here.

The maximum torque τ_{sp} and power P_{sp} of the motor on the geared scissored pair would seem to be twice that of the independent scissored pair since one motor actuates two CMGs instead of two motors providing the same level of actuation. However, if the body rate ω^{BN} is zero when all gimbal angles in an array are zero, the geared

scissored pair does not have maximum power at the origin while the independent scissored pair still has maximum power at $(\phi, \alpha) = (\pi/2, \pi/2)$.

For a spacecraft with three rotational degrees of freedom, an array of three orthogonal scissored pairs provides a cube-shaped singularity-free region with sides of length $4h_r$ (see Figure 9). This array architecture illustrates the possible advantages afforded by a geared scissored pair. The maximum angular momentum is $2\sqrt{3}h_r$ at the cube's corners. The gimbal angles for a given spacecraft momentum are easily found by projecting the spacecraft momentum vector $\mathbf{I}_b \cdot \boldsymbol{\omega}^{\text{B/N}}$ onto the output axis of each scissored pair and solving for the necessary gimbal angle to conserve angular momentum.

$$\left(\mathbf{I}_b \cdot \boldsymbol{\omega}^{\text{B/N}}\right) \cdot \hat{\mathbf{t}} = -2h_r \sin \phi \quad (23)$$

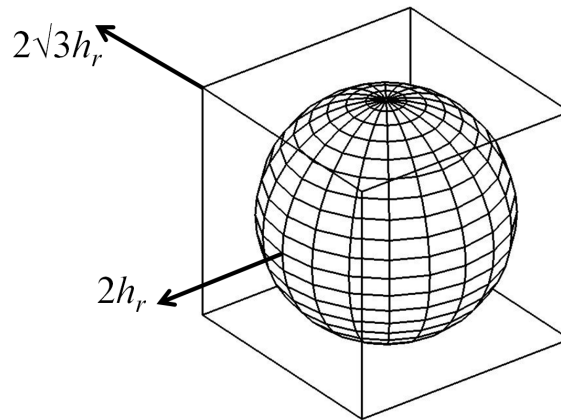


Figure 9. Scissored-pair array momentum cube.

The momentum available from a set of three orthogonal scissored pairs is a cube with sides of length $4h_r$. A single scissored pair provides $2h_r$ angular momentum for the spacecraft normal to the face of the cube. The maximum angular momentum available to the spacecraft from all three orthogonal scissored pairs is $2\sqrt{3}h_r$ at the cube's corners. The region inside the cube but outside the sphere represents the operational region that a geared scissored pair outperforms an independent scissored pair.

The body-rate angle α is determined from

$$\alpha = \cos^{-1} \left(\frac{\boldsymbol{\omega}^{B/N}}{\|\boldsymbol{\omega}^{B/N}\|} \cdot \hat{\boldsymbol{t}} \right) \quad (24)$$

For a spacecraft with spherical inertia, $\|\boldsymbol{\omega}^{B/N}\|$ is proportional to the spacecraft momentum. In this case, the geared and independent scissored pairs are equivalent when the array momentum lies within a momentum sphere of radius $2h_r$. The geared scissored pairs outperform their counterparts near the corners of the momentum envelope, a region representing up to 48% of the total momentum volume. This region is important for performing time-optimal maneuvers with actuator saturation [Wie et al., 2002]. Abrupt changes in attitude before the spacecraft comes to rest would further increase α and ϕ (Figure 6) in favor of the geared scissored pairs.

2. Scissored Pair Simulations

The agile spacecraft described in [Lappas et al., 2002] for a simple rotation about an axis. Three orthogonal scissored pairs provide actuation. The spacecraft angle, rate, and acceleration, $\theta, \dot{\theta}, \ddot{\theta}$, subject to finite jerk for a 30 degree maneuver are prescribed as shown in Figure 10. The maximum $\|\boldsymbol{\omega}^{B/N}\|$ is 6 degrees per second [18]. The desired $\boldsymbol{\omega}^{B/N}$ determines h_r from conservation of angular momentum for a rotation about the output axis of a single scissored pair.

$$|2h_r| = |\boldsymbol{I}_b \cdot \boldsymbol{\omega}^{B/N}| \quad (25)$$

The resulting CMG momentum h_r is 0.1314 kg·m²/s when a single scissored pair provides the actuation and the spacecraft inertia is $2.5 \cdot \boldsymbol{I}$ kg·m². When performing a maneuver that utilizes the corners of the momentum cube, all three scissored pairs contribute to the momentum available to the spacecraft. The greater momentum increases the maximum body rate by a factor of $\sqrt{3}$ for those maneuvers.

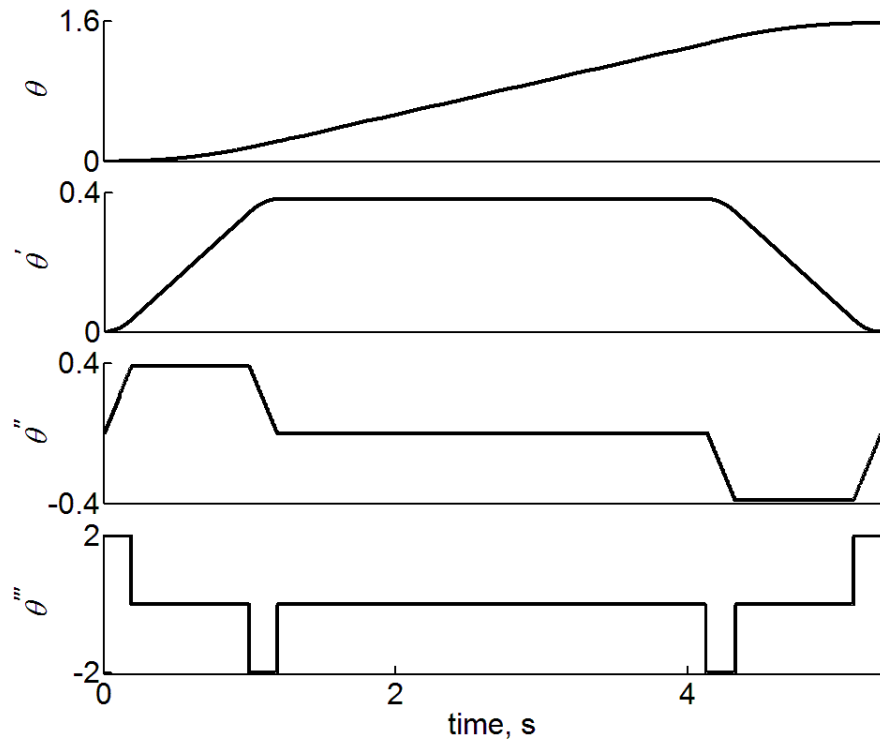


Figure 10. Commanded spacecraft angle, rate, and acceleration.

The spacecraft rotates smoothly about the $[1\ 0\ 0]$ (face normal) or the $[1\ 1\ 1]/\sqrt{3}$ (corner) axis to represent the range of loads on the scissored pairs when operating on the momentum envelope. The maximum gimbal angle is 85 degrees. The maximum torque and power of any single gimbal motor in the array, the maximum power of the entire array, and the total energy used for the maneuver are calculated for both geared and independent scissored pairs. The results are summarized in Table 1. The independent scissored pairs have the greatest maximum torque because they must work against the base-rate effect while doing little work on the spacecraft; i.e. the scissored pair constraint enforces a costly null motion. The geared scissored pair has a higher maximum power by only 20% over the independent scissored pair because of internal torque cancellations, indicating that one motor with gearing reduces mass over two independent gimbal motors in a scissored pair. The spacecraft power subsystem

Table 1. Maximum torque and power for geared and independent scissored pairs.

Location on momentum cube	Face center		Corner	
Max body rate θ_{max} , rad/s	0.1049		0.1816	
Gimbal configuration	Geared	Independent	Geared	Independent
Max motor torque τ_{sp} or $\tau_{g,i}$, mN·m	13.9	7.0	14.0	16.8
Max motor power, mW	6.0	3.0	4.5	5.0
Max total power P_{sp} or P_{ind} , mW	6.0	6.0	13.6	21.4
Total energy E_{sp} or E_{ind} , mJ	27.5	27.5	82.5	129

can also be smaller for the geared scissored pair since the maximum power is 36% less than for the independent scissored pair. As expected from the analysis, the geared and independent scissored pair arrays use the same amount of energy when operating on a face of the momentum cube, but the geared scissored pairs use less energy at the corners. The body rate effect causes the maximum gimbal power of the geared scissored pair to be less at the faster corner maneuver than the face maneuver even though maximum torque is the same. This is because the extra speed available to the spacecraft at the corner of the momentum cube does not correspond to an increase in acceleration and jerk of the base body.

The simulations consider nearly the full range of gimbal angles. If a smaller value of ϕ_{max} were used, the power costs associated with independent scissored pairs would be reduced. A gear may still be desirable for mechanically coupling the control inputs to ensure proper phasing of the two CMGs.

3. Scissored Pair Conclusions

A mechanical constraint between the CMGs of a scissored pair provides internal torque cancellation to limit the power used by the CMGs. The advantage in power used over independent CMGs occurs near the limit of the scissored pair's momentum capacity. A geared scissored pair may reduce the overall mass of the scissored pair by replacing two motors, and the extra housing, harness, and connector mass, with one motor and the connecting gears. Non-linearities in the gears or mechanism connecting the CMGs may affect these results; thus actual power savings would depend on the hardware implementation. The independent scissored pair performs poorly relative to the geared scissored pair in simulations because they perform costly null motions that are affected by the base rate. The base rate effects are cancelled internally via the mechanical coupling. Although only two types of scissored-pair CMG arrays are considered in this chapter, the difference in power between them suggest that the operation of general CMG arrays with null motion [*Bedrossian et al.*, 1990; *Vadali et al.*, 1990] could strongly affect the power used.

CHAPTER III. ANALYSIS AND CONTROL OF ROTOR SPEED

An analysis of CMG power would be incomplete without also considering the power used by the rotor spin motor. This chapter examines two conflicting assumptions that are each useful in determining the dynamics and power use of CMGs. First, the case of a constant speed rotor is considered, with an emphasis on the power required to maintain rotor speed in spite of the motion of the spacecraft. A constant rotor speed is commonly assumed to reduce the complexity of the dynamic equations and because typical rotor speed sensors and motors reference the rotor speed relative to the gimbal frame. In this work, rotor speed is defined relative to the gimbal frame and the magnitude of the rotor's angular velocity is considered separately.

The second assumption considered is the case where the spin motor's power is constant in spite of the motion of the spacecraft base. In the limit of an ideal rotor, the power goes to zero and only gimbal power is needed to characterize the total CMG power. Power-optimal CMG control algorithms need to use a cost function that distinguishes which of these two cases apply to a particular spacecraft.

Figure 11 illustrates how the constant-rotor-speed assumption departs from the ideal CMG. In Figure 11a, the spacecraft is at rest and the angular momentum of the two CMGs is perfectly canceled. In Figure 11b, the two CMGs combine their angular momentum, causing the spacecraft to rotate in the opposite direction to conserve angular momentum. If no torque has been applied to the rotor, then the angular velocity of the rotor about the spin axis will be constant *relative to the N frame*. Figure 11c shows that the rotor speed, as measured relative to the spacecraft, has changed. A spin motor required to maintain constant rotor speed would have slowed down the rotors and lost that energy.

This chapter first examines the energy cost of maintaining a constant rotor speed during base motion through what amounts to a kinematic constraint. Then the zero-rotor-torque case posits a spin motor that provides enough torque to overcome friction and other steady state losses but allows the rotor speed to vary. No additional energy is required in this case. Rather, variable rotor speed affects both the spacecraft angle and the gimbal angle. These results inform the validity of the assumption used in this dissertation to simplify the analysis while ensuring its accuracy with regards to the dynamics and power of the CMG and spacecraft.

Although a review of the literature does not reveal an analysis of the constant rotor speed assumption, rotor speed has been subject to a variety of studies. Early CMG rotors for space applications used induction motors with a large time constant and were assumed to have a nearly constant speed because the response time of such motors is slow relative to the other dynamics [Liska, 1968]. Control of the CMG rotor speed is important for integrated power and attitude control systems (IPACS). IPACS use a combination of drive motor and generator circuitry to change the rotor speed for the purpose of regulating the satellite power while passing through the shadow of the earth [Notti *et al.*, 1975]. A recent study on an IPACS architecture for the International Space Station (ISS) uses fixed-axis, kinetic energy storage rotors in concert with the existing CMGs [Roithmayr *et al.*, 2004]. Neither of these studies examines the power required by the attitude controller in the context of constant speed rotors. The rotor speed of CMGs is also varied in variable-speed CMGs (VSCMGs). VSCMGs attempt to remove the singularities in a CMG array [Schaub *et al.*, 1998] by treating the CMG array as a combination of reaction wheels and CMGs. Although the treatment of VSCMGs does include expressions for the torque required of the rotor motor [Schaub *et al.*, 1998], the power required to operate a VSCMG is not addressed.

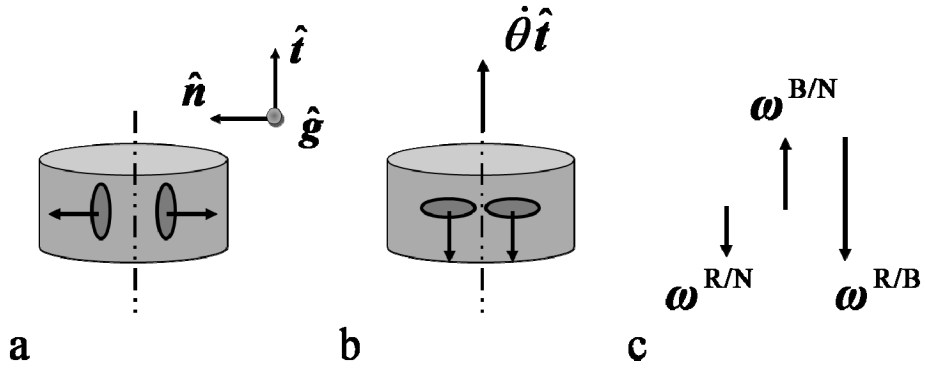


Figure 11. Rotor speed constant in N frame.

a. The single-link robot at rest. b. The CMGs have rotated 90 deg about the gimbal axis. Net angular momentum is still zero since the body's angular velocity is opposite in sign to the rotors. c. Rotor speed, $|\omega^{R/B}|$, has increased, whereas $|\omega^{R/N}|$ remains constant in the N frame.

A. Energy cost of constant-speed rotor control

In this chapter, the system under study is spacecraft with an arbitrary array of n CMGs attached. The gimbal rate of the i th CMG is $\dot{\phi}_i$ and the rotor's spin speed is Ω_i ; both are scalar values measured relative to the body. With these definitions, the rotational energy of the composite body E_c is [Carpenter and Peck, 2008]:

$$\begin{aligned}
 E_c = & \frac{1}{2} \omega^{B/N} \cdot \mathbf{I}_{sc} \cdot \omega^{B/N} + \frac{1}{2} \sum_{i=1}^n (\omega^{B/N} + \dot{\phi}_i \hat{\mathbf{g}}_i) \cdot \mathbf{I}_{g,i} \cdot (\omega^{B/N} + \dot{\phi}_i \hat{\mathbf{g}}_i) \\
 & + \frac{1}{2} \sum_{i=1}^n (\omega^{B/N} + \dot{\phi}_i \hat{\mathbf{g}}_i + \Omega_i \hat{\mathbf{h}}_i) \cdot \mathbf{I}_{r,i} \cdot (\omega^{B/N} + \dot{\phi}_i \hat{\mathbf{g}}_i + \Omega_i \hat{\mathbf{h}}_i)
 \end{aligned} \tag{26}$$

where \mathbf{I}_{sc} is the spacecraft inertia dyadic without the CMGs, and the other terms are defined as in the previous chapter.

The effect of changing the rotor speed of a single CMG on the total energy is captured by the sensitivity of E_c to Ω , i.e. the partial derivative of E_c with respect to Ω where the index has been dropped for notational clarity.

$$\frac{\partial E_c}{\partial \Omega} = \hat{\mathbf{h}} \cdot \mathbf{I}_r \cdot (\boldsymbol{\omega}^{B/N} + \Omega \hat{\mathbf{h}}) \quad (27)$$

The energy cost of changing Ω is very large due to an amplifying effect of Ω , indicating that controlling the rotor speed is energetically costly. The power required to control Ω is

$$P_r = \tau_r \cdot \Omega \quad (28)$$

The spin-motor torque, τ_r , is determined from the derivative of the rotor's angular momentum \mathbf{H}_r .

$$\mathbf{H}_r = \mathbf{I}_r \cdot (\boldsymbol{\omega}^{B/N} + \dot{\phi} \hat{\mathbf{g}} + \Omega \hat{\mathbf{h}}) \quad (29)$$

$$\dot{\mathbf{H}}_r^N = \mathbf{I}_r \cdot \left(\boldsymbol{\omega}^{B/N} - \dot{\phi} \hat{\mathbf{g}} \times \boldsymbol{\omega}^{B/N} + \ddot{\phi} \hat{\mathbf{g}} + \dot{\Omega} \hat{\mathbf{h}} \right) + (\boldsymbol{\omega}^{B/N} + \dot{\phi} \hat{\mathbf{g}}) \times \left[\mathbf{I}_r \cdot (\boldsymbol{\omega}^{B/N} + \dot{\phi} \hat{\mathbf{g}} + \Omega \hat{\mathbf{h}}) \right] \quad (30)$$

The component of $\dot{\mathbf{H}}_r^N$ along the rotor axis $\hat{\mathbf{h}}$ is

$$\tau_r = \left\{ \mathbf{I}_r \cdot \left(\boldsymbol{\omega}^{B/N} - \dot{\phi} \hat{\mathbf{g}} \times \boldsymbol{\omega}^{B/N} + \dot{\Omega} \hat{\mathbf{h}} \right) + (\boldsymbol{\omega}^{B/N} + \dot{\phi} \hat{\mathbf{g}}) \times \left[\mathbf{I}_r \cdot (\boldsymbol{\omega}^{B/N} + \dot{\phi} \hat{\mathbf{g}}) \right] \right\} \cdot \hat{\mathbf{h}} \quad (31)$$

An axisymmetric rotor eliminates the latter scalar triple product, simplifying the rotor torque to

$$\tau_r = I_r \left(\boldsymbol{\omega}^{B/N} - \dot{\phi} \hat{\mathbf{g}} \times \boldsymbol{\omega}^{B/N} \right) \cdot \hat{\mathbf{h}} + I_r \dot{\Omega} \quad (32)$$

where $I_r = \hat{\mathbf{h}} \cdot \mathbf{I}_r \cdot \hat{\mathbf{h}}$.

From Eq. (28), the power required to maintain a constant Ω in the presence of spacecraft motion is

$$P_r = \Omega \cdot I_r \left(\boldsymbol{\omega}^{B/N} - \dot{\phi} \hat{\mathbf{g}} \times \boldsymbol{\omega}^{B/N} \right) \cdot \hat{\mathbf{h}} \quad (33)$$

If the contribution of $\boldsymbol{\omega}^{\text{B/N}}$ is small, then P_r for a scissored pair is approximately equal to the gimbal power (*cf.* Eq. (17) and (18)).

$$P_r \approx \left| \left(\dot{\phi} \hat{\mathbf{g}} \times \boldsymbol{\omega}^{\text{B/N}} \right) \cdot \mathbf{h}_r \right| \quad (34)$$

Therefore, when strictly enforcing constant Ω , the spin motor uses as much energy as the gimbal motor. The high energy costs of reaction wheels as compared to CMGs is due to the costs of controlling high-speed rotors [Peck, 2005; Van Riper and Liden, 1971]. Forcing a constant Ω for energy calculations may unnecessarily penalize the CMGs' performance.

B. Zero rotor torque

When the rotor speed Ω is not controlled, no extra energy is required by the rotor beyond that determined by bearing friction, electromagnetic losses, and other inefficiencies in the rotor. However, Ω varies in response to gimbal and body rotations. This section examines errors in gimbal and CMG output torque, τ_g and τ_{cmg} , due to assuming constant Ω without enforcing constant rotor speed. An expression for the change in Ω due to spacecraft motion is also derived.

1. Gimbal torque

The gimbal torque derived in Eq. (9) assumes constant Ω . Relaxing this assumption adds $I_r \dot{\Omega} \hat{\mathbf{h}}$ to Eq. (5), but does not change Eq. (9). The sensitivity of τ_g to Ω represents the potential errors in τ_g due to either dynamically changing rotor speed or imperfect measurements. The partial derivative of Eq. (9) with respect to Ω is

$$\frac{\partial \tau_g}{\partial \Omega} = \left(\boldsymbol{\omega}^{\text{B/N}} \times I_r \hat{\mathbf{h}} \right) \cdot \hat{\mathbf{g}} \quad (35)$$

For a given rotor momentum, as $\Omega \rightarrow \infty$, $I_r \rightarrow 0$, and τ_g will be unaffected by changes in Ω . An infinite-speed rotor creates a theoretical tool that replaces the CMG with an embedded angular momentum vector whose direction changes by applying a torque τ_g .

2. CMG output torque

Changes in the rotor speed Ω influence the torque applied to the spacecraft, τ_{cmg} , and the attitude control of the spacecraft. The sensitivity of τ_{cmg} to the rotor speed is:

$$\frac{\partial \tau_{cmg}}{\partial \Omega} = I_r \hat{\mathbf{h}} + (\boldsymbol{\omega}^{B/N} + \dot{\phi} \hat{\mathbf{g}}) \times I_r \hat{\mathbf{h}} \quad (36)$$

As with the gimbal torque τ_g , as Ω approaches infinity, Eq. (36) goes to zero. In contrast, because energy depends quadratically on rotor speed, its sensitivity to rotor speed is much greater. Therefore, rotor speed affects energy more directly than torque—both the input gimbal torque and the output torque on the body.

3. Change in rotor speed

If $\Omega = \Omega_0$ and $t=t_0$ when the spacecraft is at rest, then Eq. (29) taken in the $\hat{\mathbf{h}}$ direction at time $t=t_0$ and any arbitrary time t yields the following relationship between the spacecraft rotation rate $\dot{\theta}$ and rotor speed.

$$I_r \dot{\theta} \sin \phi + I_r \Omega = I_r \Omega_0 \quad (37)$$

Assuming that Ω is constant in the analysis without enforcing that constraint causes an error in rotor speed. From Eq. (37), this error is

$$\Omega - \Omega_0 = \Omega_{err} = -\dot{\theta} \sin \phi \quad (38)$$

The constant rotor speed assumption is conservative because Ω_{err} is always positive since the sign of $\dot{\theta}$ and $\sin \phi_{max}$ will always be opposite each other, as illustrated by Figure 11. This means that the actual available momentum from the CMGs, $h_r = I_r \Omega$, is greater than h_r as estimated from Ω_0 . Also, Ω_{err} depends only on the spacecraft rate

and gimbal angle, not the rotor speed itself. Thus the relative error of Ω (i.e., Ω_{err}/Ω) decreases as Ω increases.

4. Error in spacecraft rate

The angular-momentum balance of a spacecraft constrained to rotate about a single axis of rotation under CMG actuation provides another constraint between rotor speed and spacecraft rate. In the case where the spacecraft starts at rest, the net angular momentum \mathbf{H}_c must be zero along the axis of rotation.

$$I_c \dot{\theta} + I_r \Omega \sin \phi = 0 \quad (39)$$

where I_c is the inertia of the spacecraft and CMGs about the axis of rotation. Again assuming that an estimated spacecraft rate $\dot{\theta}_{est}$ is determined from Eq. (39) for $\Omega = \Omega_0$, then the error in the estimated base rate, $\dot{\theta}_{err} = \dot{\theta} - \dot{\theta}_{est}$, is found by combining Eqs. (38) and (39).

$$I_c \dot{\theta}_{err} + I_r \Omega_{err} \sin \phi = 0 \quad (40)$$

Substituting for Ω_{err} and solving for $\dot{\theta}_{err}$ yields

$$\dot{\theta}_{err} = I_r \dot{\theta} \sin^2 \phi / I_c \quad (41)$$

The sign of $\dot{\theta}_{err}$ tracks the sign of $\dot{\theta}$, indicating that the spacecraft rotates faster than estimated by less than the ratio of rotor to spacecraft inertia I_r/I_c without enforcing constant rotor speed.

5. Rotor speed conclusions

Allowing Ω to vary maintains the rotor's angular velocity relative to an inertial reference frame and reduces the energy costs of unnecessarily controlling rotor speed to maintain constant Ω . The analysis of the spacecraft rate in Eq. (41) shows that a spacecraft designed to constant Ω conservatively predicts the maximum spacecraft rate attainable when rotor speed is not rigorously controlled.

Two observations about the rotor control arise from the analyses of rotor speed. First, accelerating and decelerating the rotor is energetically costly as shown by P_r in Eq. (34) and should be minimized. Therefore, slow, low-effort control should be selected to control the rotor speed. Specifically, if the controller bandwidth is much greater than the body-motion bandwidth, then the rotor control fully compensates for the body motion and $\Omega = \Omega_0$, with an accompanying energy cost. Otherwise, if the controller bandwidth is much less than the body-motion bandwidth, then the rotor control ignores the effect of spacecraft motion on Ω and the CMG uses much less energy.

It is also noted that changes in the steady state drag are expected over much longer time scales than the spacecraft motion. As such, any disturbances would be rejected by the rotor-speed control, thereby ensuring that the $\Omega \rightarrow \Omega_0$ when the spacecraft is at rest.

Second, for a low-effort controller, Eq. (38) indicates that the error in rotor speed is positively biased. An integral controller would artificially reduce rotor speed over several spacecraft maneuvers as the errors in Eq. (38) accumulate. An aggressive rotor-speed control is also inadvisable because interaction between rotor speed control and the spacecraft may act like an uncompensated reaction wheel creating unwanted disturbances. A larger spin motor than is practical may also be required to generate the necessary torques at high speeds.

Finally, as long as I_r/I_c is small, the rotor speed is assumed constant to simplify modeling and control of the CMG dynamics, and spin motor power is assumed to be zero for an ideal motor.

C. Control Laws for Single-Link Robot

In this section, the CMG dynamics with variable rotor speed are derived. Simple control laws for spacecraft rotation about a single degree of freedom are also given with increasing detail.

The equations of motion for a single spacecraft with an arbitrary array of identical CMGs are developed using [Schaub and Junkins, 2003] and [Roithmayr et al., 2004] as guides. Suppose that there are C single-gimbal CMGs on the spacecraft. The dynamics of the i th rotor is determined from the rotor dynamics in Eq. (32).

$$\tau_{r,i} = I_r \left(\boldsymbol{\omega}^{\text{B/N}} - \dot{\phi}_i \hat{\mathbf{g}}_i \times \boldsymbol{\omega}^{\text{B/N}} \right) \cdot \hat{\mathbf{h}}_i + I_r \dot{\Omega}_i \quad (42)$$

The gimbal dynamics are identical to the gimbal torque in Eq. (9) for $i \in [1 \dots C]$.

The remaining equations may be determined from angular momentum balance of the entire spacecraft. The total angular momentum of the spacecraft is the sum of the angular momentum of the individual parts, or

$$\mathbf{H}_c = \mathbf{I}_{sc} \cdot \boldsymbol{\omega}^{\text{B/N}} + \sum_{i=1}^C \left[\mathbf{I}_{g,i} \cdot \left(\boldsymbol{\omega}^{\text{B/N}} + \dot{\phi}_i \hat{\mathbf{g}}_i \right) + \mathbf{I}_{r,i} \cdot \left(\boldsymbol{\omega}^{\text{B/N}} + \dot{\phi}_i \hat{\mathbf{g}}_i + \Omega_i \hat{\mathbf{h}}_i \right) \right] \quad (43)$$

This equation may also be written with the angular velocity terms gathered and spherical CMG inertia assumed (Eq. (6)). Without loss of generality, the CMG inertias are all identical and included with the body inertia, simplifying the notation

$$\mathbf{H}_c = \mathbf{I}_c \cdot \boldsymbol{\omega}^{\text{B/N}} + \sum_{i=1}^C \left[I_{cmg} \dot{\phi}_i \hat{\mathbf{g}}_i + I_r \Omega_i \hat{\mathbf{h}}_i \right] \quad (44)$$

The derivative of the angular momentum with respect to time in an inertial frame is

$$\begin{aligned}
\mathbf{H}_c^N &= \mathbf{I}_c \cdot \boldsymbol{\omega}^{B/N} + \boldsymbol{\omega}^{B/N} \times \mathbf{I}_c \cdot \boldsymbol{\omega}^{B/N} + \sum_{i=1}^C \left(I_{cmg} \ddot{\phi}_i \hat{\mathbf{g}}_i + \boldsymbol{\omega}^{B/N} \times I_{cmg} \dot{\phi}_i \hat{\mathbf{g}}_i \right) \\
&+ \sum_{i=1}^C \left[I_r \dot{\Omega}_i \hat{\mathbf{h}}_i + \left(\boldsymbol{\omega}^{B/N} + \dot{\phi}_i \hat{\mathbf{g}}_i \right) \times I_r \Omega_i \hat{\mathbf{h}}_i \right]
\end{aligned} \tag{45}$$

This equation is divided into three components along the principal axes of \mathbf{I}_c , written as $\hat{\mathbf{b}}_k$, for the full equations of motion. The component of the spacecraft's angular velocity along the direction of each principal axis is denoted u_k , $k = 1..3$.

The system of equations that results when combining the rotor, gimbal, and spacecraft dynamics in Eqs. (42), (9), and (45), respectively, is

$$\begin{aligned}
&\begin{bmatrix} \hat{\mathbf{b}}_k \cdot \mathbf{I}_c \cdot \hat{\mathbf{b}}_k & I_{cmg} \hat{\mathbf{g}}_i \cdot \hat{\mathbf{b}}_k & 0 & I_r \hat{\mathbf{h}}_i \cdot \hat{\mathbf{b}}_k \\ I_{cmg} \hat{\mathbf{b}}_k \cdot \hat{\mathbf{g}}_i & I_{cmg} & 0 & 0 \\ 0 & 0 & 1 & 0 \\ I_r & 0 & 0 & I_r \end{bmatrix} \cdot \begin{bmatrix} \dot{u}_k \\ \ddot{\phi}_i \\ \dot{\phi}_i \\ \dot{\Omega}_i \end{bmatrix} \\
&= \begin{bmatrix} -\left[\boldsymbol{\omega}^{B/N} \times \left(\mathbf{I}_c \cdot \boldsymbol{\omega}^{B/N} + I_{cmg} \dot{\phi}_i \hat{\mathbf{g}}_i + I_r \Omega_i \hat{\mathbf{h}}_i \right) + \dot{\phi}_i \hat{\mathbf{g}}_i \times I_r \Omega_i \hat{\mathbf{h}}_i \right] \cdot \hat{\mathbf{b}}_k \\ -\left(\boldsymbol{\omega}^{B/N} \times I_r \Omega_i \hat{\mathbf{h}}_i \right) \cdot \hat{\mathbf{g}}_i \\ \dot{\phi}_i \\ I_r \left(\dot{\phi}_i \hat{\mathbf{g}}_i \times \boldsymbol{\omega}^{B/N} \right) \cdot \hat{\mathbf{h}}_i \end{bmatrix} + \begin{bmatrix} \boldsymbol{\tau}_{ext} \cdot \hat{\mathbf{b}}_k \\ \tau_{g,i} \\ 0 \\ \tau_{r,i} \end{bmatrix}
\end{aligned} \tag{46}$$

where τ_{ext} is the total external moment acting on the spacecraft. The spacecraft attitude is not explicitly included in this equation and would add at least three additional states requiring integration of the angular velocities. The mass matrix in this equation is written to fill the following block form using $k \in [1..3]$ and $i \in [1..C]$:

$$\mathbf{M} = \begin{bmatrix} \text{diag } 3 \times 3 & 3 \times C & 3 \times C & 3 \times C \\ C \times 3 & & & \\ C \times 3 & & \text{diag } 3C \times 3C & \\ C \times 3 & & & \end{bmatrix} \tag{47}$$

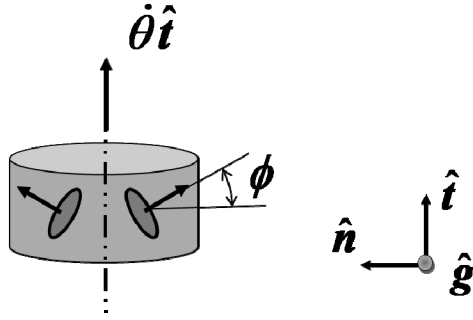


Figure 12. Single-link body controlled by gimbal angle.

To gain some insight into the dynamics of the spacecraft given in Eq. (46), consider a spacecraft with scissored-pair CMGs shown in Figure 12. The spacecraft is initially at rest, $\dot{\theta} = 0$, and the CMGs are arranged in a scissored pair. The output axis of the scissored pair is a principal axis of the spacecraft inertia dyadic I_c ; therefore, the spacecraft will only rotate about that axis in the absence of external torques. This reduced spacecraft system is identical to the single-link robot analyzed in the following chapter and has one primary degree of freedom: the spacecraft angle θ . The goal of developing control laws for this simple spacecraft system are to provide a comparison of different input variables that may be used and to show a control law that includes both gimbal and rotor torques.

Consider first a simple proportional control law. Assume that Ω is constant and the gimbal angle ϕ is the control input. The dynamics of this first-order system are captured by Eq. (39).

$$\dot{\theta} = -2I_r \Omega \sin \phi / I_c \quad (48)$$

A linearized proportional control law (for small ϕ) that drives the spacecraft to a desired angle θ_{des} is given by

$$\dot{\theta} = -2I_{r,\hat{h}} \Omega K (\theta - \theta_{des}) / I_b \quad (49)$$

where the gain K is chosen to provide the desired performance, such as the speed or steady state accuracy of driving $\theta \rightarrow \theta_{des}$.

As a second example, the control input is the gimbal rate $\dot{\phi}$, a typical approach for CMG control laws. In this case the dynamics are second order. Taking the derivative of the spacecraft dynamics in Eq. (48) yields

$$\ddot{\theta} = -2I_r \Omega \dot{\phi} \cos \phi / I_c \quad (50)$$

Combining with Eq. (48) and assuming ϕ is small yields a set of linearized equations in state-space form.

$$\begin{bmatrix} \dot{\theta} \\ \ddot{\theta} \end{bmatrix} = \begin{bmatrix} 0 & 1 \\ 0 & 0 \end{bmatrix} \cdot \begin{bmatrix} \theta \\ \dot{\theta} \end{bmatrix} + \begin{bmatrix} 0 \\ -2I_r \Omega / I_c \end{bmatrix} \dot{\phi} \quad (51)$$

The controllability matrix of this system is

$$C = \begin{bmatrix} 0 & -2I_r \Omega / I_b \\ -2I_r \Omega / I_b & 0 \end{bmatrix} \quad (52)$$

which is full rank. Therefore, the spacecraft is fully controllable with gimbal-rate control.

Controlling gimbal rate $\dot{\phi}$ requires a way to close a separate control loop from gimbal torque τ_g to $\dot{\phi}$. The spacecraft dynamics with the scissored-pair torque of Eq. (12) as the control input has four states. The spacecraft angle is measured from some arbitrary reference. Using the notation of Figure 6 and Figure 12, the governing equations of this system are

$$\begin{bmatrix} \ddot{\theta} \\ \ddot{\phi} \\ \dot{\phi} \\ \dot{\theta} \end{bmatrix} = \begin{bmatrix} 0 & -2I_r \Omega \cos \phi / I_c & 0 & 0 \\ I_r \Omega \cos \phi / I_{cmg} & 0 & 0 & 0 \\ 0 & 1 & 0 & 0 \\ 1 & 0 & 0 & 0 \end{bmatrix} \cdot \begin{bmatrix} \dot{\theta} \\ \dot{\phi} \\ \phi \\ \theta \end{bmatrix} + \begin{bmatrix} 0 \\ 1/2I_{cmg} \\ 0 \\ 0 \end{bmatrix} \cdot \tau_{sp} \quad (53)$$

The controllability matrix of this system of equations as linearized about $\phi, \theta, \dot{\phi}, \dot{\theta} = 0$ is

$$C = \begin{bmatrix} 0 & -I_r \Omega / (I_c I_{cmg}) & 0 & 0 \\ 1/2 I_{cmg} & 0 & -2(I_r \Omega)^2 / (I_c I_{cmg}) & -2(I_r \Omega)^3 / (I_c I_{cmg})^2 \\ 0 & 1/2 I_{cmg} & 0 & 0 \\ 0 & 0 & -2I_r \Omega / I_c & 0 \end{bmatrix} \quad (54)$$

which is rank deficient. Therefore the system of equations with gimbal torque control as linearized about zero has an uncontrollable mode coupling the gimbal angle to the body rate in contrast to gimbal angle or rate control. The reason for this discrepancy is that conservation of angular momentum prohibits independent control of gimbal angle ϕ and body rate $\dot{\theta}$ using internal torques, i.e., τ_{sp} , since the net angular momentum depends on both states. The eigenvalue of the uncontrollable mode is zero because the angular momentum is conserved. This implies that if the spacecraft has nonzero angular momentum when the gimbal angles are zero, no control can drive both the body rate and gimbal angles to zero. The reason gimbal angle control in Eq. (49) does not have an uncontrollable mode is because the gimbal angle is a control input instead of a state and is not subject to conservation of angular momentum. For designing a gimbal torque control law, a minimal realization of the linearized system reduces the dynamics to a third-order system and traditional methods such as LQR may be applied [Albertos and Salas, 2004].

When Ω is allowed to vary and rotor torque is included in the dynamics, the rotor speeds of the separate CMGs may be combined into one rotor speed due to the symmetry in the problem. Figure 12 shows the simple case of a body at rest with a scissored pair of CMGs as the sole means of actuation. Figure 11 suggests that an angular momentum balance of the rotors will determine the change in Ω . Given the

rotor's angular momentum in Eq. (29) and $\tau_r=0$, the rotor speed Ω for each rotor in the scissored pair is determined from Eq. (32), using the geometry shown in Figure 6 and Figure 12.

$$0 = I_r (\ddot{\theta} \sin \phi - \dot{\theta} \dot{\phi} I_r \Omega_i \cos \phi) + I_r \dot{\Omega}_i \quad (55)$$

for $i=1,2$. If $\Omega_1=\Omega_2$ at any particular time, then $\dot{\Omega}_1 = \dot{\Omega}_2$ and $\Omega_1=\Omega_2$ for all time and the subscript may again be omitted.

The equations in Eq. (46) reduces to a five-state system of equations by invoking the scissored-pair symmetry and considering only one axis of spacecraft rotation.

$$\begin{bmatrix} I_c & 2I_r \sin \phi & 0 & 0 & 0 \\ I_r & I_r & 0 & 0 & 0 \\ 0 & 0 & 2I_{cmg} & 0 & 0 \\ 0 & 0 & 0 & 1 & 0 \\ 0 & 0 & 0 & 0 & I_c \end{bmatrix} \cdot \begin{bmatrix} \ddot{\theta} \\ \dot{\Omega} \\ \ddot{\phi} \\ \dot{\phi} \\ \dot{\theta} \end{bmatrix} = \begin{bmatrix} -2\dot{\phi} I_r \Omega \cos \phi \\ -I_r \dot{\phi} \dot{\theta} \cos \phi \\ 2\dot{\theta} I_r \Omega \cos \phi \\ \dot{\phi} \\ -2I_r \Omega \sin \phi \end{bmatrix} + \begin{bmatrix} 0 & 0 \\ 0 & 1 \\ 1 & 0 \\ 0 & 0 \\ 0 & 0 \end{bmatrix} \cdot \begin{bmatrix} \tau_{sp} \\ \tau_r \end{bmatrix} \quad (56)$$

The mass matrix is written so that its inverse may be found by inverting the 2×2 block matrix and each of the remaining diagonal elements. The inverse of the 2×2 block is

$$\begin{bmatrix} I_c & 2I_r \sin \phi \\ I_r & I_r \end{bmatrix}^{-1} = \frac{1}{\det} \begin{bmatrix} I_r & -2I_r \sin \phi \\ -I_r & I_c \end{bmatrix} \quad (57)$$

$$\det = I_r (I_c - 2I_r \sin \phi)$$

The system written in first order matrix form is

$$\begin{bmatrix} \ddot{\theta} \\ \dot{\Omega} \\ \ddot{\phi} \\ \dot{\phi} \\ \dot{\theta} \end{bmatrix} = \begin{bmatrix} (\sin \phi \dot{\theta} - \Omega) 2I_r \dot{\phi} \cos \phi / \Delta \\ (2I_r \Omega - I_c \dot{\theta}) \dot{\phi} \cos \phi / \Delta \\ \dot{\theta} I_r \Omega \cos \phi / I_{cmg} \\ \dot{\phi} \\ -2I_r \Omega \sin \phi \end{bmatrix} + \begin{bmatrix} 0 & -2I_r \sin \phi / den \\ 0 & I_c / den \\ 1 / (2I_{cmg}) & 0 \\ 0 & 0 \\ 0 & 0 \end{bmatrix} \cdot \begin{bmatrix} \tau_{sp} \\ \tau_r \end{bmatrix} \quad (58)$$

where $\Delta = I_c - 2I_r \sin \phi$.

Suppose that the rotor speed is controlled by a proportional gain:

$$\tau_r = I_r \left[-K_r (\Omega - \Omega_0) + \tau_{drag} \right] \quad (59)$$

where the K_r is the proportionality gain and Ω_0 and τ_{drag} are the nominal rotor speed and rotor torque, respectively, when the spacecraft or robot arm is at rest. As K_r approaches infinity, the rotor speed approaches a constant, and the power cost of constant Ω from section A of this chapter is relevant. As the gain approaches zero, the torque also approaches zero and the error in rotor speed and spacecraft rate are determined from section B of this chapter. In practice, the gain is nonzero to allow the controller to overcome bearing friction and motor losses that may change over time.

A control law of the form in Eq. (59) has several advantages over more complex control laws while still allowing some flexibility in the gain and set-point speed chosen. First, Eq. (59) is easily implemented in the CMG electronics independent of the gimbal control. Second, knowledge of the spacecraft state is not required of the rotor controller, reducing communications bandwidth. Third, this control law is broadly applicable because it is independent of the particular CMG array used on the spacecraft.

The control law of Eq. (59) combined with the dynamics in Eq. (58) as linearized about $\phi, \theta, \dot{\phi}, \dot{\theta} = 0$ and $\Omega = \Omega_0$ yields

$$\begin{bmatrix} \ddot{\theta} \\ \dot{\Omega} \\ \ddot{\phi} \\ \dot{\phi} \\ \dot{\theta} \end{bmatrix} = \begin{bmatrix} 0 & 0 & -2\Omega_0 I_r / I_c & 0 & 0 \\ 0 & -K_r & 2\Omega_0 I_r / I_c & 0 & 0 \\ I_r \Omega_0 / I_{cmg} & 0 & 0 & 0 & 0 \\ 0 & 0 & 1 & 0 & 0 \\ 0 & 0 & 0 & -2I_r \Omega_0 & 0 \end{bmatrix} \cdot \begin{bmatrix} \dot{\theta} \\ \Omega_{err} \\ \dot{\phi} \\ \phi \\ \theta \end{bmatrix} + \frac{1}{(2I_{cmg})} \cdot \tau_{sp} \quad (60)$$

which allows for flexible gimbal torque control. Because this system is linearized about zero, the uncontrollable mode coupling gimbal angle and body rate is still

present. A linear feedback law cannot drive the gimbal angle to zero when the spacecraft is at rest. However, a variable speed rotor with nonlinear control could be used to adjust the CMG momentum to drive the gimbal angles to any arbitrary value. In practice, external torques from, e.g., thrusters, could return the CMGs to a desired resting angle.

D. Rotor Speed Conclusions

This chapter has examined the relevance of assuming a constant speed rotor while allowing spacecraft (or robot) dynamics to affect the rotor speed Ω . The energy required to maintain strictly constant Ω is equal to the energy used by the gimbals, an unacceptable cost for spacecraft applications. As Ω increases relative to the maximum angular velocity of the spacecraft or robot arm, Ω varies a fixed amount and the sensitivity of gimbal torque and CMG output torque to Ω decreases. In the limit, a high-speed CMG rotor is replaced with an angular momentum vector whose direction is controlled by the gimbal.

A linear control law about rest for a single body actuated by a scissored pair is also given. This controller demonstrates how one might control a link on a robot arm. The analysis of this chapter highlights the importance of choosing a low-bandwidth controller for the rotor speed. A spacecraft benefits from such a design because the motor can be smaller and operate at maximum efficiency by ensuring that steady state and maximum torque are similar.

CHAPTER IV. SINGLE-LINK ROBOT ARM

This section analyzes actuation of a single-link robot as a single-degree-of-freedom system to obtain an analytical expression for power used by either a joint motor between the spacecraft and robot or a scissored-pair of CMGs on the robot. The cost of additional attitude control effort when using a joint motor is not included. The differences in actuator mass are also not included. Although important trades can be made between actuator mass and system mass and performance, this paper focuses on the contribution of CMGs as joint actuators. Equal actuator mass and inertia also establishes an ‘equivalent system’ in which the CMGs are conceptually replaced with joint torques to analyze the tradeoffs associated with sizing CMGs in this or any CMG-driven system in terms of an equivalent system driven by joint motors.

E. Single-Link Analysis

The dynamics of a single-link robot with a joint motor are given first as the reference equations and are then augmented to obtain the dynamics of the CMG-driven robot.

1. Joint-torque-driven robot

Suppose the robot link’s angular momentum about the joint axis is

$$\mathbf{H}_b = \mathbf{H}_j = \mathbf{I}_b \cdot \boldsymbol{\omega}^{B/N} \quad (61)$$

Since \mathbf{v}_j , the velocity of the center of mass, is not explicitly included in \mathbf{H}_b , \mathbf{I}_b is the inertia of the link (including actuator inertia) measured about either the center of mass or an inertially fixed point, whichever intersects the joint axis $\hat{\mathbf{t}}$. The link’s inertial angular velocity $\boldsymbol{\omega}^{B/N}$ need not be parallel to the joint axis. The angular momentum derivative is

$$\dot{\mathbf{H}}_b^N = \mathbf{I}_b \cdot \dot{\boldsymbol{\omega}}^{B/N} + \boldsymbol{\omega}^{B/N} \times (\mathbf{I}_b \cdot \boldsymbol{\omega}^{B/N}) \quad (62)$$

The joint torque acting about the joint axis $\hat{\mathbf{t}}$ is given by

$$\tau_j = \mathbf{I}_b \cdot \boldsymbol{\omega}^{B/N} \cdot \hat{\mathbf{t}} + \left[\boldsymbol{\omega}^{B/N} \times \left(\mathbf{I}_b \cdot \boldsymbol{\omega}^{B/N} \right) \right] \cdot \hat{\mathbf{t}} \quad (63)$$

2. CMG-driven robot

A CMG-driven robot replaces the joint motor with the rotors and gimbals of a scissored-pair CMG. Although the CMGs likely represent a greater inertia than the joint motor, including the actuator inertia in \mathbf{I}_b for comparing CMGs and joint motors separates the obvious effects on power of increasing inertia from the remaining gyroscopic effects of the CMGs. The angular momentum of the CMG-driven robot is the same \mathbf{H}_b as for the joint driven robot with the additional angular momentum due to the CMGs.

$$\begin{aligned} \mathbf{H}_c &= \mathbf{H}_b + \mathbf{h}_{cmg1} + \mathbf{h}_{cmg2} \\ \mathbf{H}_c &= \mathbf{I}_b \cdot \boldsymbol{\omega}^{B/N} + \mathbf{I}_{cmg} \cdot \left(\boldsymbol{\omega}^{G1/B} + \boldsymbol{\omega}^{B/N} \right) + \mathbf{h}_{r1} + \mathbf{I}_{cmg} \cdot \left(\boldsymbol{\omega}^{G2/B} + \boldsymbol{\omega}^{B/N} \right) + \mathbf{h}_{r2} \end{aligned} \quad (64)$$

where $\mathbf{h}_{cmg} = \mathbf{H}_{cmg} - \mathbf{I}_{cmg} \cdot \boldsymbol{\omega}^{B/N}$. For the scissored-pair CMGs with $\mathbf{I}_{cmg1} = \mathbf{I}_{cmg2}$, the angular momentum of the gimbals cancels, i.e., $\mathbf{I}_{cmg1} \cdot \boldsymbol{\omega}^{G1/B} + \mathbf{I}_{cmg2} \cdot \boldsymbol{\omega}^{G2/B} = 0$. As indicated in Figure 6, the sum of the rotor momenta becomes

$$\mathbf{h}_{r1} + \mathbf{h}_{r2} = 2h_r \sin \phi \hat{\mathbf{t}} \quad (65)$$

With this substitution \mathbf{H}_c reduces to

$$\mathbf{H}_c = \mathbf{I}_b \cdot \boldsymbol{\omega}^{B/N} + 2h_r \sin \phi \hat{\mathbf{t}} \quad (66)$$

The only difference between \mathbf{H}_j and \mathbf{H}_c is $2h_r \sin \phi \hat{\mathbf{t}}$. The derivative of \mathbf{H}_c is:

$$\dot{\mathbf{H}}_c^N = \mathbf{I}_b \cdot \dot{\boldsymbol{\omega}}^{B/N} + \boldsymbol{\omega}^{B/N} \times \left(\mathbf{I}_b \cdot \boldsymbol{\omega}^{B/N} \right) + 2h_r \dot{\phi} \cos \phi \hat{\mathbf{t}} + \boldsymbol{\omega}^{B/N} \times 2h_r \sin \phi \hat{\mathbf{t}} \quad (67)$$

For the CMG-driven robot, the robot freely rotates about $\hat{\mathbf{t}}$. Therefore the projection of $\dot{\mathbf{H}}_c^N$ from Eq. (67) onto the joint axis $\hat{\mathbf{t}}$ must be zero.

$$0 = \mathbf{I}_b \cdot \boldsymbol{\omega}^{B/N} \cdot \hat{\mathbf{t}} + \left(\boldsymbol{\omega}^{B/N} \times \left(\mathbf{I}_b \cdot \boldsymbol{\omega}^{B/N} \right) \right) \cdot \hat{\mathbf{t}} + 2h_r \dot{\phi} \cos \phi \quad (68)$$

Substituting Eq. (63) leads to an expression for the gimbal rate:

$$\dot{\phi} = \frac{-\tau_j}{2h_r \cos \phi} \quad (69)$$

This equation states that the gimbal velocity becomes infinite as the gimbal angle approaches 90 deg. Also note that gimbal velocity roughly tracks the robot acceleration due to the relationship between τ_j and $\ddot{\theta}$.

3. Joint-motor and CMG power

Calculating power requires both torque and velocity about the axis of interest--the joint axis or the gimbal axis for joint-moto or CMG actuation, respectively. The scalar value of the angular velocity of the link about the joint axis is

$$\boldsymbol{\omega}^{B/N} \cdot \hat{\mathbf{t}} = \dot{\theta} \quad (70)$$

The joint-motor power is

$$P_j = |\tau_j \dot{\theta}| \quad (71)$$

Substituting the torque in Eq. (12) and the gimbal rate in Eq. (69), CMG power P_{cmg} becomes

$$P_{cmg} = \left| \left(2I_{cmg} \ddot{\phi} - 2\dot{\theta} h_r \cos \phi \right) \frac{-\tau_j}{2h_r \cos \phi} \right| \quad (72)$$

When $I_{cmg} \ddot{\phi} \ll \dot{\theta} h_r \cos \phi$, i.e., rotor momentum is the dominant term in Eq. (72), the CMG power equals the joint-motor power:

$$P_{cmg} \approx |\tau_j \dot{\theta}| \quad (73)$$

Both ϕ and h_r are eliminated from P_{cmg} when $I_{cmg}\ddot{\phi} \ll \dot{\theta}h_r \cos\phi$. A DC bias error in the gimbal angle ϕ , equivalent to a non-zero-momentum set point, would not significantly affect the power usage. Neither would misalignment of the scissored pair, which introduces a momentum bias perpendicular to the joint axis and serves only to reduce the available angular momentum from the scissored pair. In conclusion, this section provides a simple derivation of the power cost for CMGs and joint motors and shows that both are equal for $I_{cmg}\ddot{\phi} \ll \dot{\theta}h_r \cos\phi$.

F. Sizing CMGs in a Scissored Pair

Since the CMG power cost (excluding baseline losses) is on par with joint-motor power, CMG design principles for determining gimbal-motor torque and speed can be traced to the same robot link parameters that would be used to determine joint-motor sizing. These design principals are derived for specific cases of CMG-robot configurations; a later section establishes the validity of these principals for the more general equations derived above. In both the analysis and simulation, these design principles are valid only if the CMGs do not become saturated, e.g., from external torques.

CMGs on a robot arm are robust against if conservation of net robot angular momentum \mathbf{H}_c about the joint axis $\hat{\mathbf{t}}$ determines the maximum gimbal angle, ϕ_{max} based on the maximum momentum required by the robot arm. The necessary conditions for conservation of momentum about a joint provide a relationship between CMG momentum and link momentum that may be used to properly size the CMGs.

The change in \mathbf{H}_c about $\hat{\mathbf{t}}$ is

$$\frac{d}{dt}(\mathbf{H}_c \cdot \hat{\mathbf{t}}) = \frac{d}{dt}(\mathbf{H}_c) \cdot \hat{\mathbf{t}} + \mathbf{H}_c \cdot \frac{d}{dt}(\hat{\mathbf{t}}) \quad (74)$$

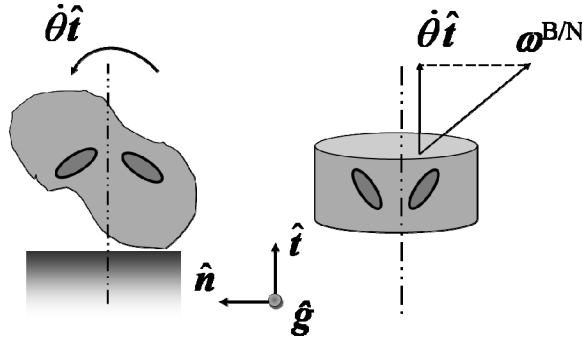


Figure 13. Valid single-link robot configurations in determining the bound on gimbal rate.

The derivatives may be taken in any reference frame since this is a scalar equation. The first term on the right is equal to the torque about $\hat{\mathbf{t}}$ and is zero for a CMG-driven robot. Substituting Eq. (66) for \mathbf{H}_c and noting that the derivative of $\hat{\mathbf{t}}$ in the inertial frame is $\boldsymbol{\omega}^{B/N} \times \hat{\mathbf{t}}$, leads to

$$\frac{d}{dt}(\mathbf{H}_c \cdot \hat{\mathbf{t}}) = (\mathbf{I}_b \cdot \boldsymbol{\omega}^{B/N} + 2h_r \sin \phi \hat{\mathbf{t}}) \cdot (\boldsymbol{\omega}^{B/N} \times \hat{\mathbf{t}}) \quad (75)$$

Rearranging terms, angular momentum is conserved about $\hat{\mathbf{t}}$ iff

$$\left[\boldsymbol{\omega}^{B/N} \times (\mathbf{I}_b \cdot \boldsymbol{\omega}^{B/N}) \right] \cdot \hat{\mathbf{t}} = 0 \quad (76)$$

Physically, Eqs. (75) and (76) state that momentum about the joint axis is conserved for the two cases illustrated in Figure 13. Either the link rotates purely about the joint axis or, for arbitrary rotation of the link, the link inertia is symmetric about $\hat{\mathbf{t}}$.

If the condition in Eq. (76) is satisfied, then a robot that starts at $\mathbf{H}_c = 0$ and $\phi = 0$ will always satisfy $\mathbf{H}_c \cdot \hat{\mathbf{t}} = 0$. From Eq. (66), $\mathbf{H}_c \cdot \hat{\mathbf{t}}$ is

$$\mathbf{H}_c \cdot \hat{\mathbf{t}} = I_{b,\hat{\mathbf{t}}} \dot{\theta} + 2h_r \sin \phi = 0 \quad (77)$$

The joint torque from Eq. (63) reduces to

$$\tau_j = I_{b,i} \ddot{\theta} \quad (78)$$

Both Eq. (77) and (78) depend on only the component of inertia about the joint axis $I_{b,i}$ as a consequence of Eq. (76), a fact verified by considering both cases shown in Figure 13. Combining Eq. (69) with Eq. (77) provides a bound on the gimbal rate for the one-degree-of-freedom robot.

$$|\dot{\phi}| < \ddot{\theta}_{max} \tan(\phi_{max}) / \dot{\theta}_{max} \quad (79)$$

This bound is conservative because the angular acceleration goes to zero when the angular velocity reaches its maximum value. The bound on $|\dot{\phi}|$ also illustrates a tradeoff between designing for a high ϕ_{max} to minimize the size and mass of the rotor versus designing for a more limited ϕ_{max} to reduce $\dot{\phi}$ and associated power costs. The simulations below suggest a maximum gimbal angle of 60 to 70 deg to balance these options.

4. Gimbal torque and torque amplification

Single-gimbal CMGs are credited with a torque-amplification property, meaning that the output to input torque ratio is much greater than one:

$$\tau_{cmg} / \tau_g \gg 1 \quad (80)$$

It can be shown that torque amplification requires that the gimbal rate $\dot{\phi}$ be much greater than the body rate $\dot{\theta}$ [Margulies and Aubrun, 1978; Lappas et al., 2002].

$$\dot{\phi} / \dot{\theta} \gg 1 \quad (81)$$

For given robot joint rate and acceleration requirements, ensuring that $\dot{\phi}$ satisfies both the condition in Eq. (81) and the bound in Eq. (79) may require artificially limiting ϕ_{max} by increasing \mathbf{h}_r .

Because this may be undesirable, an expression for the torque ratio in Eq. (80) which includes the acceleration of the body or link being actuated is found by writing the CMG output torque as the joint-motor torque of an equivalent robot. The joint torque of the equivalent system from Eq. (78) and the scissored-pair torque of Eq. (12) are combined to write a torque ratio for scissored-pair CMGs as

$$\frac{\tau_{cmg}}{\tau_g} = \frac{I_{b,i}\ddot{\theta}}{2I_{cmg}\ddot{\phi} - 2\dot{\theta}h_r \cos\phi} \quad (82)$$

A simplified version of this equation for rapid design iterations would omit the contribution of gimbal inertia and acceleration.

$$\frac{\tau_{cmg}}{\tau_{sp}} = \frac{I_{b,i}\ddot{\theta}}{2\dot{\theta}h_r \cos\phi} \quad (83)$$

Interpreting this torque input/output ratio, the CMGs amplify the input torque near $\phi = 0$, but the reverse occurs as ϕ approaches 90 deg. This analysis underscores the tradeoff between minimizing rotor size and gimbal-motor size. Interestingly, CMGs without meaningful torque amplification remove one primary objection to double-gimbal CMGs (DGCMGs): the need to transfer large torques through the gimbal motors rather than bearings [Margulies and Aubrun, 1978]. A DGCMG could reduce ACS volume [Liska, 1968], though questions remain regarding the reliability and accuracy of such a system [Liden, 1974].

When τ_{sp} is the limiting factor in a particular CMG-robot application, Eq. (16) indicates that $\dot{\theta}_{max}$ increases as h_r decreases, but conservation of angular momentum (Eq. (77)) suggests the opposite relationship. An estimate of the optimal h_r that maximizes $\dot{\theta}_{max}$ may be determined as follows. Consider a CMG robot that satisfies Eq. (66). When $\dot{\theta} = \dot{\theta}_{max}$, $\phi = \phi_{max}$ and $\ddot{\phi} = 0$. Combining Eqs. (12) and (66) gives an expression for τ_{sp} :

$$\tau_{sp} = (2h_r)^2 \sin \phi \cos \phi / I_{b,i} \quad (84)$$

The first order optimality condition determines the ϕ that maximizes τ_{sp} for a given h_r .

$$\frac{\partial \tau_{sp}}{\partial \phi} = 0 = (2h_r)^2 (\cos^2 \phi - \sin^2 \phi) / I_{b,i} \quad (85)$$

The maximum value of τ_{sp} occurs when $\phi = k\pi/4$, $k = 1, 3, 5, \dots$. Solving for h_r :

$$h_r = \sqrt{I_{b,i} \tau_{sp} / 2} \quad (86)$$

The corresponding $\dot{\theta}_{max}$ is found from Eq. (66) at .

$$\dot{\theta}_{max} = \sqrt{2\tau_{sp} / I_{b,i}} \sin \phi_{max} \quad (87)$$

A CMG-driven robot will in general present a varying inertia to its actuators since motion of outer links affects the motion of the inner links. Therefore the optimal h_r

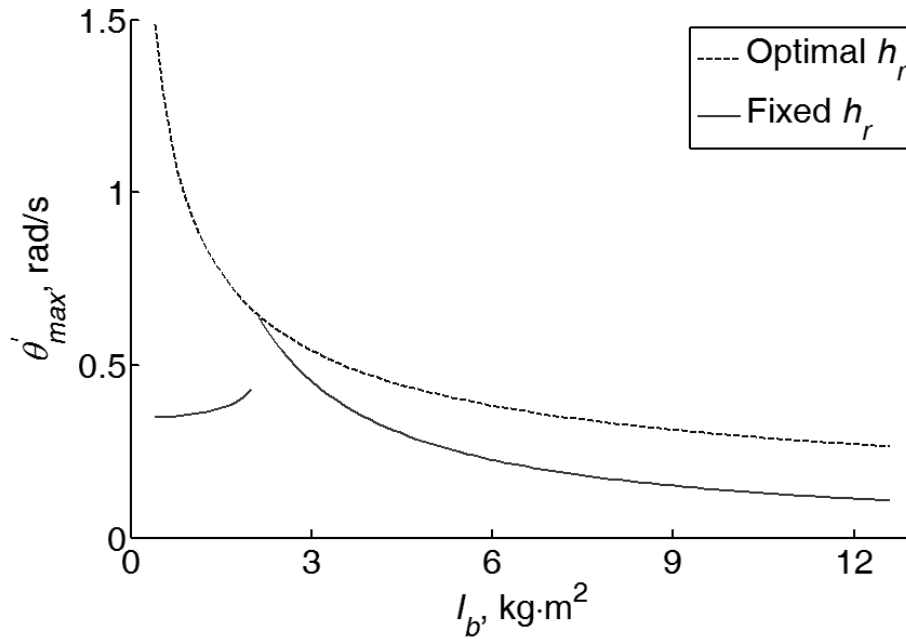


Figure 14. Maximum robot angular velocity vs. robot inertia under limited gimbal torque.

from Eq. (86) is selected for a particular robot configuration, e.g. fully extended to meet performance requirements for the greatest robot inertia taken about the shoulder joint. An abrupt change in $\dot{\theta}_{max}$ occurs for small inertias because if τ_{sp} cannot provide enough torque to reach the designed ϕ_{max} , then $\phi_{max} < \pi/4$ due to the condition given in Eq. (85). An example of a single-link robot with variable inertia due to changing payloads is given in Figure 14. This plot of $\dot{\theta}_{max}$ vs. total robot inertia compares the optimal $\dot{\theta}_{max}$ calculated when $h_r = \sqrt{I_{b,i}\tau_{sp}/2}$ to the realizable $\dot{\theta}_{max}$ when h_r is fixed over the range of inertias. If the CMG is too large for the gimbal motor, then performance is significantly less than would be predicted from conservation of angular momentum alone. The lower performance region with small robot inertias may occur during testing of a robot link not attached to a base and with hardware omitted.

5. Gimbal acceleration

The gimbal acceleration $\ddot{\phi}$ contributes to the gimbal torque (Eq. (12)) as well as the gimbal power (Eq. (72)) and the input/output torque relationship (Eq. (82)). Differentiating the gimbal rate in Eq. (69) for the case when angular momentum is conserved about the joint axis (Eq. (76)) gives an expression for gimbal acceleration:

$$\ddot{\phi} = \frac{-I_{b,i}\ddot{\theta} + 2h_r\dot{\phi}^2 \sin \phi}{2h_r \cos \phi} \quad (88)$$

Two important features of the gimbal acceleration are that $\ddot{\phi} \rightarrow \infty$ as $\phi \rightarrow 90$ deg and that finite $\ddot{\phi}$ implies finite $\ddot{\theta}$. The latter conclusion implies that the jerk of the robot link will never be infinite since infinite gimbal torque would be required.

6. Power contributors

The CMG and joint-motor power are shown to be equal in the analysis above. However, when gimbal acceleration $\ddot{\phi}$ is an important contributor to P_{cmg} , the relationship between P_{cmg} and P_j is less clear. The factors that affect the CMG power

relative to joint-motor power in the more general case determine how the simulation results later in this chapter may be scaled according to a specific set of problem parameters. A dimensionless power, \tilde{P}_{rel} , is defined as:

$$\tilde{P}_{rel} = \frac{P_{cmg} - P_j}{P_j} \quad (89)$$

When $P_j = 0$, e.g., at the start or end of a maneuver or when changing direction, \tilde{P}_{rel} becomes unbounded. Integrating power for each actuation method over the entire maneuver provides a more robust performance metric. Therefore, \tilde{P}_{rel} by itself should not be the cost function for finding an optimal actuation method and is here used only to determine scaling relationships.

To express \tilde{P}_{rel} in terms of the design parameters of the robot, Eqs. (71) and (72) are substituted into Eq. (89).

$$\tilde{P}_{rel} = \frac{-I_{cmg} \ddot{\phi}}{\dot{\theta} h_r \cos \phi} \quad (90)$$

Substituting from Eqs. (88) and (69) eliminates $\ddot{\phi}$ and $\dot{\phi}$ from this result, yielding

$$\tilde{P}_{rel} = \frac{I_{cmg} I_{b,\hat{t}}}{2\dot{\theta} h_r^2 \cos^2 \phi} \left(\ddot{\theta} - \frac{I_{b,\hat{t}} \dot{\theta}^2 \sin \phi}{2h_r \cos^2 \phi} \right) \quad (91)$$

Relative power is given as a function of time. For practical use, a time-independent scaling relationship may be obtained by evaluating the maxima of \tilde{P}_{rel} over all possible values of $\dot{\theta}$, $\ddot{\theta}$, $\ddot{\theta}$, and ϕ . Two obvious maxima occur as $\dot{\theta} \rightarrow 0$ or as $\phi \rightarrow \pi/2$ with a value of $\tilde{P}_{rel} \rightarrow \infty$. Therefore a candidate local maximum of \tilde{P}_{rel} would occur at ϕ_{max} which also corresponds to $\dot{\theta} = \dot{\theta}_{max}$ and $\ddot{\theta} = 0$. However, $\ddot{\theta}$ may be nonzero at this instant. Therefore, Eq. (91) may take a local maximum value of

$$\tilde{P}_{rel} \Big|_{\phi=\phi_{max}} = \frac{I_{cmg} I_{b,i} \ddot{\theta}_{max}}{2 \dot{\theta}_{max} h_r^2 \cos^2 \phi_{max}} \quad (92)$$

This equation shows that the power consumption of a CMG compared to a direct drive motor will be proportional to the product $I_{cmg} I_{b,i} \ddot{\theta}_{max}$ and inversely proportional to $\dot{\theta}_{max}$ and the square of $h_r \cos \phi_{max}$.

Relative power may have another local maximum for $0 < \dot{\theta} < \dot{\theta}_{max}$ corresponding to a nonzero value of $\ddot{\theta}$. To explore the relative magnitude of $\tilde{P}_{rel} \Big|_{\phi=\phi_{max}}$ as compared to the other local maximum, time histories of the link angle and gimbal angle from $\dot{\theta}_{max}/4 \leq \dot{\theta} \leq \dot{\theta}_{max}$ for values of ϕ_{max} between 55 and 80 deg are used to determine the maximum \tilde{P}_{rel} in this interval, denoted $\tilde{P}_{rel,max}$. Values of $\dot{\theta} < \dot{\theta}_{max}/4$ are likely influenced by the discontinuity in Eq. (91) at $\dot{\theta} = 0$. A plot of the relative error $\left(\tilde{P}_{rel,max} - \tilde{P}_{rel} \Big|_{\phi=\phi_{max}} \right) / \tilde{P}_{rel,max}$ in Figure 15 shows that $\tilde{P}_{rel} \Big|_{\phi=\phi_{max}}$ provides a reasonable approximation for $\tilde{P}_{rel,max}$ for $\dot{\theta}_{max}/4 \leq \dot{\theta} \leq \dot{\theta}_{max}$. This approximation is within one

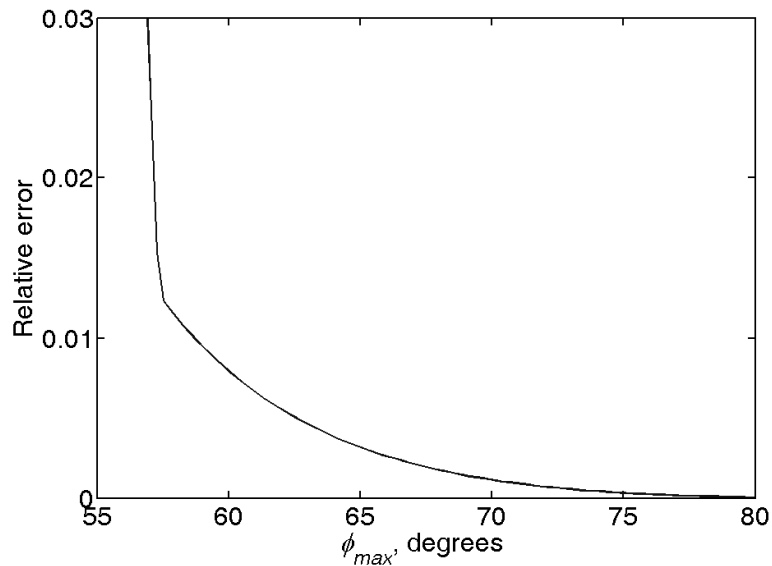


Figure 15. Relative error in \tilde{P}_{rel} . Relative error is defined as $\left(\tilde{P}_{rel,max} - \tilde{P}_{rel} \Big|_{\phi=\phi_{max}} \right) / \tilde{P}_{rel,max}$.

percent of $\tilde{P}_{rel,max}$ for $\phi_{max} > 60$ deg. Another useful expression for $\tilde{P}_{rel}|_{\phi=\phi_{max}}$ may be found by applying Eq. (77) to express \tilde{P}_{rel} independent of gimbal angle.

$$\tilde{P}_{rel}|_{\phi=\phi_{max}} = \frac{2I_{cmg}I_{b,i}\ddot{\theta}_{max}}{h_r^2 - (I_{b,i}\dot{\theta}_{max})^2} \quad (93)$$

Proper sizing of CMGs involves tradeoffs between link inertia, joint velocity, rotor momentum, and gimbal angle constrained by conservation of angular momentum about the joint axis. Although the sizing and scaling relationships of this section are derived from a scissored-pair CMG array on a robot arm, they can be extended to CMG arrays used for attitude control of satellites with the generalization that the scissored-pair gimbal angle ϕ corresponds to the angle between the rotor momentum of any active CMG in an array and the output-torque axis.

G. Single-Link Simulations

As discussed and defined above, the local maximum relative power, $\tilde{P}_{rel,max}$, gives an indication of the performance of CMGs vs. joint motors. The goal of this section is to show through simulation the effect of CMG size as driven by gimbal inertia and maximum gimbal angle by simulating a rest-to-rest maneuver. The ratio of the energy used by either CMGs or joint motors is used as an alternative to \tilde{P}_{rel} to quantify the differences in power between the two actuation methods over a complete rest-to-rest maneuver. Robot arms that do not conserve momentum about the joint axis are also simulated to explore the effect, if any, of the transverse rate of a link on CMG energy use.

1. Trajectory generation

The link motion $\theta, \dot{\theta}, \ddot{\theta}, \ddot{\theta}$ as a function of time is prescribed to facilitate comparison between joint motors and scissored pairs without confounding influences

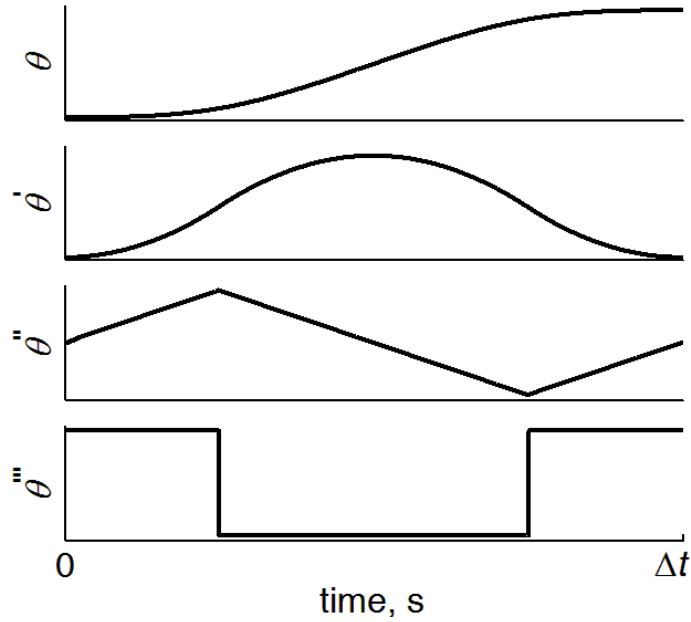


Figure 16. Joint trajectory.

from a particular control algorithm. The link is rotated through a given angle in minimum time by maximizing, in order, jerk, acceleration, and rate. The joint-angle profile, shown in Figure 16, reaches the maximum rate and acceleration for only an instant and is achieved via the following relationships among total link rotation and maximum rate, acceleration, and jerk:

$$\dot{\theta}_{max}^2 = \ddot{\theta}_{max} \cdot \dot{\theta}_{max} \quad (94)$$

$$\Delta\theta = \dot{\theta}_{max} \left(\frac{\dot{\theta}_{max}}{\ddot{\theta}_{max}} + \frac{\ddot{\theta}_{max}}{\ddot{\theta}_{max}} \right) \quad (95)$$

$$\Delta t = 4\ddot{\theta}_{max} / \ddot{\theta}_{max} \quad (96)$$

The first two relationships ensure that joint rate and acceleration just reach a maximum but do not plateau during the rest-to-rest maneuver. The final relationship determines the slew time.

The torque and power required by the joint motor and the scissored-pair CMGs are then calculated for the given trajectory. Integrating power over time provides the total energy used by each actuation method. Writing power as the product of torque and velocity, the energy used by each actuation method is, for joint-motors and CMGs respectively,

$$E_j = \int_0^{\Delta t} |\tau_j \dot{\phi}| dt \quad (97)$$

$$E_{cmg} = \int_0^{\Delta t} |\tau_{sp} \dot{\phi}| dt \quad (98)$$

The ratio of these two energies determines the relative performance of the two actuation methods in lieu of the power ratio, which, as shown above, captures the instantaneous relative performance but not the aggregate performance given by Eqs. (97) and (98).

2. Gimbal inertia and maximum gimbal angle

The first simulation explores the contribution of I_{cmg} and ϕ_{max} to E_{cmg}/E_j . A fixed I_b is maintained for all simulation runs even though I_{cmg} varies for each simulation; i.e., the inertia I_b includes CMG inertia and is identical to the I_b used for the joint-motor-driven robot, regardless of the changes in I_{cmg} . The cost of increasing gimbal inertia is thus separated from the cost of increasing the link inertia by maintaining a fixed I_b . The results are based on 30 evenly spaced values for ϕ_{max} and I_{cmg} from 1 to 1.5 rad (57-86 deg) and 0 to 0.3 kg·m² respectively, as listed in Table 2. The remaining robotic arm parameters are chosen to be unity, but they can easily be scaled to accommodate other designs. The rotor momentum is prescribed to conserve angular momentum about the joint axis across simulations (Eq. (62)).

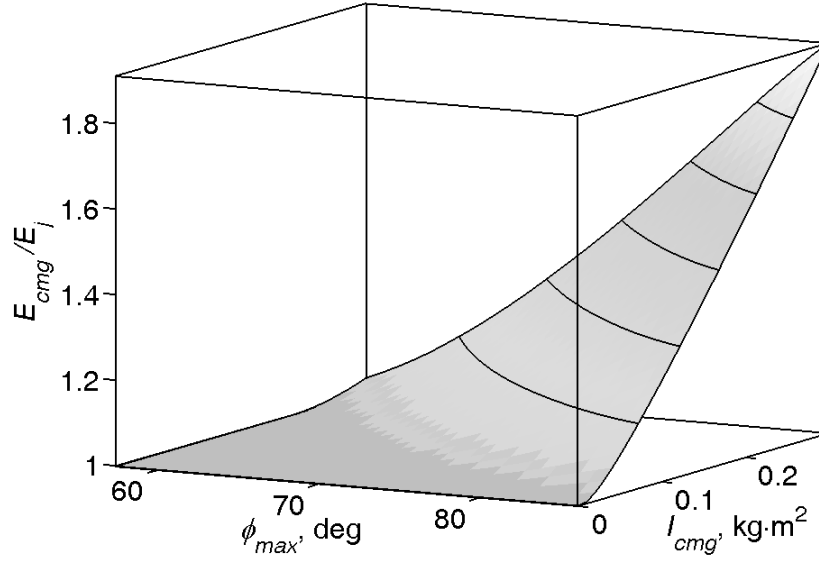


Figure 17. Gimbal inertia and maximum gimbal angle effect on CMG energy use.

Figure 17 shows the energy ratio of all the simulations. The flat region where the ratio of the energies is near unity indicates a large preferred design space for ϕ_{max} and I_{cmg} such that CMGs are about as efficient as joint motors. Note that the energy ratio increases approximately linearly with both I_{cmg} and ϕ_{max} in the plot even though $\ddot{P}_{rel,max}$ in Eq. (92) is proportional to $1/\cos^2 \phi$. This trend arises because E_{cmg} is the integral of P_{cmg} over the interval $0 \leq \phi \leq \phi_{max}$. This simulation suggests that reasonable limits for ϕ_{max} and I_{cmg} are about 70 deg and one tenth of I_b , respectively.

Table 2. Parameters for single-link simulation.

Study	$\Delta\theta$, deg	ω_{max} , s^{-1}	a_{max} , s^{-2}	j_{max} , s^{-3}	I_b , $kg \cdot m^2$	h_r , $N \cdot m \cdot s$	ϕ_{max} , deg	I_{cmg} , $kg \cdot m^2$	E_{cmg}/E_j
Gimbal properties	115	1	1	1	$1 \cdot I$	0.50— 0.59	57— 86	0— 0.3	1.0— 1.91
Body rate	"	"	"	"	0.8— 1.2	0.44— 0.65	60— 70	0.1	1.0— 1.03

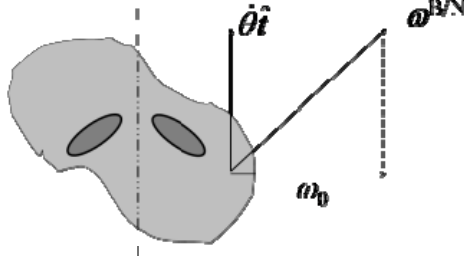


Figure 18. Transverse rate.

3. Transverse Rate

CMGs are best suited for robotic systems that conserve angular momentum about the joint axis as this avoids momentum bias that would eventually saturate the CMGs. However, momentum about any particular joint axis may not be conserved during the operation of a robot because the condition of Eq. (76) may not be satisfied for an arbitrary payload or complex motion of the robot link attached to a moving spacecraft base or other robotic links. This next simulation is of a robot arm that does not conserve momentum about its joint axis. Consider the case of a body with arbitrary inertial properties (i.e. a robot arm segment with an arbitrary payload) rotating about a transverse axis at a constant rate. This transverse rate is maintained through external means (e.g. spacecraft ACS or other links of the robot arm) while the body of interest performs the maneuver as shown in Figure 18. The angular velocity vector as written in the link's frame is $[\omega^{B/N}]^B = [\omega_1 \ \omega_2 \ \omega_3]^T$, where $\omega_1 = \dot{\theta}$ as defined in Figure 16, and ω_2 and ω_3 are constants such that total transverse rate, $\omega_0 = \sqrt{\omega_2^2 + \omega_3^2}$, is less than 1 rad/s (Figure 18).

The link inertia varies between trials by choosing physically realizable principal moments of inertia from the range given in Table 2 and arbitrarily rotating the resulting inertia matrix to introduce off-diagonal terms in the body-fixed reference frame, i.e. the joint axis is not one of the principal axes of inertia. The off-diagonal

terms ensure that the off-axis rotation contributes to the dynamics (*cf.* Eq. (76)). In a physically realizable inertia, the maximum principal inertia cannot be greater than the sum of the other two principal inertias. The inertia matrix must also be symmetric. Peck describes a method of simulating a distribution of random inertia matrices [Peck, 2006] that selects the principal inertias and randomly rotates this diagonal matrix. In this work the principal inertias are drawn from the sum of uniform distributions both for ease of use and to limit bias that could arise if the inertia were fixed to some arbitrary value. Physical but random and asymmetric inertia matrices further explore the effects of transverse rate on power and energy use but are not central to its conclusion. The variation of the inertia matrix also effectively accounts for a displaced mass center.

Since the CMG-driven robot link's angular momentum is not conserved about $\hat{\mathbf{t}}$, only the case where $\mathbf{H}_c = 0$ at $t = 0$ is considered. The rotor momentum is determined by approximating the robot momentum about the joint axis at maximum body rate using

$$\mathbf{H}_c \Big|_{\dot{\theta}=\dot{\theta}_{max}} \approx \mathbf{H}_c \Big|_{t=0} + \left[\frac{d\mathbf{H}_c}{dt} \cdot t \right]_{max} \quad (99)$$

The term in brackets is evaluated at $t=0$ and $t=\Delta t/2$ to determine its maximum value. From the link's angular momentum in Eq. (66) and zero initial momentum, combined with the change in momentum about the joint axis from Eq. (76), the rotor momentum, h_r , is found by solving:

$$\mathbf{I}_b \cdot \boldsymbol{\omega}_{max}^{B/N} \cdot \hat{\mathbf{t}} + 2h_r \sin \phi_{max} \approx 0 - \left[\boldsymbol{\omega}^{B/N} \times (\mathbf{I}_b \cdot \boldsymbol{\omega}^{B/N}) \cdot \hat{\mathbf{t}} \right]_{max} \cdot \Delta t/2 \quad (100)$$

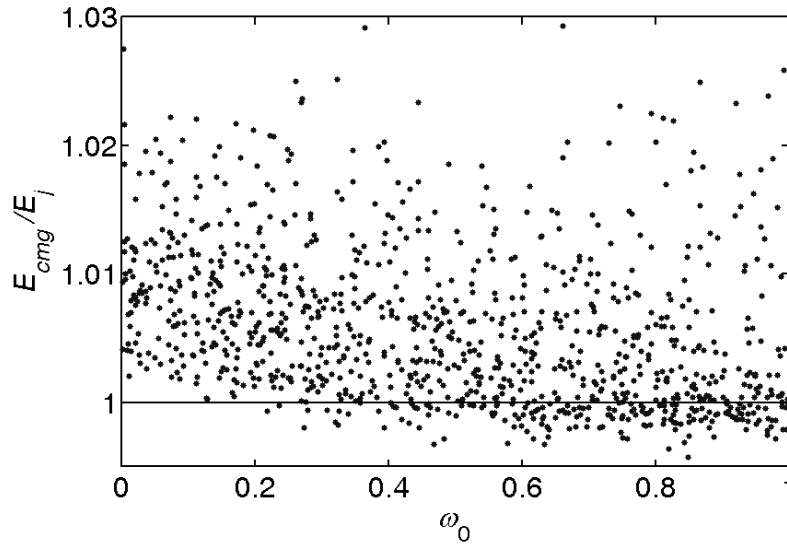


Figure 19. Energy ratio plotted against transverse rate.

The maximum gimbal angle used to calculate h_r is 70 deg (1.22 rad). Although h_r is determined from a fixed value of ϕ_{max} , the actual ϕ_{max} achieved during the simulation varies, and the range of ϕ_{max} values reported in Table 2 reflects that Eq. (100) is an approximation. The ratio of energy used by CMGs to joint motors is shown for 1000 simulations in Figure 19. Transverse rate does not appear to significantly affect the energy used by a scissored pair if the rotor momentum is appropriately sized.

This chapter demonstrates that internal momentum exchange via CMGs can be designed to use the same amount of power as joint motors. The CMG does add complexity and rotor losses associated with storing momentum when compared to joint-motors. Also, undersized CMGs and bulky gimbals add to the energy costs, but transverse-axis rotation does not. Correctly and accurately sizing the momentum requires knowledge of the bounds on link kinematics to ensure optimal CMG performance.

CHAPTER V. TWO-LINK ROBOT ARM

This chapter introduces the general equations for an n -link robot arm with CMGs, followed by specific treatment of two-link robots to highlight the key differences in the equations of motion. The two-link robot gives insight into the design considerations for multilink robots by illustrating the effect of neighboring joints on a given link based on whether joint torques or CMGs are used. Simulations reveal a power difference for different robotic motions, including some that are particularly well suited for CMGs.

With joint-motor actuation, each motor moves its own link and reacts the torques produced by links further down the chain according to the angles between the joint axes—the joint topology. Two distinct joint topologies for a two-link robot are the

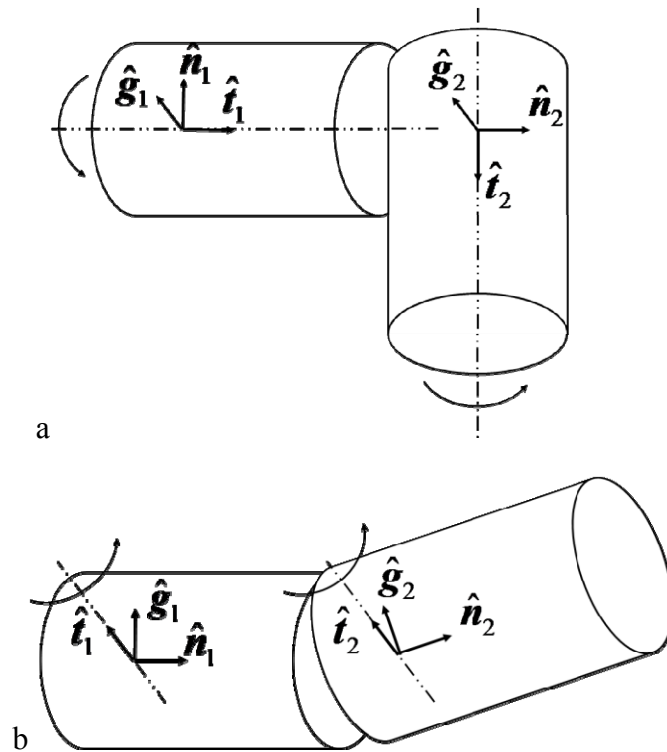


Figure 20. Joint topologies. a) Orthogonal joint axes. b) Parallel joint axes.

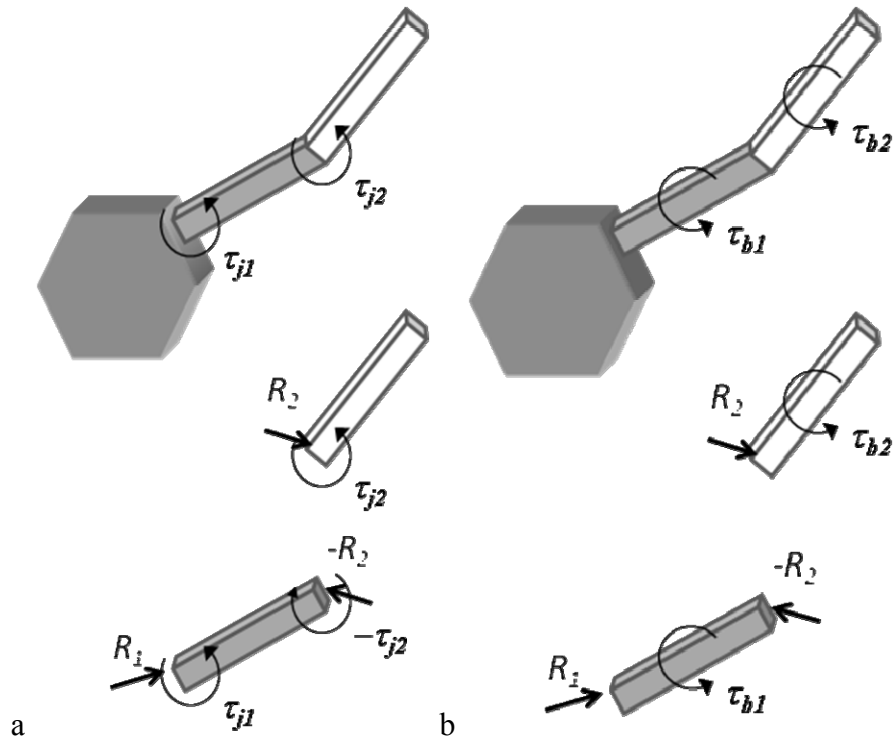


Figure 21. Free-body diagram of a two-link robot.
a. Joint torque. b. Body torque.

planar robot with parallel joint axes and a ‘pitch-roll’ robot with orthogonal joint axes, shown in Figure 20. The key difference between these two topologies is that a torque about the second joint of the ‘pitch-roll’ robot is perpendicular to the first joint axis and will be transmitted to the base via a constraint torque. Torque about the second joint of a planar robot is coupled to the first joint, as shown in the free-body diagram of a two-link robot with joint torques (Figure 21). A subscript j or b denotes joint torques and body torques. Figure 21 also shows that, as with CMGs, a body torque must have zero torque about the joint axis.

A. Multilink Robot Dynamics

The single-link robot arm with CMG actuation provides insight into the power and energy used by CMGs as a single unit. A multilink robot may gain additional

benefits with CMGs because the reactionless actuation affects not only the torques reacted onto the base but also torque reacted between links. The equations of motion for a three-link robot with scissored-pair CMG actuation have been derived by Carpenter and Peck [*Carpenter and Peck, 2008*]. They used Kane's equations [*Kane and Levinson, 1985*], equivalent to the principle of virtual power in this formulation [*Moon, 1998*], to derive the equations of motion. This work extends their analysis to n -link robots to compare joint-motor or scissored-pair CMG actuation.

Kane's equations may be written as [*Moon, 1998*]:

$$\sum_{i=1}^n \left(m_i \mathbf{v}_i^N - \mathbf{F}_i^a \right) \cdot \frac{\partial \mathbf{v}_i}{\partial \dot{q}_k} + \sum_{i=1}^n \left(\mathbf{H}_i^N - \mathbf{M}_i^a \right) \cdot \frac{\partial \boldsymbol{\omega}^{Bi/N}}{\partial \dot{q}_k} = 0 \text{ for } k = 1..n \quad (101)$$

The number of links is n , i sums over each link, and k indexes the generalized coordinates. There are n generalized coordinates for a grounded serial linkage with revolute joints. The applied forces and moments on the i th link are \mathbf{F}_i^a and \mathbf{M}_i^a ; the superscript a distinguishes them from constraint forces and moments. The partial derivatives in Eq. (101) are known as partial velocities and indicate the component of the velocity or angular rate aligned with the appropriate generalized velocity. The velocities and rates are taken with respect to an inertial frame. Each body frame is denoted Bi , with a body-fixed vector $\hat{\mathbf{t}}_i$ aligned with the i th joint axis. The zeroth link is the nonrotating N frame. The angle of rotation of each link about its joint axis is the i th generalized coordinate, q_i .

Recursive expressions for each term allow additional links to be added using the same block of code with another joint-angle command. Since this analysis uses prescribed motion, the expressions include no feedback terms. Including feedback requires an expression for the mass matrix, an exercise in algebra and indexing not

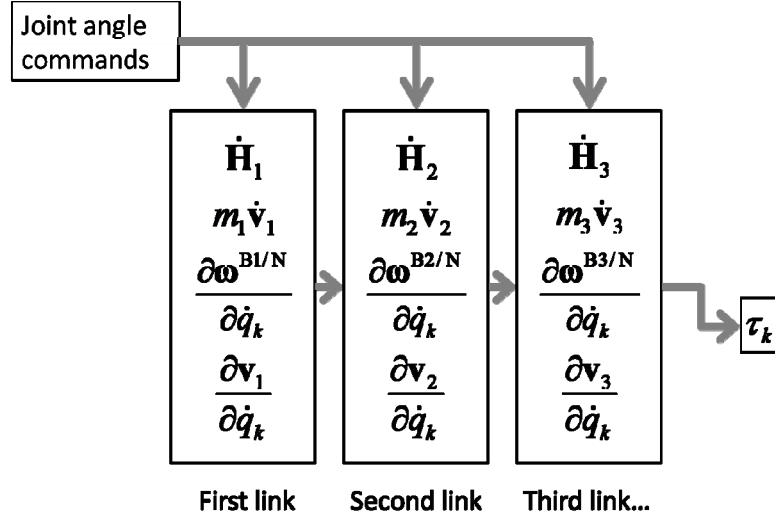


Figure 22. Code structure for n -link robot with joint motors showing recursive dependence.

included here. A schematic of the code structure for the joint-motor simulation is shown in Figure 22.

1. Joint motor actuation

The motion of the robot links is identical for both the joint-motor and CMG-driven robots. The angular velocity of the i th link with respect to the Newtonian frame is defined recursively as:

$$\omega^{Bi/N} = \dot{q}_i \hat{t}_i + \omega^{B(i-1)/N} \quad (102)$$

The angular acceleration is also given recursively:

$$\dot{\omega}^{Bi/N} = \ddot{q}_i \hat{t}_i - \dot{q}_i \hat{t}_i \times \omega^{B(i-1)/N} + \dot{\omega}^{B(i-1)/N} \quad (103)$$

The angular velocity and acceleration of each link are calculated first because the other terms in Eq. (101) may be written in terms of these quantities. From Eq. (102), the partial angular velocity term in Eqs. (101) may be concisely written as:

$$\frac{\partial \boldsymbol{\omega}^{\text{Bi/N}}}{\partial \dot{q}_k} = \begin{cases} \hat{\mathbf{t}}_k & k \leq i \\ \mathbf{0} & k > i \end{cases} \quad (104)$$

The angular momentum of the joint-motor actuated link i and its derivative are given in Eqs. (61) and (62). Letting \mathbf{I}_i denote the inertia of link i and its actuator, $\mathbf{H}_{j,i}^{\text{N}}$ for an n -link robot is

$$\mathbf{H}_{j,i}^{\text{N}} = \mathbf{I}_i \boldsymbol{\omega}^{\text{Bi/N}} + \boldsymbol{\omega}^{\text{Bi/N}} \times \mathbf{I}_i \boldsymbol{\omega}^{\text{Bi/N}} \quad (105)$$

The applied moments on link i from the joint motors are

$$\mathbf{M}_{j,i}^a = \tau_{j,i} \hat{\mathbf{t}}_i - \tau_{j,i+1} \hat{\mathbf{t}}_{i+1} \quad (106)$$

The applied moments become much less cumbersome after summing over all the links. The k th equation from Eq. (101) has a single torque term after taking the sum of applied moments projected onto the space of partial angular velocities:

$$\sum_{i=1}^N \mathbf{M}_{j,i}^a \cdot \frac{\partial \boldsymbol{\omega}^{\text{Bi/N}}}{\partial \dot{q}_k} = \sum_{i=k}^N \left\{ (\tau_{j,i} \hat{\mathbf{t}}_i - \tau_{j,i+1} \hat{\mathbf{t}}_{i+1}) \cdot \hat{\mathbf{t}}_k \right\} \quad (107)$$

$$\sum_{i=1}^N \mathbf{M}_{j,i}^a \cdot \frac{\partial \boldsymbol{\omega}^{\text{Bi/N}}}{\partial \dot{q}_k} = \tau_{j,k} \quad (108)$$

The dynamics due to the acceleration of the centers of mass of each link are not addressed in the single-link analysis. The first sum in Eq. (101) includes such dynamics. In a single link, these effects can be included by augmenting the inertia matrix in the equations of motion. The geometry of the robot is defined as follows. Let \mathbf{l}_i be the vector from the i -frame origin to the $i+1$ -frame origin, and let \mathbf{r}_i be the vector from the i -frame origin to the center of mass of link. The position, \mathbf{R}_i , and velocity, \mathbf{v}_i , of the i th link relative to the inertial frame origin are written recursively as

$$\mathbf{R}_i = \sum_{m=1}^{i-1} \mathbf{l}_m + \mathbf{r}_i \quad (109)$$

$$\mathbf{v}_i = \dot{\mathbf{R}}_i = \sum_{m=1}^{i-1} \boldsymbol{\omega}^{Bj/N} \times \mathbf{l}_m + \boldsymbol{\omega}^{Bi/N} \times \mathbf{r}_i \quad (110)$$

The acceleration of link i is

$$\mathbf{v}_i = \sum_{m=1}^{i-1} \left\{ \boldsymbol{\omega}^{Bm/N} \times \mathbf{l}_m + \boldsymbol{\omega}^{Bm/N} \times (\boldsymbol{\omega}^{Bm/N} \times \mathbf{l}_j) \right\} + \boldsymbol{\omega}^{Bi/N} \times \mathbf{r}_i + \boldsymbol{\omega}^{Bi/N} \times (\boldsymbol{\omega}^{Bi/N} \times \mathbf{r}_i) \quad (111)$$

The corresponding partial velocities are

$$\frac{\partial \mathbf{v}_i}{\partial \dot{q}_k} = \begin{cases} \hat{\mathbf{t}}_k \times \left(\mathbf{r}_i + \sum_{\substack{m=k \\ k \neq i}}^{i-1} \mathbf{l}_m \right) & i \geq k \\ 0 & i < k \end{cases} \quad (112)$$

With no applied forces in the problem, $\mathbf{F}^a=0$.

2. CMG actuated robot

As is the case for the single-link equations, the equations for the multibody CMG-driven robot arm share most of the terms from the equations for the joint-motor-driven robot arm. The only difference is that there are no applied joint torques, i.e., the gimbal motor is considered an internal force and

$$\sum_{i=1}^N \mathbf{M}_i^a \cdot \frac{\partial \boldsymbol{\omega}^{Bi/N}}{\partial \dot{q}_k} = 0 \quad (113)$$

Instead, motion is controlled with internal angular momentum from the CMGs. The angular momentum of a link and its CMGs is given by Eq. (66). The angular momentum derivative given by Eq. (67) for a single link takes the same form for the i th link:

$$\mathbf{H}_{c,i}^N = \mathbf{I}_i \cdot \boldsymbol{\omega}^{Bi/N} + \boldsymbol{\omega}^{Bi/N} \times (\mathbf{I}_i \cdot \boldsymbol{\omega}^{Bi/N}) + 2h_{r,i} \dot{\phi}_i \cos \phi_i \hat{\mathbf{t}}_i + \boldsymbol{\omega}^{Bi/N} \times 2h_{r,i} \sin \phi_i \hat{\mathbf{t}}_i \quad (114)$$

This equation is projected onto the partial velocities in Eq. (104). The equations of motion for the CMG-actuated robot are related to the equations of motion for the joint-motor-driven robot by the following:

$$\sum_{i=1}^n \mathbf{H}_{c,i}^N \cdot \frac{\partial \boldsymbol{\omega}^{Bi/N}}{\partial \dot{q}_k} = \sum_{i=1}^n \mathbf{H}_{j,i}^N \cdot \frac{\partial \boldsymbol{\omega}^{Bi/N}}{\partial \dot{q}_k} + 2h_r \dot{\phi}_i \cos \phi_i \hat{\mathbf{t}}_i \cdot \hat{\mathbf{t}}_k + \boldsymbol{\omega}^{Bi/N} \cdot (2h_r \sin \phi_i \hat{\mathbf{t}}_i \times \hat{\mathbf{t}}_k) \quad (115)$$

for $k \leq i$. The equations of motion for the joint-motor driven robot can be assembled into the following form with a mass matrix M and the velocity product terms V [Moon, 1998].

$$M(\Theta, \dot{\Theta}) \ddot{\Theta} + V(\Theta, \dot{\Theta}) = T \quad (116)$$

The n joint angles, rates, and accelerations and the joint torques are the elements of the arrays Θ , $\dot{\Theta}$, $\ddot{\Theta}$, and T . The same left-hand side of this equation can be used to express the motion of a CMG-driven robot. Including the gimbal dynamics results in a differential equation in both joint angles Θ and the gimbal angles Φ .

$$M(\Theta, \dot{\Theta}) \ddot{\Theta} + V(\Theta, \dot{\Theta}) = -B(\Theta, \dot{\Theta}, \Phi) - P(\Theta, \Phi) \dot{\Phi} \quad (117)$$

The matrix P is an upper-triangular matrix that reflects the alignment of an outboard scissored pair with the inboard link of interest. In other words, once T has been determined for an equivalent robotic system, the gimbal trajectories may be determined by:

$$T = -B(\Theta, \dot{\Theta}, \Phi) - D(\Theta, \Phi) \dot{\Phi} \quad (118)$$

The Φ are then used with Eq. (12) to find the gimbal torques. Implementation of a CMG-robot control scheme could consist of a standard control algorithm for T and a nested control algorithm for Φ .

A. Two Link Simulations

A robot with orthogonal joint axes is contrasted with a robot with parallel joint axes as two possible joint topologies for a two-link robot. For example, the first provides orientation control with two degrees of freedom (e.g., azimuth and elevation) for pointing a sensor at a target. The latter provides range for reaching tasks for a manipulation robot on a spacecraft. These two cases represent two extremes of the potential differences between CMG torques and joint torques on a two-link robot.

1. *Link rate and CMG size*

For both joint topologies, the mass properties and motion of the outer link affect CMG sizing through the total angular momentum of the robot. The net angular velocity of the outer link includes a component from the first joint that can project along the second joint axis because the joint axes are not necessarily principal axes of inertia. Therefore sizing the CMGs on a two-link robot requires careful bookkeeping of a time-varying inertia and angular velocities of the links. The CMGs on a multi-link robot could be sized according to the expected maximum angular momentum about each joint. An economic alternative used in these simulations is to place identical CMGs on each link and adjust the maximum joint velocity so that the net angular momentum is bounded by the capacity of the CMGs. The maximum angular velocities that do not saturate the CMGs are determined using an expanded version of the approximate change in momentum about the joint axis from Eq. (100). The angular momentum about each joint axis depends on the rate about both axes, yielding a system of two equations that is quadratic in the joint velocities.

Table 3. Parameter value ranges for two-link simulations.

The two entries per row in the columns under intermediate calculations correspond to the first link (top) and second link (bottom).

	Parameters		Monte Carlo Inputs				
	I_{cmg} , kg·m ²	h_r , N·m·s	$I_{b,i}$ kg·m ²	$r(i)$, m	$l_1(i)$, m	Δt_0 , s	sign($\Delta\theta$)
Ortho	0.1	0.53	0.8–1.2	-0.5– 0.5	-1–1	0–4	+/-
Parallel	0.1	0.53	0.8–1.2	-0.5– 0.5	-1–1	0–4	+/-

	Intermediate calculations				Result
	ω_{max} , s ⁻¹	I_{max} , kg·m ²	ϕ_{max} , deg	$\Delta\theta$, deg	E_{cmg}/E_j
Ortho	0.1–0.5	1.9–6.1	7–74	10–59	1–1.33
	0.6–1.2	0.8–1.6	50–80	65–134	
Parallel	0.03–1.0	1.0–4.0	3–73	4–112	-0.49–1.38
	0.0–0.9	0.9–1.5	1–73	0.2–98	

For this exploratory study, the maximum acceleration and jerk are arbitrarily set to the same numerical value as the adjusted maximum angular velocity to satisfy Eq. (94). The angle of rotation and slew duration are given by Eqs. (95) and (96). The start time of the rotations is offset by Δt_0 , with either joint randomly assigned to move first. The parameters used for a 1000 trial simulation are given in Table 3. The principal inertias, center-of-mass offset, and joint axis locations are randomly assigned component-wise from a uniform distribution over the range given in Table 3. The uniform distribution is merely meant to provide a qualitative assessment, not to encourage statistical inferences from the outputs. The maximum inertia about the joint axis, the maximum body rate, and maximum gimbal angle are calculated from the assigned parameters. Table 3 also gives ranges for these values.

2. Orthogonal joint axes

The equations of motion are decoupled if the following conditions hold: the joint axes are orthogonal, the outer link is axisymmetric about its joint axis, and the two

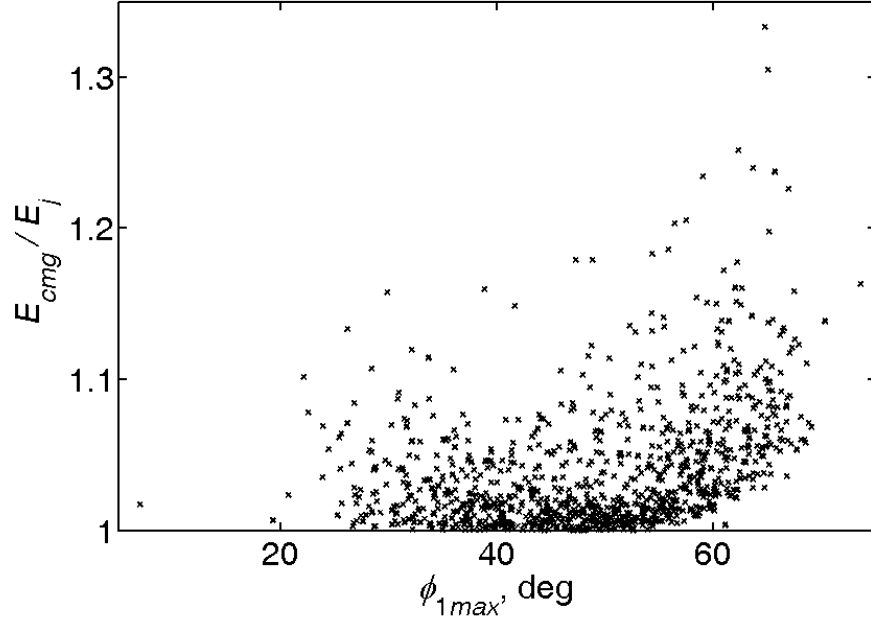


Figure 23. Performance of CMGs on robot arm with orthogonal joint axes.

joint axes intersect. These conditions also satisfy conservation of momentum about the joint axes stated in Eqs. (74) through (76), adjusted for the two-link robot. In such a case, the power performance is calculated as for two independent single links. The simulations below specifically offset the joint axes, translate the centers of mass, and include off-diagonal terms in the inertia matrices to avoid repeating the results of CHAPTER IV.

Figure 23 is a plot of the energy ratio for the two-link robot as a function of the maximum gimbal angle of the inner link, ϕ_{1max} . The greater inertia about the first joint axis causes the inner link's gimbal angle to influence the energy ratio more than the outer link's gimbal angle as shown in Figure 23. The effect of the combined inertia of the links about the first joint axis is included in ϕ_{1max} through Eq. (100). As with the single link robot, the energy ratio is greater than zero with some dependence on the size of the CMG as represented by the maximum angle for the first gimbal. However,

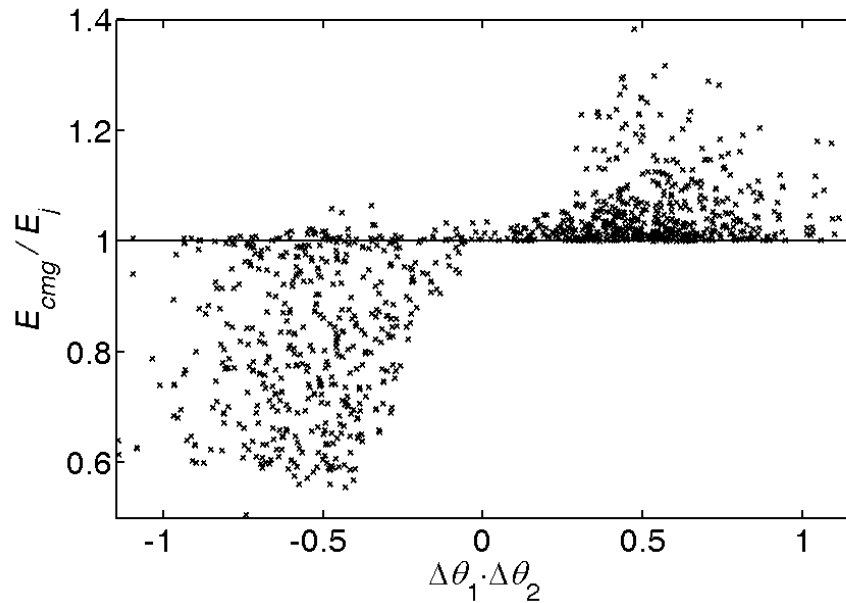


Figure 24. Joint-angle command product as an indicator of performance for parallel joint axes.

some trials in this simulation are not very power efficient due to increased inertia about the joint axes without a corresponding decrease in the other terms of the relative power in Eq. (92).

3. Parallel joint axes

None of the simulations thus far have indicated that CMGs offer an advantage in terms of power and energy over joint motors. In the simulations below, identical CMGs are again used on each link and the maximum joint rate is adjusted in accordance with the momentum capability of the scissored pair. For parallel joint axes, the sign of each joint's rotation is critical in determining the maximum joint rate. When both joints move together, the outer link saturates its CMGs more easily because both joint velocities add to determine the link's angular velocity with respect to ground. When the joints move in opposite directions, the outer link can attain a high joint rate while keeping the angular momentum low. The maximum joint velocities are

determined from the CMG momentum by taking the individual joint velocity if they are opposite sign or the sum of the two if they share the same sign. Zero velocity of either link is possible due to the start-time offset Δt_0 .

For 1000 trials over the same range of parameters as the orthogonal-axes case, the energy ratio is less than zero for 403 trials. Figure 24 shows the values of the energy ratio plotted against the sign of the product of the joint angle commands. The results show that CMGs are more efficient than joint motors when the joints move in opposite directions, as they must for reaching tasks. Joint motors represent a more power-efficient choice when the joints move together, e.g. overhand throwing motions.

CHAPTER VI. ENERGETICS OF ROBOT ACTUATION USING JOINT AND BODY TORQUES

The application of robotics in space, biology, microelectromechanical systems (MEMS), and other fields creates new applications and areas of research. Often, different types of actuation must be developed and studied to meet the specific demands of a given area, e.g. muscles in biological systems, or electromagnetic field interactions for MEMS. This chapter builds on recent work in space robotics and momentum-based actuation by generalizing earlier results on power differences between direct joint actuation and control-moment-gyroscope (CMG) actuation [*Carpenter and Peck, 2008; Brown and Peck, in review*].

Momentum-based actuation is currently used for spacecraft attitude control when applying external forces would require a greater supply of fuel than can be economically transported to space. Reaction wheels or CMGs are two common methods of controlling spacecraft orientation through internal momentum exchange. A system, such as a satellite, that uses no external forces to control its motion is termed a reactionless system in this work. When these same momentum-exchange actuators control a robot arm [*Carpenter and Peck, 2008*], this reactionless property is preserved in the sense that the actuator does not react additional torques against the base [*Carpenter and Peck, in review; Brown and Peck, in review*]. However, the motion of the center of mass of the arm may generate other constraint forces and torques between the robot and the base as stated by D'Alembert's Principle.

The CMGs produce torque on a body by providing an inertial base against which a gimbal motor may act. The dynamics of the CMGs affect the direction and magnitude of the resulting output torque, but the power delivered by the CMG is conserved in the limit of an ideal CMG [*Brown and Peck, in review*]. This chapter

provides an analytical link between a CMG-actuated robot and a robot with direct joint-torque actuation by conceptualizing the CMG's output torque as a body torque applied at the center of mass of the body. The direction of the CMG's output torque is constrained to a single, body-fixed axis by using scissored-pair CMGs [Yang *et al.*, 1995; Havill and Ratcliff, 1964]. However, replacing CMGs with idealized body torques will not account for two important and related limitations of the physical robot. First, CMGs are limited by the angular momentum stored in their rotor in that external torques cause a change in the total angular momentum of the robot that may saturate the CMGs. Second, complex motion of the robot may alter the direction of the angular momentum so that the direction of the CMG output torque is not constant with respect to the robot link. A hybrid robot with both CMGs and joint torques could help overcome the former limitation, and the second would necessitate more complex analysis of the robot.

Other applications that could use body torques (either from CMGs or other actuation methods) include robots with a thrust available along a single body-fixed direction. For example, CMGs have been proposed for steering control on an autonomous underwater vehicle (AUVs) [Thornton *et al.*, 2005]. Surgical probes inside a flexible needle are steered by controlling the orientation of the tip [Webster III *et al.*, 2006]. Greatly miniaturized CMGs could be used to augment existing strategies for needle steering. Joint torques may not be feasible in many MEMS applications. External electromagnetic fields [Bar-Cohen, 2004; Kim and Tadokoro, 2007], light [Maruo *et al.*, 2003], linear momentum [Koh *et al.*, 2002; Mita *et al.*, 2003], or even acoustic streaming [Parviz *et al.*, 2001] are all MEMS actuation methods that could be modeled as body torque for the control of a microrobot arm.

A more traditional robot configuration that is modeled like a body-torque actuated robot uses pulleys to connect the motion of the robot links to actuators attached to the

base of the robot. In a similar manner, the tendon network of the fingers or biarticulate muscles in the arms and legs affect the energetics of simple, daily tasks [Alexander, 1997; van Ingen Schenau et al., 1987]. This paper analyses only joint torques that act across a single joint between two neighboring robot links and body torques that act only between a given robot link and an inertial base.

This chapter expresses body torques in terms of the equivalent joint torques required for a given motion of a serial-link robot attached to an inertial base. A similar expression is found for an over-actuated robot with joint and body torques. Choosing the power-optimal distribution of joint and body torques is expressed as a constrained optimization problem. Simulations of a two-link planar robot show the importance of the sign of the joints' velocities in determining which actuation method uses less power. A three-link robot is used to show the added improvements in power when combined joint- and body-torque actuation is used.

A. Equations of Motion and Power

The method of virtual power [Moon, 1998] isolates the applied torques from the constraint forces and torques while maintaining vector notation throughout the derivation. For an N-link robot, the equations of motion are derived from

$$\sum_{i=1}^N (m_i \mathbf{a}_i - \mathbf{F}_i^a) \cdot \frac{\partial \mathbf{v}_i}{\partial \dot{q}_k} + \sum_{i=1}^N (\dot{\mathbf{H}}_i - \mathbf{M}_i^a) \cdot \frac{\partial \boldsymbol{\omega}_i}{\partial \dot{q}_k} = 0 \quad (119)$$

The subscript i denotes each link and q_k denotes each generalized coordinate—the joint angles between adjacent links are the generalized coordinates used throughout this work. The full equations of motion for a joint-torque-driven robot as derived from this method are given in CHAPTER V. The focus of this chapter is on the relationships between the torques, power, and energy of a robot actuated by either joint or body torques.

4. Torques

Because the two robotic systems under consideration are identical in every respect except the application of torques, the equations of motion are conveniently expressed in matrix form. The generalized coordinates are the joint angles. For the joint torques, Eq. (119) can be written as

$$\mathbf{A}(\ddot{\theta}, \dot{\theta}, \theta, t) - \mathbf{T}_j = 0 \quad (120)$$

The matrix \mathbf{A} captures the kinematics of the robot by combining the mass, stiffness, and Coriolis matrices. The vector \mathbf{T}_j contains the joint torques as mapped onto the generalized coordinates. Since the work done by $\tau_{j,k}$ is $\tau_{j,k} \cdot q_k$, the k th element of \mathbf{T}_j is $\tau_{j,k}$.

When body torques provide the actuation, Eq. (119) becomes

$$\mathbf{A}(\ddot{\theta}, \dot{\theta}, \theta, t) - \mathbf{B}(\theta)\mathbf{T}_c = 0 \quad (121)$$

The \mathbf{B} matrix represents the mapping needed to align each $\tau_{c,k}$ with the generalized velocities [Duindam and Stramigioli, 2008]. The vector \mathbf{T}_c is a column vector of scalar body torques. As seen from Eqs. (120) and (121), \mathbf{B} also maps \mathbf{T}_c to the equivalent \mathbf{T}_j necessary to produce the same motion for a given set of robot parameters.

$$\mathbf{T}_j = \mathbf{B}(\theta)\mathbf{T}_c \quad (122)$$

To find \mathbf{B} from Eq. (119), the partial derivative of the angular velocity is found for a serial-link robot anchored to an inertial base with the k th joint axis denoted $\hat{\mathbf{t}}_k$.

$$\frac{\partial \boldsymbol{\omega}_i}{\partial \dot{q}_k} = \begin{cases} \hat{\mathbf{t}}_k & k \leq i \\ 0 & k > i \end{cases} \quad (123)$$

The applied moments on the i th link for the joint torques are the inner joint torque and the negative of the outer joint torque as shown in the free-body diagram in Figure 21b.

$$\mathbf{M}_{j,i}^a = \tau_{j,i} \hat{\mathbf{t}}_i - \tau_{j,i+1} \hat{\mathbf{t}}_{i+1} \quad (124)$$

Referring to Eq. (119) and Eq. (123), the total contribution of the applied joint torques to the k th equation is

$$\sum_{i=1}^N \mathbf{M}_{j,i}^a \cdot \frac{\partial \boldsymbol{\omega}_i}{\partial \dot{q}_k} = \sum_{i=k}^N \left\{ (\tau_{j,i} \hat{\mathbf{t}}_i - \tau_{j,i+1} \hat{\mathbf{t}}_{i+1}) \cdot \hat{\mathbf{t}}_k \right\} \quad (125)$$

Note that $\tau_{j,N+1}$ does not exist, reducing this summation to

$$\sum_{i=1}^N \mathbf{M}_{j,i}^a \cdot \frac{\partial \boldsymbol{\omega}_i}{\partial \dot{q}_k} = \tau_{j,k} \quad (126)$$

which agrees with the identity mapping from $\tau_{j,k}$ to q_k in Eq. (120).

For body torques, the $\mathbf{M}_{c,i}^a$ are aligned with the inboard joint axis and can be written as

$$\mathbf{M}_{c,i}^a = \tau_{c,i} \hat{\mathbf{t}}_i \quad (127)$$

The net contribution of the τ_c to the k th generalized coordinate is

$$\sum_{i=1}^N \mathbf{M}_{c,i}^a \cdot \frac{\partial \boldsymbol{\omega}_i}{\partial \dot{q}_k} = \sum_{i=k}^N \tau_{c,i} \hat{\mathbf{t}}_i \cdot \hat{\mathbf{t}}_k \quad (128)$$

For a three link robot, Eq. (128) is written in vector-matrix form as:

$$\sum_{i=1}^N \mathbf{M}_{c,i}^a \cdot \frac{\partial \boldsymbol{\omega}_i}{\partial \dot{q}_k} = \begin{bmatrix} 1 & \hat{\mathbf{t}}_1 \cdot \hat{\mathbf{t}}_2 & \hat{\mathbf{t}}_1 \cdot \hat{\mathbf{t}}_3 \\ 0 & 1 & \hat{\mathbf{t}}_2 \cdot \hat{\mathbf{t}}_3 \\ 0 & 0 & 1 \end{bmatrix} \cdot \begin{bmatrix} \tau_{c1} \\ \tau_{c2} \\ \tau_{c3} \end{bmatrix} \quad (129)$$

Thus \mathbf{B} is the upper triangular matrix whose (k,i) entry is the dot product of the unit vectors along the k th and i th joint axes where i and k refer to the i th body and k th generalized coordinate in Eq. (119). The body torques can always be written in terms of equivalent joint torques because \mathbf{B} is guaranteed to be nonsingular.

Combined joint and body torques

A more general actuation scheme combines both types of actuation. This would allow an optimal control algorithm to choose an assortment of body and joint torques to execute a maneuver. The matrix that maps from the applied torques to the generalized velocities would be the concatenation of \mathbf{B} and the identity matrices. A useful alternative that helps unify the two actuation methods is to express Eq. (119) as a combination of the relative contribution of each.

$$\mathbf{A}(\ddot{\theta}, \dot{\theta}, \theta, t) - \mathbf{B}(\theta)\mathbf{T}_c^* - \mathbf{T}_j^* = 0 \quad (130)$$

The asterisk distinguishes the torques applied to the robot with hybrid actuation from the torques of Eqs. (120) and (121). Let the joint torques in the hybrid robot be expressed as proportional to the joint torques from Eq. (120).

$$\mathbf{T}_j^* = \text{diag}(\alpha_i)\mathbf{T}_j \quad (131)$$

The α_i are the entries on a diagonal matrix that determines the relative contribution of the joint and body torques. An α of 1 indicates that τ_j from Eq. (120) is used, and an α of zero indicates that τ_c from Eq. (121) is used. The body and joint torques are related by Eqs. (122) and (131).

$$\mathbf{B}(\theta)\mathbf{T}_c^* = (\mathbf{I} - \text{diag}(\alpha_i))\mathbf{T}_j \quad (132)$$

The α_i s are chosen to achieve performance requirements or to optimize for a given cost function. A choice of α_i equal to zero or one for all time is equivalent to removing

the i th body-torque or joint-torque actuator from the robot. The optimal α_i is not necessarily between 0 and 1.

5. Angular Velocity

The angular velocity that determines the power of a joint torque is different from the angular velocity associated with a body torque. Joint torques correspond to the joint velocities, whereas body torques correspond to the angular velocity of the body taken in the reference inertial frame and aligned with the body torque direction, i.e. $\dot{\theta}_{c,i} = \boldsymbol{\omega}^{\text{Bt/N}} \cdot \hat{\mathbf{t}}_i$. For the robots considered here, the angular velocity of a given body in the inertial frame is the sum of the inboard joint velocities. The scalar component of the body velocities that aligns with the body torques in terms of the joint velocities for the three link case is

$$\begin{bmatrix} \dot{\theta}_{c1} \\ \dot{\theta}_{c2} \\ \dot{\theta}_{c3} \end{bmatrix} = \begin{bmatrix} 1 & 0 & 0 \\ \hat{\mathbf{t}}_1 \cdot \hat{\mathbf{t}}_2 & 1 & 0 \\ \hat{\mathbf{t}}_1 \cdot \hat{\mathbf{t}}_3 & \hat{\mathbf{t}}_2 \cdot \hat{\mathbf{t}}_3 & 1 \end{bmatrix} \begin{bmatrix} \dot{\theta}_1 \\ \dot{\theta}_2 \\ \dot{\theta}_3 \end{bmatrix} \quad (133)$$

Again, the tilde is used to designate a body-referenced angular velocity. If the vector of joint angles is designated as $\boldsymbol{\theta}_j$, then the body angles can be written in terms of the joint angles.

$$\dot{\boldsymbol{\theta}}_c = \mathbf{B}^T \dot{\boldsymbol{\theta}}_j \quad (134)$$

6. Power

The power associated with the body torques can now be expressed in terms of the joint torques and joint velocities. For both joint- and body-torque based robots, the total power is the sum of the power at each joint. For a perfectly restorative robot, i.e., one that fully recovers negative work, the power is the dot product of the torques and velocities for each actuation method:

$$P_{j,C} = \dot{\boldsymbol{\theta}}_j \cdot \mathbf{T}_j \quad (135)$$

$$P_{c,C} = \dot{\boldsymbol{\theta}}_c \cdot \mathbf{T}_c \quad (136)$$

Substituting from Eqs. (122) and (134), the power of this body-torque-driven robot is identical to the power from the joint-torque-driven robot.

$$P_{c,C} = \boldsymbol{\theta}_j^T \mathbf{B} \mathbf{B}^{-1} \mathbf{T}_j \quad (137)$$

For Eq. (137) to be valid, negative power at one joint cancels an equal positive power at another joint. A physical robot at a minimum loses some of the energy associated negative work from inefficiencies of power regeneration. A lossless braking mechanism does not recover any of the negative work and does not account for braking effort. For a well controlled robot, the negative power represents active braking with some amount of associated power cost. In this work, the cost of negative power is the absolute value of power. Choosing a different cost function for negative power does not in general change whether or not joint torques and body torques have different total power because one actuation method will have positive power while the other has negative power for different robot positions and motion. Total power is taken as the sum of the absolute value of the power of each actuator.

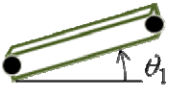
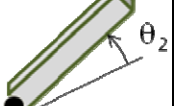
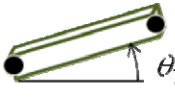
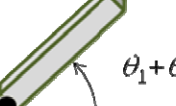
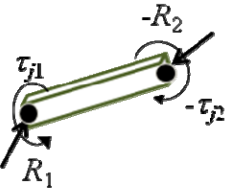
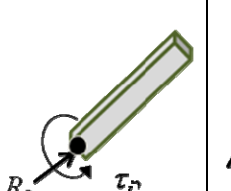
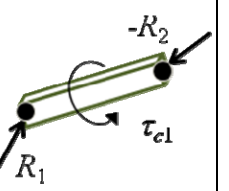
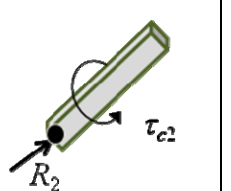
$$P_j = \sum_{i=1}^N |\tau_{j,i} \dot{\theta}_i| \quad (138)$$

$$P_c = \sum_{i=1}^N |\tau_{c,i} \dot{\theta}_{c,i}| \quad (139)$$

With the absolute value included in the summation, Eqs. (135) and (136) can no longer be used and $P_j \neq P_c$. For a hybrid robot with both types of actuators, the total power is

Table 4. Contrasting joint-torque and body-torque actuation.

For the two-link planar robot shown in Figure 21, the relationship between joint torques and body torques of an otherwise equivalent robot is illustrated with a description of the kinematics and free body diagrams for each link.

	Upper arm	Forearm	Upper arm	Forearm
Kinematics				
Free-body diagram				
Torque	τ_{j1}	τ_{j2}	$\tau_{c1} = \tau_{j1} - \tau_{j2}$	$\tau_{c2} = \tau_{j2}$
Velocity	$\dot{\theta}_1$	$\dot{\theta}_2$	$\dot{\theta}_{c1} = \dot{\theta}_1$	$\dot{\theta}_{c2} = \dot{\theta}_1 + \dot{\theta}_2$
Power	$P_{j1} = \tau_{j1} \dot{\theta}_1 $	$P_{j2} = \tau_{j2} \dot{\theta}_2 $	$P_{c1} = P_{j1} - \tau_{j2} \dot{\theta}_1 $	$P_{c2} = P_{j2} + \tau_{j2} \dot{\theta}_1 $

$$P_H = \sum_{i=1}^N |(1-\alpha) \tau_{c,i} \dot{\theta}_{c,i}| + \sum_{i=1}^N |\alpha \tau_{j,i} \dot{\theta}_i| \quad (140)$$

Power visualization for two-link robot

The difference between joint-torque power and body-torque power is illustrated with a planar, two-link robot as summarized in Table 4. The dot product of the unit vectors along the joint axes' directions is one. Therefore, the **B** matrix is [1 1; 0 1], with an inverse of [1 -1; 0 1]. The joint-torque case is the reference case and the body-torque power is expressed in terms of the joint torques and powers. The total power for the body-torque-driven robot given in Eq. (139) is

$$P_c = |(\tau_{j1} - \tau_{j2}) \dot{\theta}_1| + |\tau_{j2} (\dot{\theta}_1 + \dot{\theta}_2)| \quad (141)$$

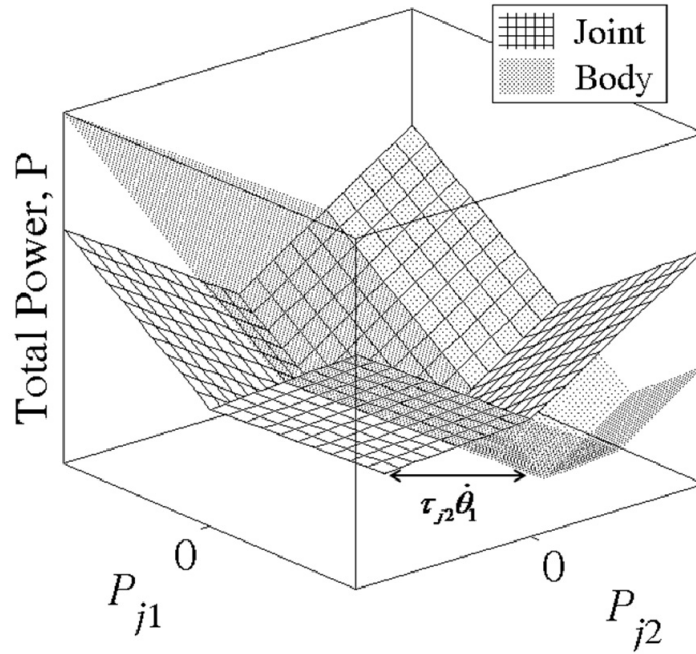


Figure 25. The total power cost as a function of the local joint power.

For a two-link planar robot, the joint-torque power is an inverted pyramid (grid). The body-torque power (grey) is the same shape but with the apex translated along the line $P_{j1} = -P_{j2}$ according to the time-changing value of $\tau_{j2}\dot{\theta}_1$. The two are equal in the overlapping regions at the front and back of the plot area.

The i th joint's power $P_{j,i}$ is defined as

$$P_{j,i} = \tau_{j,i}\dot{\theta}_i \quad (142)$$

With this definition, P_c is

$$P_c = |P_{j1} - \tau_{j2}\dot{\theta}_1| + |P_{j2} + \tau_{j2}\dot{\theta}_1| \quad (143)$$

The power for the body-torque-driven robot is a function of three values: P_{j1} , P_{j2} , and a cross-product term $\tau_{j2}\dot{\theta}_1$.

A plot of the total power as a function of $P_{j,i}$ for $i = 1,2$ is shown in Figure 25 for a positive value of $\tau_{j2}\dot{\theta}_1$. The absolute value function creates an inverted pyramid with

the apex at the origin. The body-torque power is simply the joint-torque power with the apex shifted by $\tau_{j2}\dot{\theta}_1$ along the line defined by $P_{j1} = -P_{j2}$. The combination of the absolute value as the cost function and the coordinate shift along the [1 -1] direction in the joint-power coordinates creates a significant region of equal power cost dividing the regions that favor joint torques or body torques.

Power for a Robot with Hybrid Actuation

In general, the values of α_i that minimize Eq. (140) depend on how the negative power is penalized in the cost function. A power-optimal value of α_1 can be determined independently of the other α_i s for the case of the absolute value taken as the negative power penalty function. First the total power at a given instant in time is written as a function of α_1 only; the other α_i s are fixed to some (optimal) value.

$$P_H = \left| (1 - \alpha_1) \tau_{j1} \dot{\theta}_1 + c_1 \right| + \left| \alpha_1 \tau_{j1} \dot{\theta}_1 \right| + c_2 \quad (144)$$

In this equation, τ_1 is determined from Eq. (120) and substituted into Eq. (132). The values for c_1 and c_2 are independent of α_1 and contain the other terms in the power of the first body torque (for c_1) and the body and joint torques on the other links (for c_2). The triangle inequality provides a lower bound for Eq. (144).

$$P_H \geq \left| (1 - \alpha_1) \tau_{j1} \dot{\theta}_1 + c_1 + \alpha_1 \tau_{j1} \dot{\theta}_1 \right| + c_2 \quad (145)$$

The only value of α_1 that guarantees equality in this equation is zero. Setting α_1 to zero is equivalent to removing the joint torque on the first link and only using a body torque.

The other scaling factors α_i cannot be so easily determined because they enter into multiple expressions of the body torques. The problem of determining the optimal distribution of torques between joint and body torques can be cast as a linear programming problem [Shanno and Weil, 1971] when using the absolute value as the

power cost. The vertices in the optimization function correspond to zeros in either the body- or joint-torque generated power. For a small number of links (two or three in are given as examples), the power may be calculated at these vertices and the smallest power chosen. An illustration of this method for a three-link robot is given below.

7. Energy

Power represents the instantaneous load on the power system and does not account for the amount of energy used during a complete motion of the robot. The calculated energy use for the simulations reported in this chapter is the integral of the power cost in Eq. (138) through (140).

$$E_x = \int P_x \quad (146)$$

B. Simulations

8. Two-link robot

A robot with hybrid actuation from both body and joint torques would only need three actuators for the two-link robot to minimize power: a body torque on each link and a joint torque on the second joint. The combined power for the two-link robot is

$$P_H = \min_{\alpha_2} \left| \tau_{j1} \dot{\theta}_1 - (1 - \alpha_2) \tau_{j2} \dot{\theta}_1 \right| + \left| (1 - \alpha_2) \tau_{j2} (\dot{\theta}_1 + \dot{\theta}_2) \right| + \left| \alpha_2 \tau_{j2} \dot{\theta}_2 \right| \quad (148)$$

To find the optimal α_2 requires only determining where the individual expressions each become zero. The second and third terms are zero when α_2 is one and zero, respectively. The first term is zero when $\tau_2 \neq 0$ and

$$\alpha_2 = 1 - \tau_{j1} / \tau_{j2} \quad (149)$$

The power is then calculated for three candidate values of α_2 and the minimum selected at each time point.

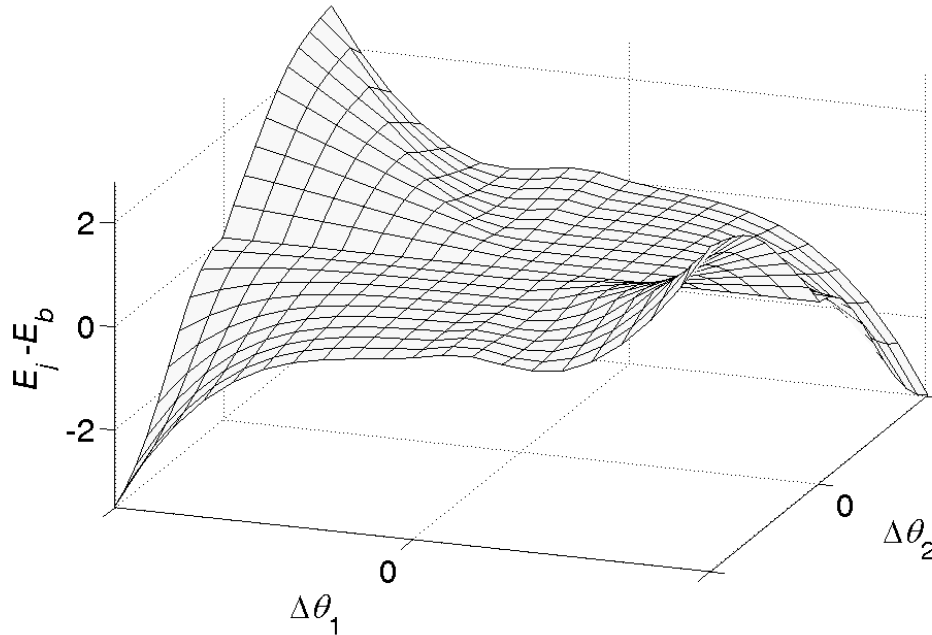


Figure 26. The difference in energy used by joint torques and body torques. *The peaks represent regions of body-torque advantage corresponding to opposite motion of each joint, whereas the valleys represent regions of joint-torque advantage corresponding to same-sign joint motion.*

In [Brown and Peck, in review], body-torque producing control-moment gyros (CMGs) provided actuation for a planar, two-link robot. The authors show that CMGs may use less energy than joint torques when the two joint angles move in opposite directions, whereas the joint torques use less energy when the joints move in the same direction. In this work, a body torque replaces the CMGs to eliminate the extra gyroscopic terms associated with CMGs. The energy used for joint torques, body

Table 5. Parameters used for the two-link simulations. The links are identical. Inertia is taken about the center of mass.

Mass, kg	Inertia, kg·m ²	r _{cm} , m	length, m
1	0.25	0.5	1

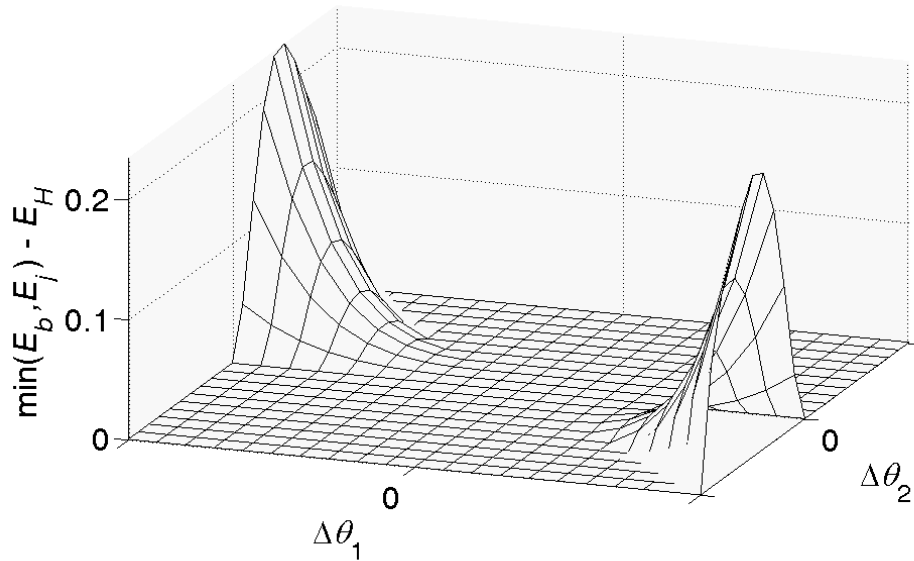


Figure 27. Benefits of combined actuation for two-link robot.
The energy used by a robot with combined body- and joint-torques is able to outperform robots with either actuation method alone for only some maneuvers.

torques, or both for a robot with parameters given in Table 5 is calculated for zero initial link angles and final angles from $-\pi$ to π .

The energy used by the body torques is compared to the energy used by the joint torques for the prescribed arm movements. The difference in energy used is shown in Figure 26, with peaks corresponding to an advantage for the body torques and valleys indicating less energy used by the joint torques. As reported earlier for CMGs [Brown and Peck, in review], the body-torque advantage occurs when the joints move in opposite directions. Figure 25 indicates that the joint power also has opposite sign for at least a portion of the robot motion.

In a two-link robot with hybrid actuation, a simple control law might choose to use all body torques or all joint torques at any given portion of the motion, depending on which actuation method would use less energy. The additional savings from letting both joint and body torques be active at one time are shown in Figure 27, a plot of

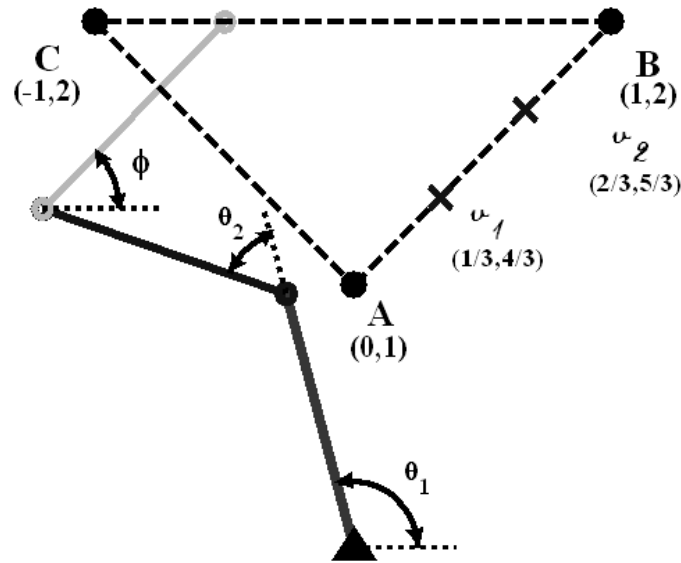


Figure 28. The closed path followed by the robot.
Each segment is defined with cubic splines through two via points. The optimization variables are the absolute angle of the third link, ϕ , and time at each via point.

difference of the energy using the simplistic control and the energy of the truly hybrid actuation. The nonzero values in Figure 27 correspond to values of α_2 not equal to either zero or one.

9. Three-Link Robot

The simulations of a two-link robot considered the same joint motion for either case. This section examines a robot with an additional degree of freedom to permit optimization of the joint trajectories of the three candidate actuation methods.

Path Optimization

The end-effector path is the triangle illustrated in Figure 28, chosen to represent a closed path in the workspace. The optimization routine uses the energy required to move the robot end-effector through this path as the cost function in determining the optimal joint trajectories. The infinite-dimension space defining all possible joint trajectories is reduced by specifying the (x,y,ϕ) position of the end effector with cubic splines and optimizing over the spline coefficients. Two via points evenly divide each

line segment into three splines with known location, smooth velocity, and continuous acceleration. The time the robot reaches each vertex of the triangle is specified, as are all the (x,y) coordinates of the vertices and via points. The optimizer chooses the time to reach the via points and ϕ at both the via points and the vertices for a total of 15 optimization variables.

The (x,y,ϕ) trajectory and sign of θ_2 fully define the joint trajectory. The sign of θ_2 is determined *a priori* and does not change during the simulation. The inverse kinematics that determine θ_1 and θ_2 for a three-link robot are given in standard robotics textbooks, such as [Murray *et al.*, 1994; Craig, 2005]. The first and second derivatives of θ_1 and θ_2 are calculated in closed form in terms of the x , y , and ϕ splines using the Jacobian of the robot.

Power of hybrid actuation

The total power for the robot with hybrid actuation for a given robot trajectory is a function of (α_2, α_3) only:

$$\begin{aligned}
P_H = \min_{\alpha_2, \alpha_3} & \left| \tau_1 \dot{\theta}_1 - (1 - \alpha_2) \tau_2 \dot{\theta}_1 \right| \\
& + \left| \left[(1 - \alpha_2) \tau_2 - (1 - \alpha_3) \tau_3 \right] (\dot{\theta}_1 + \dot{\theta}_2) \right| \\
& + \left| (1 - \alpha_3) \tau_3 (\dot{\theta}_1 + \dot{\theta}_2 + \dot{\theta}_3) \right| + \left| \alpha_2 \tau_2 \dot{\theta}_2 \right| + \left| \alpha_3 \tau_3 \dot{\theta}_3 \right|.
\end{aligned} \tag{150}$$

where the value of α_1 is zero as discussed above. The minimum value of Eq. (150) occurs when at least two of the individual absolute value terms become zero—the intersection of two edges of the cost function. The eight possible vertices used to calculate the optimal (α_2, α_3) are summarized in Table 6.

Monte Carlo Simulations

The link lengths and masses were varied to provide a comparison of the different actuation methods. The link masses and lengths were sampled from a normal distribution with mean 1 kg and 1 m, respectively, and variance 0.25 units². If the total

length of a candidate robot in the Monte Carlo simulation was less than 2.5 m, a new set of parameters was chosen until the path would be in the workspace. The inertia of each link was calculated using

$$I_i = m_i \cdot l_i^2 / 12 \quad (151)$$

Each simulation calculated the energy required for an optimal trajectory given each of the three actuation methods, i.e., three optimizations for each of the 1500 parameter sets. The Matlab optimization toolbox was used to perform the optimizations.

Although the software converged on a result for every simulation, no guarantee is made that every point represents a global optimum. However, the authors' experience with additional searches yielded answers close to the results from Matlab. Therefore, the aggregate behavior indicated in the results are likely to remain true should globally optimum results become available.

Table 6. Optimal distribution between joint and body torques.

The optimal power for a robot with combined actuation is determined by evaluating the power at each of the following eight (α_2, α_3) pairs. The zeroed terms indicate which terms in Eq. (150) are set to zero. If either τ_2 or τ_3 are zero, then the corresponding α_2 or α_3 is arbitrarily set to zero without affecting the optimal α_s .

Zeroed terms	α_2	α_3
1, 2	$1 - (\tau_1 / \tau_2)$	$1 - (\tau_1 / \tau_3)$
1, 3	$1 - (\tau_1 / \tau_2)$	1
1, 5	$1 - (\tau_1 / \tau_2)$	0
2, 3	1	1
2, 5	$1 - (\tau_3 / \tau_2)$	0
4, 2	0	$1 - (\tau_2 / \tau_3)$
4, 3	0	1
4, 5	0	0

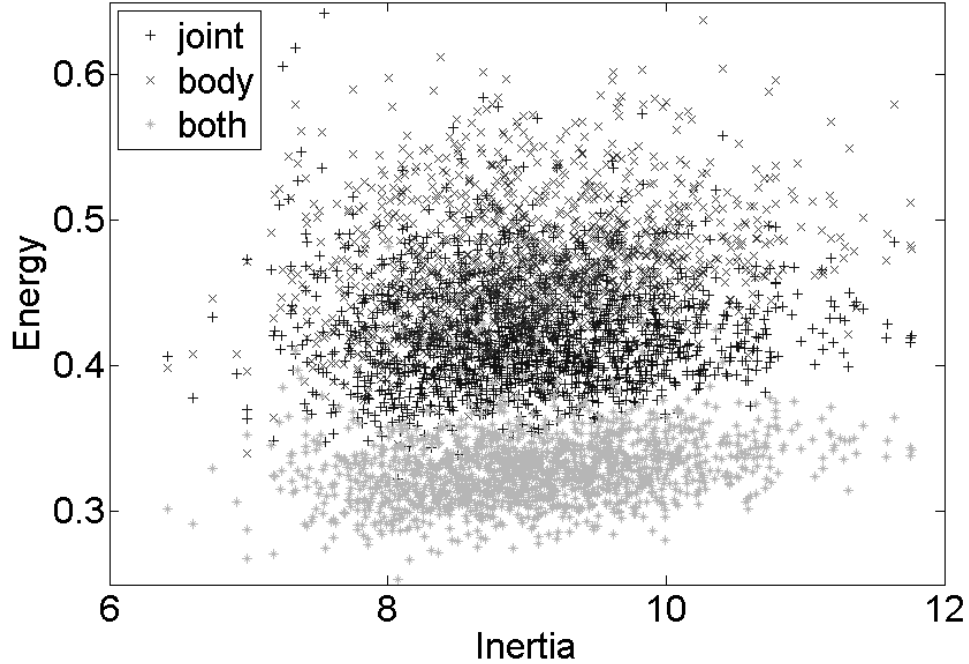


Figure 29. Energy cost of different actuation methods.
A hybrid robot with both joint and body torques available uses 21% less energy in this case study.

Results

Of the 1500 simulations run, the recorded energy for 11 of these was outside six standard deviations of the remaining values. These 11 simulations were removed from the data. The energy used by the 1489 remaining simulations is shown in Figure 29, with mean (std dev) reported in Table 7. For this particular robot setup, the joint torques outperformed the body torques. The hybrid-actuation robot did considerably better than either.

Table 7. Three-link robot results for Monte Carlo simulation.
Mean, (std dev) reported.

	Joint torques	Body torques	Combined actuation
Energy used, W	0.42, (0.04)	0.47, (0.04)	0.33, (0.02)

C. Discussion

The hybrid actuation provides more benefits than energy alone. In a space-robotics application, combined actuation also allows momentum transfer from links in the robot to the base spacecraft. Nonplanar robots do not generally conserve momentum about individual joint axes and the CMGs could saturate without the means to transfer momentum among links and with the base. A joint motor between the first link and the base does not improve energy efficiency and directly impacts the spacecraft's attitude control system. Thus the first joint motor would likely be used only for dumping momentum.

Other robotic systems that have non-identity mappings from the actuators to the joint angles are cable or tendon driven mechanisms. These mechanisms provide an interesting extension to the results in this paper. In [Murray *et al.*, 1994] a transformation matrix much like the B matrix in Eq. (121) is used to write the equations of motion for a tendon-driven robot. The flexibility in how the cables are routed means that nearly any desired structure in the B matrix can be achieved. This work supports the hypothesis that biarticular muscles in biological systems save energy as compared to uniarticular muscles [Alexander, 1997; van Ingen Schenau *et al.*, 1987].

The work in this chapter provides a framework for understanding how nontraditional actuation methods affect the power used by a robot through the structure of the mapping from actuation torques to the joint velocities. A comparison of joint torques and body torques is given, motivated by recent work on CMG-actuated robots. In a robot with hybrid actuation of both joint and body torques, the first joint torque may be omitted or left unused without sacrificing power optimality. Omitting actuation of the first joint is particularly relevant for CMG-driven robots since the CMGs on the first link react to torques from later links without transmitting

them to the base spacecraft, reducing the attitude control effort and preserving key benefits of reactionless actuation.

CHAPTER VII. CASE STUDY: CMG TESTBED

The analyses of the previous chapters are unified in an analysis of a planar testbed currently in development for CMG robot experiments. The testbed is a critical component of future work on CMG robotics and is presented as a case study of how to apply the results from the previous chapters.

Ground-based simulators for the space environment are often used for experimental validation of new ideas. Several testbeds for CMGs on single spacecraft are reported in the literature [*Lappas et al.*, 2005; *Liska*, 1968; *Peck and Cavender*, 2004; *Hall*, 2006; *Jung and Tsiotras*, 2003]. A survey of simulators using air bearings is given in [*Schwartz et al.*, 2003]. Student teams at Cornell University have previously built CMG-driven robots (Figure 30) [*Cornell CMG Team*, 2006; *Cornell CMG Team*, 2007]. They demonstrated successful operation of the CMGs on the NASA Microgravity research aircraft [*Berkowitz*, 2008]. The weightless environment

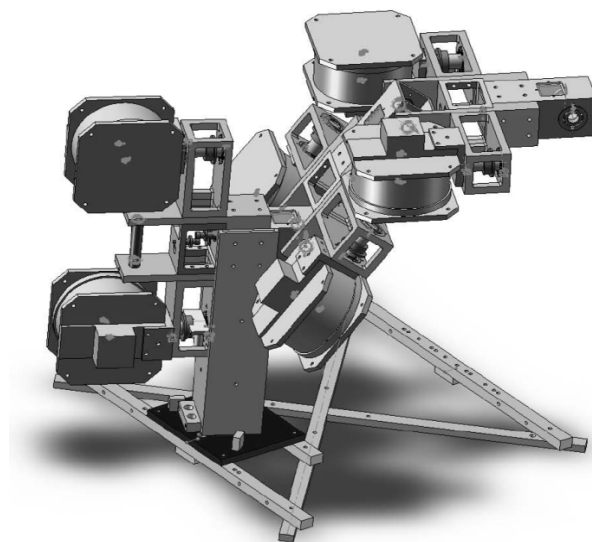


Figure 30. Robot built by Cornell CMG team.

aboard the NASA research craft allowed the student teams to test three-dimensional motion of their robot arms but limited testing to one flight per year.

A. Requirements

The primary goal of the planar testbed is to compare CMGs with joint torques on a physical robot. The results for a planar, two-link robot in Figure 24 suggest that microgravity is not necessary to achieve this goal. Therefore, the testbed seeks to modify the existing CMG robot to include air bearings to support the robot on a flat surface with joint motors added as an optional actuation method. The requirements are listed in Table 8 and are divided into system-level and flowed-down requirements, with functional and performance metrics included. Each of the three system-level requirements is discussed in the following paragraphs.

First, the testbed must allow free robot motion. Air bearings provide rotational and translational freedom within the limits of the available flat testing surface. The

Table 8. Testbed requirements

System-level requirement	Flowed-down requirements	Metrics
Unencumbered planar motion	Space for at least two robot links	Link length < 0.6 m
	Removable base	-90 to 90 deg joint range of motion
CMG and joint torque capabilities	Detachable joint motors	Two control outputs per link
	Control available to operate CMGs and joint motors together	
Measure power difference for a given maneuver	Record current and voltage at motors	Six analog inputs per link
	Use feedback control to perform identical maneuver	At least two links

testing surface is plate glass 0.013 m (0.5 in) thick and 1.22 m (4 ft) square. Glass was chosen to provide the stiffness necessary to maintain a flat surface when properly leveled so that gravity's effects would be insignificant. The test surface limits the link length to less than 0.61 m (2 ft). The CMGs from the student team were placed closer together to attain the desired size while allowing the full range of motion. The grounding link is removable to permit experiments on free-floating robots as well as validation of the analyses of earlier chapters where the base is fixed. The joint range of motion was verified early in mechanical assembly as shown in Figure 31.

Second, both CMGs and joint motors are available actuators. The joint motors are removable to avoid extra joint torques during CMG actuation. The joint motors are attached via a cogged belt so that changing from one actuation method to the other requires only removing the belt (see Figure 32). Two separate control channels from the computer permit a hybrid operation where both actuators are controlled. Communication between the computer and robot is achieved with a wireless USB hub (Belkin Wireless USB Hub) and USB DAQ board (Measurement Computing USB 1408FS).

Third, the power used by either method of actuation is recorded for direct comparison of the CMGs and joint motors. The electrical power of each motor is recorded, not the mechanical power. Joint-angle feedback helps ensure that the same base motion occurs when comparing the two actuation methods. At least two links and a ground are required to demonstrate the differences between the two actuation methods (see CHAPTER V).

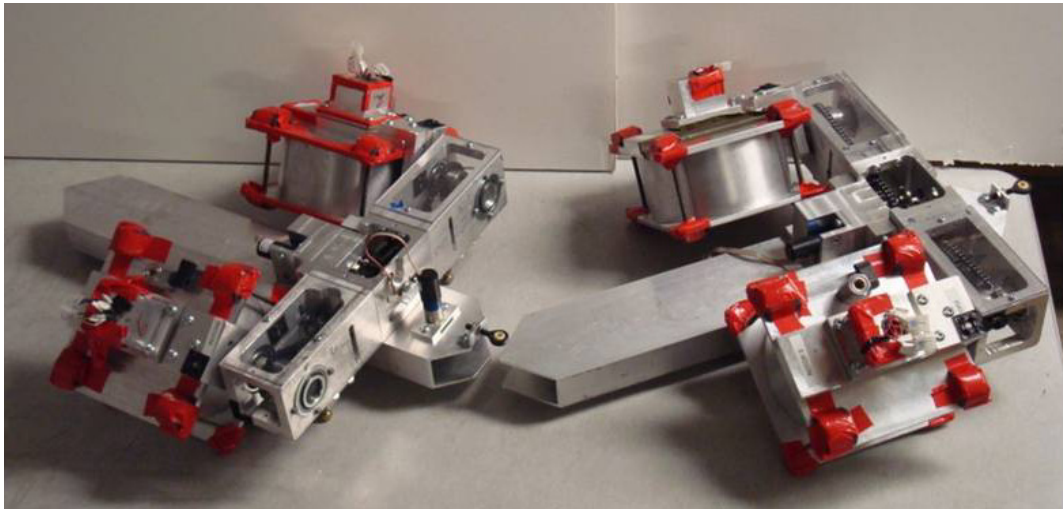


Figure 31. Two links mechanically assembled.
Joint range of motion and link length were verified during assembly. Sharp edges are protected, and the joint motor is seen in front of the gimbal structure on the left.

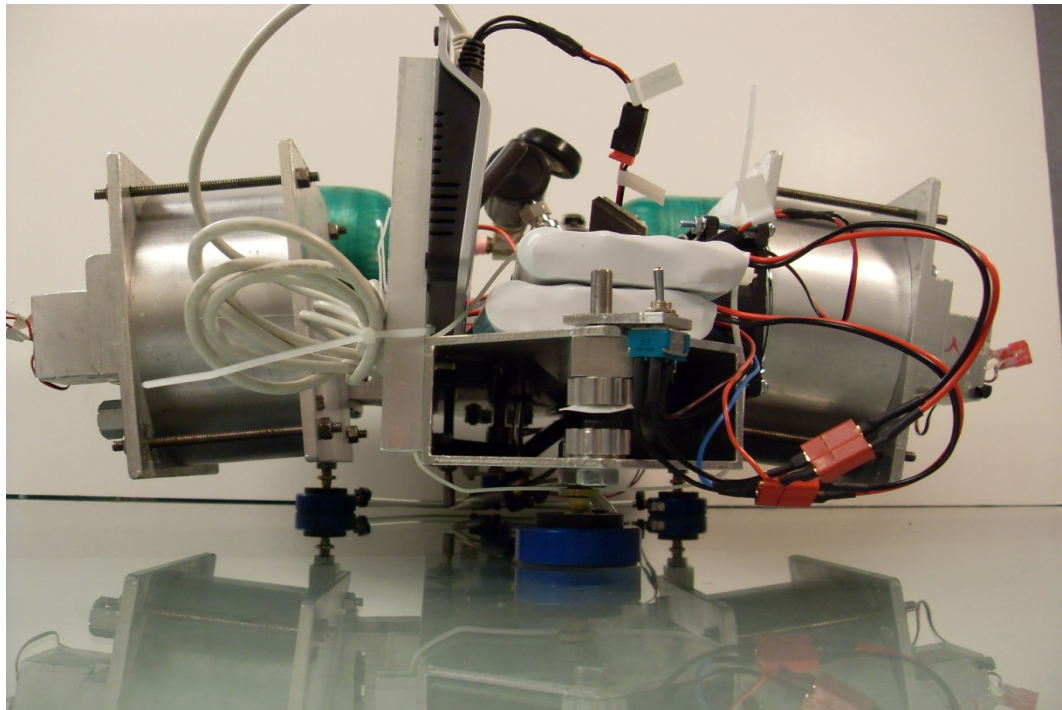


Figure 32. Front view of testbed link.
Cogs for joint-motor drive belt are visible at the front of the robot. Three air bearings provide support the robot on the glass surface. The wireless USB hub is mounted vertically on the left of the main beam for communication with main program.

B. Design

A summary of the approximate physical values of the testbed robot is given in Table 9. The parameters in Table 9 are estimated from the 2008 CMG teams' CAD models. The link mass and inertia are approximations that account for the addition of electronics and the air system. The motors purchased by the CMG team were chosen to permit $\dot{\theta}_{max} = 1$ rad/s with $\phi_{max} = 1.22$ rad (70 deg). However, τ_{sp} is limited by the existing gimbal structure for the scissored pair used on our testbed. Slippage of the cogs used to transmit torque from a central gimbal motor to each CMG limits τ_{sp} to approximately 0.5 N.

The critical design choice is the selection of h_r . A typical design application for CMGs would require a minimum output torque τ_{CMG} . However, based on the analysis of the two-link robot, $\dot{\theta}_{max}$ is chosen as the performance metric. Figures 14 and 33 illustrate how h_r and $\dot{\theta}_{max}$ interact given the limitation on τ_{sp} . The values used to

Table 9. Physical parameters inherited from the CMG team. CMG inertia is half the inertia of the scissored pair.

Rotor inertia, I_r	Rotor speed, Ω	Rotor momentum, h_r	CMG inertia, I_{cmg}
0.0023 kg·m ²	3000 rpm	0.71 N·m·s	0.009 kg·m ²
Link inertia, I_b	Distance from first joint to link center of mass, r	Link length, l	Link mass, m
0.4 kg·m ²	0.26 m	0.62 m	14 kg
Mechanical torque available, τ_{sp}, τ_j	Available power, P_c, P_j	Target gimbal torque, τ_{sp}	Link inertia about joint axis, I_{bj}
3.5 N·m	7.7 W	0.5 N·m	1.35 kg·m ²

generate Figures 14 and 33 satisfy $\tau_{sp} \leq 0.5$ N and represent the rotors spinning at 3000 rpm. For the parameters in Table 9, $h_r = 0.58$, and $\dot{\theta}_{max} = 0.8$ rad/s when $\phi_{max} = 1.22$ rad (70 deg). Even though the rotors are sized to spin at 3000 rpm, the optimal rotor speed is 2400 rpm (250 rad/s).

The optimal h_r of the preceding paragraph is for a single robot link rotating about a fixed joint, representative of the second link rotating while the first link is held fixed. The CMGs on the first link must act against the combined inertia of both links. The worst-case inertia of both links taken about the first joint is $I_{bj} = 12.6$ kg·m². The optimal h_r and corresponding $\dot{\theta}_{max}$ for $I_{bj} = 0.4$ to 12.6 kg·m² are shown in Figure 33. For a small robot, a larger CMG will not add agility unless the gimbal motor and structure is designed to support the additional loads. An interpretation of this is that

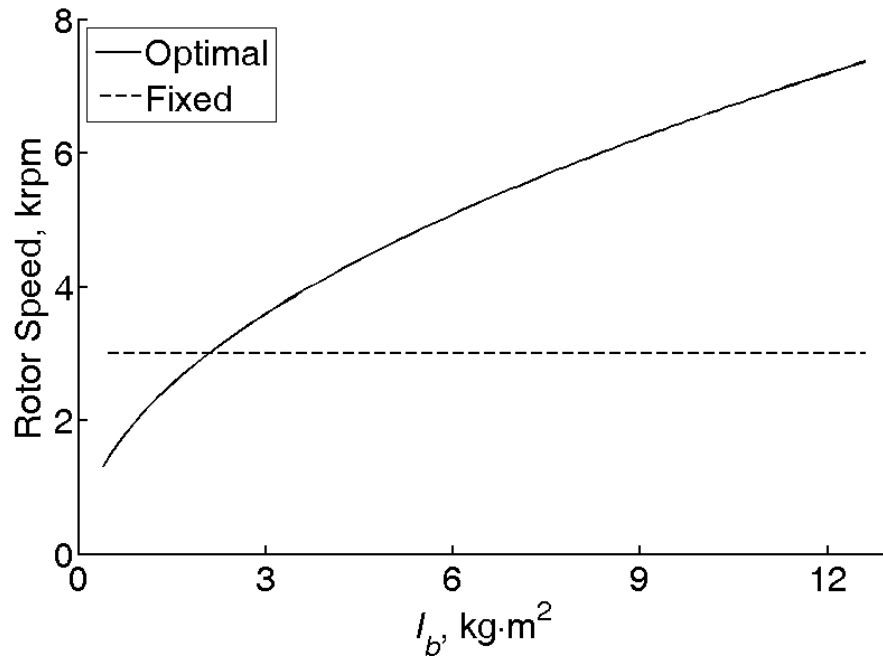


Figure 33. Rotor sizing for testbed.

The speed required for obtainin the optimal h_r for achieving a maximal $\dot{\theta}_{max}$ when τ_{sp} is restricted as compared to a fixed speed. These data correspond to the data in Figure 14.

Table 10. Robot trajectory parameters.

	Single link only	Both links
$I_{bj,i}$, kg·m ²	1.35	12.6
h_r , N·m·s	0.58	1.8
Ω , rpm	2400	7400
$\dot{\theta}_{max}$, rad/s	0.81	0.26
$\ddot{\theta}_{max}$, rad/s ²	1.3	0.14
$\dddot{\theta}_{max}$, rad/s ³	2.1	0.073
min $\Delta\theta$, rad	1.0	1.0
Δt , s $\Delta\theta = \pi/2$ rad	3.2	9.7

the CMGs provide a transmission that is inversely dependent on the robot speed, i.e., at low $\dot{\theta}$ τ_{sp} is amplified onto the robot [Lappas *et al.*, 2002], but at high speeds τ_{sp} must overcome the added gyroscopic effects of the robot motion before effectively applying torque to the robot.

The desired $\Delta\theta$, $\dot{\theta}_{max}$, and $\ddot{\theta}_{max}$ also determine if $\dot{\theta}_{max}$ is reachable by the robot. The value of $\ddot{\theta}_{max}$ is selected based on joint-motor actuation with $\tau_j = 1.75$ N, half the rated torque of the motor. For rotation of the second link only ($I_{bj2} = 1.35$ kg·m² taken about the joint axis), $\ddot{\theta}_{max} = 1.3$ rad/s². If $I_{bj1} = 12.6$ kg·m², i.e., the total inertia of the fully extended robot about the first joint, then $\ddot{\theta}_{max} = 0.14$ rad/s², and $\ddot{\theta}_{max}$ is found from Eq. (94). Equation (95) gives the minimum $\Delta\theta$ that is needed to reach $\dot{\theta}_{max}$ to verify that the joint range of motion is consistent with the other trajectory parameters. The robot trajectory parameters are summarized in Table 10.

A simulation of the testbed with a single link rotating about a fixed base produces the joint trajectory shown in Figure 34a for a $\pi/2$ rad rest-to-rest maneuver. The

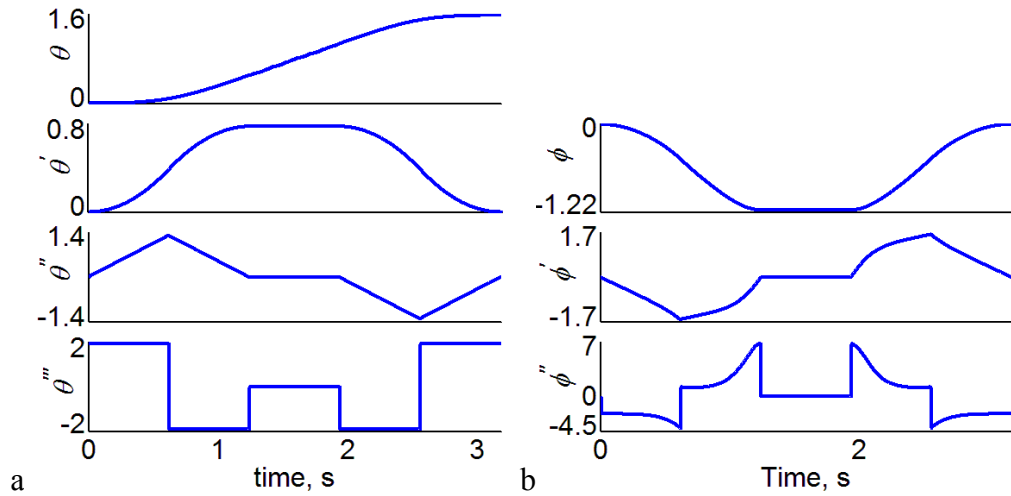


Figure 34. Joint and gimbal angle trajectories for testbed simulation.
a. The joint trajectory. b. Gimbal trajectory. Note that the gimbal position and velocity are closely related to the negative robot joint velocity and acceleration, respectively. The gimbal acceleration superimposes the robot jerk and velocity.

gimbal trajectory is shown in Figure 34b to emphasize the unique character of CMG actuation. The placement of the graphs emphasizes that the trajectories in Figure 34b represent a derivative shift from those in Figure 34a.

The torque required by either actuation method is shown in Figure 35. The joint torque closely follows $\ddot{\theta}$ as expected. In contrast, τ_{sp} does not follow $\ddot{\phi}$ closely, but is rather a blend of all the gimbal states shown in Figure 34b. The maximum power is 0.84 W for the CMGs and 0.77 W for the joint motor.

C. Conclusions

This case study of a CMG-robot testbed illustrates how the comparison of CMGs with joint motors in this dissertation may be used to size CMGs. Particular attention was given to the effect of limited gimbal torque on the optimal CMG size. The robot performance was expressed in terms of $\dot{\theta}$, $\ddot{\theta}$, and $\ddot{\phi}$ to emphasize that momentum exchange is the primary means of operation for CMGs.

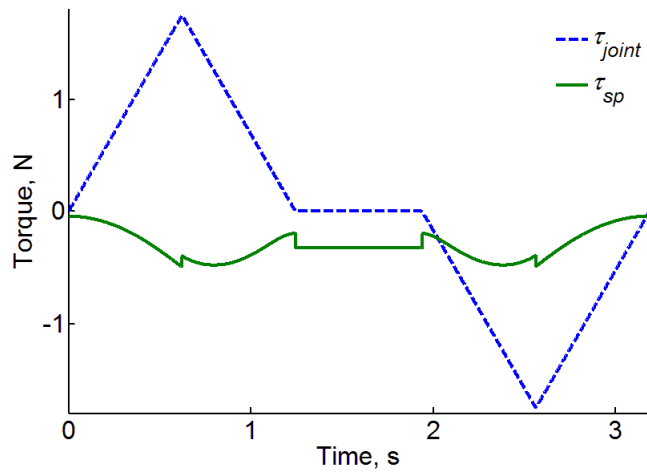


Figure 35. Testbed torques.

Notice that τ_j follows $\ddot{\theta}$, whereas τ_{sp} corresponds to $\dot{\theta}$ and $\ddot{\theta}$ shown in Figure 34.

The CMG testbed is part of ongoing work to better understand CMGs for both traditional attitude control and space robotics. Unlike the analysis herein, the comparisons made between CMGs and joint motors will depend on the control algorithms. The CMG control given in Eq. (53) could be combined with path planning and trajectory control for a free-floating robot. (See [Moosavian and Papadopoulos, 2007] for a recent review.) The hardware implementation also requires an analysis of the measurement uncertainties and the minimum sample rates.

CHAPTER VIII. CONCLUSION

In the limit of an ideal rotor, momentum actuation via CMGs is theoretically as efficient as rigid-body actuation via joint motors, i.e. there is no hidden cost to using momentum actuation comparable to thermodynamics' second law for dynamics. Friction losses and electromagnetic inefficiencies represent additional power costs in physical CMGs. A CMG-driven robot reduces the attitude control effort required to respond to robot motions by distributing the attitude control among the robot joints and helps simplify the dynamic interactions between the spacecraft and robot. Although the complexity of CMGs may not warrant replacing joint motors purely for power savings, additional benefits of eliminating a reaction torque on a spacecraft cannot be ignored. Furthermore, CMGs represent a more power-efficient option for reactionless actuation than reaction wheels.

Scissored-pairs are the preferred CMG array architecture for CMG-driven robots. Geared scissored pairs in particular eliminate potential power losses due to transverse rates of the base spacecraft and consolidate actuation to a single motor. Independent scissored pairs do have two gimbal motors and can operate as two fully independent CMGs for an additional degree of freedom.

Throughout this paper, a number of design principles and pros and cons of CMG-driven robots have been discussed. Results that relate to the design of a CMG robot are summarized in Table 11. The torque amplification and gimbal-torque-limited CMG sizing were obtained through a general treatment of the CMG size, allowing for the possibility of rapid robot-arm movement beyond motions typical of single-body spacecraft because a link in a robot arm may have a much smaller inertia relative to the CMG inertia than for an entire spacecraft.

A summary of the pros and cons of a CMG robot as discussed in this dissertation and related references is provided in Table 12. Table 12 also discusses the utility of combining CMGs and joint motors. Strategically placed CMGs on the robot could reduce reaction forces on the spacecraft by reducing the joint torques. Joint motors in

Table 11. Summary of design tools.

Description	Equation	Reference
Calculate CMG dynamics from equivalent joint-motor robot	$T = -B(\Theta, \dot{\Theta}, \Phi) - D(\Theta, \Phi)\dot{\Phi}$	Eq. (118)
Conservation of angular momentum about joint axis	$\left[\boldsymbol{\omega}^{B/N} \times (I_b \cdot \boldsymbol{\omega}^{B/N}) \right] \cdot \hat{\mathbf{t}} = 0$	Eq. (76)
Gimbal rate bound	$ \dot{\phi} < \ddot{\theta}_{max} \tan(\phi_{max}) / \dot{\theta}_{max}$	Eq. (79)
Torque amplification	$\frac{\tau_{cmg}}{\tau_{sp}} = \frac{I_{b,i} \ddot{\theta}}{2\dot{\theta} h_r \cos \phi}$	Eq. (83)
Gimbal-torque-limited design	$h_r = \sqrt{I_{b,i} \tau_{sp} / 2} \quad \text{and}$ $\dot{\theta}_{max} = \sqrt{2\tau_{sp} / I_{b,i}} \sin \phi_{max}$	Eqs. (86) and (87)
Gimbal acceleration and robot jerk	$\ddot{\phi} = \frac{-I_{b,i} \ddot{\theta} + 2h_r \dot{\phi}^2 \sin \phi}{2h_r \cos \phi}$	Eq. (88)
Relative power costs of CMGs to joint motors	$\tilde{P}_{rel} \Big _{\phi=\phi_{max}} = \frac{I_{cmg} I_{b,i} \ddot{\theta}_{max}}{2\dot{\theta}_{max} h_r^2 \cos^2 \phi_{max}}$	Eq. (92)

turn would provide a path to exchange momentum between robot links and the spacecraft to restore the CMGs to a neutral position, relaxing the requirement that angular momentum be conserved about each joint axis. Also, joint motors provide a means to produce or resist persistent torques that would otherwise saturate the CMGs. An operations concept for a combined actuation method is to use the CMGs for positioning the robot and payload into an anchored position on the spacecraft, and let the joint motors provide the torque for any operations once the payload is anchored.

A smaller, more agile robot may need to devote a significant fraction of its mass and inertia to the CMGs. In such robots, gimbal inertia and rotor momentum must be carefully selected to limit the maximum power requirements. Gimbal motor selection

Table 12. Pros and cons of CMG-driven robotic joints.

Pros	Cons
Reduce reaction forces on spacecraft	Adds mechanical complexity
Simplify spacecraft attitude and robot control interactions	Sensitive to conservation of angular momentum about each joint axis (but robust to transverse rates otherwise)
Use existing dynamics and control methods from robotics with a nested loop for the CMGs	Spin-up and quiescent power costs
Theoretical power performance near that of joint motors, better for reaching motions	Vibration from spinning rotors
CMG dynamics limit jerk of robot	Unable to provide persistent torques

is aided by the bound on the gimbal rate and estimated gimbal torque. For sizing the motor on a single CMG used in an arbitrary array, the scissored-pair gimbal angle ϕ corresponds to the angle between the rotor momentum and the array's output-torque axis. The rate bound applies, and the gimbal torque is approximated by half the scissored-pair torque. The difficulty in extending these results to an arbitrary CMG array is that the maximum gimbal angle is not well defined because the array's output-torque axis is continually changing and the gimbals are typically free to rotate continuously. However, control based on limiting an analogous maximum gimbal angle so that CMGs are not asked to provide actuation when the angle between the rotor momentum and the desired output torque axis exceeds a specified value may also improve robustness to singularities.

Simulations that include transverse rotations of the spacecraft base indicate that relative power use is not affected by gyroscopic torques as a consequence of the scissored-pair architecture used. A robot that does not conserve momentum about the joint axes introduces additional complexity in the design of CMG-actuated robots because the gimbals do not necessarily return to their original position in a rest-to-rest maneuver. Such concerns arise for robotic manipulation because the inertial properties of a payload are uncertain. CMGs redirect the momentum of the robot without torquing against an inertial base. However, robotic manipulators are often called on to provide torques against a payload and would saturate a purely gyroscopic actuator. A possible solution to avoid saturating the CMGs is to combine CMG actuation with joint motors where the required torques are distributed among the CMGs and joint motors according to some design criteria.

Recursive equations of motion for a general n -link robot facilitate simulation of robots with increasing numbers of links. A two-link robot with orthogonal axes can often be written as two independent, single-link robots. If the equations of motion

cannot be decoupled for such a joint topology, angular momentum is not conserved about the joint axes, and the CMGs may have trouble avoiding saturation.

For a planar two-link robot, CMGs provides an advantage in power use for maneuvers with opposite joint motions, such as reaching motions. Replacing CMGs with body torques explains their advantage over joint torques for these motions, as well as the corresponding advantage of joint torques for other maneuvers.

Considering a general robotics system with either joint torques or body torques provides context for the CMG robot. For robots with a mix of actuation methods, the link closest to the spacecraft may operate with a body torque (e.g. CMGs) without sacrificing optimal power usage. An overactuated, three-link planar robot tracing a closed triangular path uses less energy than either joint-torque or body-torque-only configurations.

An illustrative case study sizing CMGs for a testbed currently in development demonstrates the importance of gimbal torque on CMG sizing. Future work with the testbed will implement control algorithms designed for CMGs as well as demonstrate the value of CMGs on robotic appendages of free-floating spacecraft.

A further recommendation for continued work is to generalize the CMG design rules laid out in this work to apply to arbitrary arrays of CMGs on spacecraft. Scissored pairs will likely be ready replacements for reaction wheels with significant gains in torque available and reductions in the power requirements of the attitude control system. Additional, though smaller, gains from other CMG arrays would then have a baseline gained through much greater flight heritage than now exists.

APPENDIX A.

List of Equations

$$\Delta E_r = \frac{1}{2} I_r (\omega_2^2 - \omega_1^2) \quad (1) \dots\dots 16$$

$$\begin{aligned} \mathbf{H}_{cmg} &= \mathbf{I}_g \cdot \boldsymbol{\omega}^{G/N} + \mathbf{I}_r \cdot \boldsymbol{\omega}^{R/N} \\ &= \mathbf{I}_g \cdot (\boldsymbol{\omega}^{G/B} + \boldsymbol{\omega}^{B/N}) + \mathbf{I}_r \cdot (\boldsymbol{\omega}^{R/G} + \boldsymbol{\omega}^{G/B} + \boldsymbol{\omega}^{B/N}) \\ &= \mathbf{I}_{cmg} \cdot (\boldsymbol{\omega}^{G/B} + \boldsymbol{\omega}^{B/N}) + \mathbf{h}_r \end{aligned} \quad (2) \dots\dots 19$$

$$\boldsymbol{\tau}_{cmg} = -\mathbf{H}_{cmg}^N \quad (3) \dots\dots 19$$

$$\mathbf{x} = \frac{Y}{dt} d(\mathbf{x}) \quad (4) \dots\dots 19$$

$$\mathbf{H}_{cmg}^N = I_{cmg} \cdot \left(\ddot{\phi} \hat{\mathbf{g}} + \boldsymbol{\omega}^{B/N} - \dot{\phi} \hat{\mathbf{g}} \times \boldsymbol{\omega}^{B/N} \right) + (\dot{\phi} \hat{\mathbf{g}} + \boldsymbol{\omega}^{B/N}) \times \left[I_{cmg} \cdot (\dot{\phi} \hat{\mathbf{g}} + \boldsymbol{\omega}^{B/N}) + \mathbf{h}_r \right] \quad (5) \dots\dots 19$$

$$\mathbf{I}_g + \mathbf{I}_r = \mathbf{I}_{cmg} = I_{cmg} \mathbf{I} \quad (6) \dots\dots 20$$

$$I_{cmg} = I_{cmg} \cdot \hat{\mathbf{g}} + (h_r^2 / k_{OA}) \quad (7) \dots\dots 20$$

$$\boldsymbol{\tau}_{cmg} = -\dot{\phi} \hat{\mathbf{g}} \times \mathbf{h}_r \quad (8) \dots\dots 21$$

$$\tau_{g,i} = (-1)^{i-1} \cdot I_{cmg} \ddot{\phi} + I_{cmg} \boldsymbol{\omega}^{B/N} \cdot \hat{\mathbf{g}} + (\boldsymbol{\omega}^{B/N} \times \mathbf{h}_{r,i}) \cdot \hat{\mathbf{g}} \quad (9) \dots\dots 25$$

$$\tau_{sp} = \tau_{g1} - \tau_{g2} \quad (10) \dots\dots 26$$

$$\tau_{sp} = 2I_{cmg} \ddot{\phi} + \left[\boldsymbol{\omega}^{B/N} \times (\mathbf{h}_{r1} - \mathbf{h}_{r2}) \right] \cdot \hat{\mathbf{g}} \quad (11) \dots\dots 26$$

$$\tau_{sp} = 2I_{cmg} \ddot{\phi} - \boldsymbol{\omega}^{B/N} \cdot 2h_r \cos \phi \hat{\mathbf{t}} \quad (12) \dots\dots 27$$

$$P_{sp} = \left| \tau_{sp} \dot{\phi} \right| \quad (13) \dots\dots 27$$

$$P_{ind} = \left| \tau_{g1} \dot{\phi} \right| + \left| \tau_{g2} \dot{\phi} \right| \quad (14) \dots\dots 28$$

$$I_{cmg} \ddot{\phi} \ll \omega^{B/N} \cdot h_r \cos \phi \hat{\mathbf{t}} \quad (15) \dots\dots 28$$

$$\tau_{sp} \approx -\omega^{B/N} \cdot 2h_r \cos \phi \hat{\mathbf{t}} \quad (16) \dots\dots 28$$

$$P_{sp} \approx \left| \dot{\phi} \cdot \left[\omega^{B/N} \times (\mathbf{h}_{r1} - \mathbf{h}_{r2}) \right] \cdot \hat{\mathbf{g}} \right| \quad (17) \dots\dots 29$$

$$P_{ind} \approx \left| \dot{\phi} \cdot (\omega^{B/N} \times \mathbf{h}_{r1}) \cdot \hat{\mathbf{g}} \right| + \left| \dot{\phi} \cdot (\omega^{B/N} \times \mathbf{h}_{r2}) \cdot \hat{\mathbf{g}} \right| \quad (18) \dots\dots 29$$

$$P_x^* = \frac{P_x}{\left(\left\| \omega^{B/N} \right\| h_r \right)} \quad (19) \dots\dots 29$$

$$P_{sp}^* \approx |2 \cos \alpha \cos \phi| \quad (20) \dots\dots 29$$

$$P_{ind}^* \approx |\cos(\alpha - \phi)| + |\cos(\alpha + \phi)| \quad (21) \dots\dots 29$$

$$\frac{P_{sp}}{P_{ind}} \approx \frac{|2 \cos \alpha \cos \phi|}{|\cos(\alpha - \phi)| + |\cos(\alpha + \phi)|} \quad (22) \dots\dots 32$$

$$\left(\mathbf{I}_b \cdot \omega^{B/N} \right) \cdot \hat{\mathbf{t}} = -2h_r \sin \phi \quad (23) \dots\dots 34$$

$$\alpha = \cos^{-1} \left(\frac{\omega^{B/N}}{\left\| \omega^{B/N} \right\|} \cdot \hat{\mathbf{t}} \right) \quad (24) \dots\dots 34$$

$$|2h_r| = \left| \mathbf{I}_b \cdot \omega^{B/N} \right| \quad (25) \dots\dots 35$$

$$E_c = \frac{1}{2} \omega^{B/N} \cdot \mathbf{I}_{sc} \cdot \omega^{B/N} + \frac{1}{2} \sum_{i=1}^n \left(\omega^{B/N} + \dot{\phi}_i \hat{\mathbf{g}}_i \right) \cdot \mathbf{I}_{g,i} \cdot \left(\omega^{B/N} + \dot{\phi}_i \hat{\mathbf{g}}_i \right) \\ + \frac{1}{2} \sum_{i=1}^n \left(\omega^{B/N} + \dot{\phi}_i \hat{\mathbf{g}}_i + \Omega_i \hat{\mathbf{h}}_i \right) \cdot \mathbf{I}_{r,i} \cdot \left(\omega^{B/N} + \dot{\phi}_i \hat{\mathbf{g}}_i + \Omega_i \hat{\mathbf{h}}_i \right) \quad (26) \dots\dots 40$$

$$\frac{\partial E_c}{\partial \Omega} = \hat{\mathbf{h}} \cdot \mathbf{I}_r \cdot \left(\omega^{B/N} + \Omega \hat{\mathbf{h}} \right) \quad (27) \dots\dots 41$$

$$P_r = \tau_r \cdot \Omega \quad (28) \dots\dots 41$$

$$\mathbf{H}_r = \mathbf{I}_r \cdot \left(\omega^{B/N} + \dot{\phi} \hat{\mathbf{g}} + \Omega \hat{\mathbf{h}} \right) \quad (29) \dots\dots 41$$

$$\mathbf{H}_r^N = I_r \cdot \left(\boldsymbol{\omega}^{B/N} - \dot{\phi} \hat{\mathbf{g}} \times \boldsymbol{\omega}^{B/N} + \ddot{\phi} \hat{\mathbf{g}} + \dot{\Omega} \hat{\mathbf{h}} \right) + \left(\boldsymbol{\omega}^{B/N} + \dot{\phi} \hat{\mathbf{g}} \right) \times \left[I_r \cdot \left(\boldsymbol{\omega}^{B/N} + \dot{\phi} \hat{\mathbf{g}} + \Omega \hat{\mathbf{h}} \right) \right] \quad (30) \dots 41$$

$$\tau_r = \left\{ I_r \cdot \left(\boldsymbol{\omega}^{B/N} - \dot{\phi} \hat{\mathbf{g}} \times \boldsymbol{\omega}^{B/N} + \dot{\Omega} \hat{\mathbf{h}} \right) + \left(\boldsymbol{\omega}^{B/N} + \dot{\phi} \hat{\mathbf{g}} \right) \times \left[I_r \cdot \left(\boldsymbol{\omega}^{B/N} + \dot{\phi} \hat{\mathbf{g}} \right) \right] \right\} \cdot \hat{\mathbf{h}} \quad (31) \dots 41$$

$$\tau_r = I_r \left(\boldsymbol{\omega}^{B/N} - \dot{\phi} \hat{\mathbf{g}} \times \boldsymbol{\omega}^{B/N} \right) \cdot \hat{\mathbf{h}} + I_r \dot{\Omega} \quad (32) \dots 41$$

$$P_r = \Omega \cdot I_r \left(\boldsymbol{\omega}^{B/N} - \dot{\phi} \hat{\mathbf{g}} \times \boldsymbol{\omega}^{B/N} \right) \cdot \hat{\mathbf{h}} \quad (33) \dots 41$$

$$P_r \approx \left| \left(\dot{\phi} \hat{\mathbf{g}} \times \boldsymbol{\omega}^{B/N} \right) \cdot \mathbf{h}_r \right| \quad (34) \dots 42$$

$$\frac{\partial \tau_g}{\partial \Omega} = \left(\boldsymbol{\omega}^{B/N} \times I_r \hat{\mathbf{h}} \right) \cdot \hat{\mathbf{g}} \quad (35) \dots 42$$

$$\frac{\partial \tau_{cmg}}{\partial \Omega} = I_r \hat{\mathbf{h}} + \left(\boldsymbol{\omega}^{B/N} + \dot{\phi} \hat{\mathbf{g}} \right) \times I_r \hat{\mathbf{h}} \quad (36) \dots 43$$

$$I_r \dot{\theta} \sin \phi + I_r \Omega = I_r \Omega_0 \quad (37) \dots 43$$

$$\Omega - \Omega_0 = \Omega_{err} = -\dot{\theta} \sin \phi \quad (38) \dots 43$$

$$I_c \dot{\theta} + I_r \Omega \sin \phi = 0 \quad (39) \dots 44$$

$$I_c \dot{\theta}_{err} + I_r \Omega_{err} \sin \phi = 0 \quad (40) \dots 44$$

$$\dot{\theta}_{err} = I_r \dot{\theta} \sin^2 \phi / I_c \quad (41) \dots 44$$

$$\tau_{r,i} = I_r \left(\boldsymbol{\omega}^{B/N} - \dot{\phi}_i \hat{\mathbf{g}}_i \times \boldsymbol{\omega}^{B/N} \right) \cdot \hat{\mathbf{h}}_i + I_r \dot{\Omega}_i \quad (42) \dots 46$$

$$\mathbf{H}_c = I_{sc} \cdot \boldsymbol{\omega}^{B/N} + \sum_{i=1}^C \left[I_{g,i} \cdot \left(\boldsymbol{\omega}^{B/N} + \dot{\phi}_i \hat{\mathbf{g}}_i \right) + I_{r,i} \cdot \left(\boldsymbol{\omega}^{B/N} + \dot{\phi}_i \hat{\mathbf{g}}_i + \Omega_i \hat{\mathbf{h}}_i \right) \right] \quad (43) \dots 46$$

$$\mathbf{H}_c = I_c \cdot \boldsymbol{\omega}^{B/N} + \sum_{i=1}^C \left[I_{cmg,i} \dot{\phi}_i \hat{\mathbf{g}}_i + I_r \Omega_i \hat{\mathbf{h}}_i \right] \quad (44) \dots 46$$

$$\begin{aligned} \hat{\mathbf{H}}_c^N &= I_c \cdot \boldsymbol{\omega}^{B/N} + \boldsymbol{\omega}^{B/N} \times I_c \cdot \boldsymbol{\omega}^{B/N} + \sum_{i=1}^C (I_{cmg} \ddot{\phi}_i \hat{\mathbf{g}}_i + \boldsymbol{\omega}^{B/N} \times I_{cmg} \dot{\phi}_i \hat{\mathbf{g}}_i) \\ &+ \sum_{i=1}^C [I_r \dot{\Omega}_i \hat{\mathbf{h}}_i + (\boldsymbol{\omega}^{B/N} + \dot{\phi}_i \hat{\mathbf{g}}_i) \times I_r \Omega_i \hat{\mathbf{h}}_i] \end{aligned} \quad (45) \dots\dots 47$$

$$\begin{aligned} &\begin{bmatrix} \hat{\mathbf{b}}_k \cdot I_c \cdot \hat{\mathbf{b}}_k & I_{cmg} \hat{\mathbf{g}}_i \cdot \hat{\mathbf{b}}_k & 0 & I_r \hat{\mathbf{h}}_i \cdot \hat{\mathbf{b}}_k \\ I_{cmg} \hat{\mathbf{b}}_k \cdot \hat{\mathbf{g}}_i & I_{cmg} & 0 & 0 \\ 0 & 0 & 1 & 0 \\ I_r & 0 & 0 & I_r \end{bmatrix} \cdot \begin{bmatrix} \dot{u}_k \\ \ddot{\phi}_i \\ \dot{\phi}_i \\ -\dot{\Omega}_i \end{bmatrix} \\ &= \begin{bmatrix} -[\boldsymbol{\omega}^{B/N} \times (I_c \cdot \boldsymbol{\omega}^{B/N} + I_{cmg} \dot{\phi}_i \hat{\mathbf{g}}_i + I_r \Omega_i \hat{\mathbf{h}}_i) + \dot{\phi}_i \hat{\mathbf{g}}_i \times I_r \Omega_i \hat{\mathbf{h}}_i] \cdot \hat{\mathbf{b}}_k \\ -(\boldsymbol{\omega}^{B/N} \times I_r \Omega_i \hat{\mathbf{h}}_i) \cdot \hat{\mathbf{g}}_i \\ \dot{\phi}_i \\ I_r (\dot{\phi}_i \hat{\mathbf{g}}_i \times \boldsymbol{\omega}^{B/N}) \cdot \hat{\mathbf{h}}_i \end{bmatrix} + \begin{bmatrix} \boldsymbol{\tau}_{ext} \cdot \hat{\mathbf{b}}_k \\ \tau_{g,i} \\ 0 \\ \tau_{r,i} \end{bmatrix} \end{aligned} \quad (46) \dots\dots 47$$

$$\mathbf{M} = \begin{bmatrix} \text{diag } 3 \times 3 & 3 \times C & 3 \times C & 3 \times C \\ C \times 3 & & & \\ C \times 3 & \text{diag } 3C \times 3C & & \\ C \times 3 & & & \end{bmatrix} \quad (47) \dots\dots 47$$

$$\dot{\theta} = -2I_r \Omega \sin \phi / I_c \quad (48) \dots\dots 48$$

$$\dot{\theta} = -2I_{r,\hat{\mathbf{h}}} \Omega K (\theta - \theta_{des}) / I_b \quad (49) \dots\dots 48$$

$$\ddot{\theta} = -2I_r \Omega \dot{\phi} \cos \phi / I_c \quad (50) \dots\dots 49$$

$$\begin{bmatrix} \dot{\theta} \\ \ddot{\theta} \end{bmatrix} = \begin{bmatrix} 0 & 1 \\ 0 & 0 \end{bmatrix} \cdot \begin{bmatrix} \theta \\ \dot{\theta} \end{bmatrix} + \begin{bmatrix} 0 \\ -2I_r \Omega / I_c \end{bmatrix} \dot{\phi} \quad (51) \dots\dots 49$$

$$C = \begin{bmatrix} 0 & -2I_r \Omega / I_b \\ -2I_r \Omega / I_b & 0 \end{bmatrix} \quad (52) \dots\dots 49$$

$$\begin{bmatrix} \ddot{\theta} \\ \ddot{\phi} \\ \dot{\phi} \\ \dot{\theta} \end{bmatrix} = \begin{bmatrix} 0 & -2I_r \Omega \cos \phi / I_c & 0 & 0 \\ I_r \Omega \cos \phi / I_{cmg} & 0 & 0 & 0 \\ 0 & 1 & 0 & 0 \\ 1 & 0 & 0 & 0 \end{bmatrix} \cdot \begin{bmatrix} \dot{\theta} \\ \dot{\phi} \\ \phi \\ \theta \end{bmatrix} + \begin{bmatrix} 0 \\ 1/2I_{cmg} \\ 0 \\ 0 \end{bmatrix} \cdot \boldsymbol{\tau}_{sp} \quad (53) \dots\dots 49$$

$$C = \begin{bmatrix} 0 & -I_r \Omega / (I_c I_{cmg}) & 0 & 0 \\ 1/2 I_{cmg} & 0 & -2(I_r \Omega)^2 / (I_c I_{cmg}) & -2(I_r \Omega)^3 / (I_c I_{cmg})^2 \\ 0 & 1/2 I_{cmg} & 0 & 0 \\ 0 & 0 & -2I_r \Omega / I_c & 0 \end{bmatrix} \quad (54) \dots\dots 50$$

$$0 = I_r (\ddot{\theta} \sin \phi - \dot{\theta} \dot{\phi} I_r \Omega_i \cos \phi) + I_r \dot{\Omega}_i \quad (55) \dots\dots 51$$

$$\begin{bmatrix} I_c & 2I_r \sin \phi & 0 & 0 & 0 \\ I_r & I_r & 0 & 0 & 0 \\ 0 & 0 & 2I_{cmg} & 0 & 0 \\ 0 & 0 & 0 & 1 & 0 \\ 0 & 0 & 0 & 0 & I_c \end{bmatrix} \cdot \begin{bmatrix} \ddot{\theta} \\ \dot{\Omega} \\ \ddot{\phi} \\ \dot{\phi} \\ \dot{\theta} \end{bmatrix} = \begin{bmatrix} -2\dot{\phi} I_r \Omega \cos \phi \\ -I_r \dot{\phi} \dot{\theta} \cos \phi \\ 2\dot{\theta} I_r \Omega \cos \phi \\ \dot{\phi} \\ -2I_r \Omega \sin \phi \end{bmatrix} + \begin{bmatrix} 0 & 0 \\ 0 & 1 \\ 1 & 0 \\ 0 & 0 \\ 0 & 0 \end{bmatrix} \cdot \begin{bmatrix} \tau_{sp} \\ \tau_r \end{bmatrix} \quad (56) \dots\dots 51$$

$$\begin{bmatrix} I_c & 2I_r \sin \phi \\ I_r & I_r \end{bmatrix}^{-1} = \frac{1}{\det} \begin{bmatrix} I_r & -2I_r \sin \phi \\ -I_r & I_c \end{bmatrix} \quad (57) \dots\dots 51$$

$$\det = I_r (I_c - 2I_r \sin \phi)$$

$$\begin{bmatrix} \ddot{\theta} \\ \dot{\Omega} \\ \ddot{\phi} \\ \dot{\phi} \\ \dot{\theta} \end{bmatrix} = \begin{bmatrix} (\sin \phi \dot{\theta} - \Omega) 2I_r \dot{\phi} \cos \phi / \Delta \\ (2I_r \Omega - I_c \dot{\theta}) \dot{\phi} \cos \phi / \Delta \\ \dot{\theta} I_r \Omega \cos \phi / I_{cmg} \\ \dot{\phi} \\ -2I_r \Omega \sin \phi \end{bmatrix} + \begin{bmatrix} 0 & -2I_r \sin \phi / den \\ 0 & I_c / den \\ 0 & 0 \\ 0 & 0 \\ 0 & 0 \end{bmatrix} \cdot \begin{bmatrix} \tau_{sp} \\ \tau_r \end{bmatrix} \quad (58) \dots\dots 51$$

$$\tau_r = I_r [-K_r (\Omega - \Omega_0) + \tau_{drag}] \quad (59) \dots\dots 52$$

$$\begin{bmatrix} \ddot{\theta} \\ \dot{\Omega} \\ \ddot{\phi} \\ \dot{\phi} \\ \dot{\theta} \end{bmatrix} = \begin{bmatrix} 0 & 0 & -2\Omega_0 I_r / I_c & 0 & 0 \\ 0 & -K_r & 2\Omega_0 I_r / I_c & 0 & 0 \\ I_r \Omega_0 / I_{cmg} & 0 & 0 & 0 & 0 \\ 0 & 0 & 1 & 0 & 0 \\ 0 & 0 & 0 & -2I_r \Omega_0 & 0 \end{bmatrix} \cdot \begin{bmatrix} \dot{\theta} \\ \Omega_{err} \\ \dot{\phi} \\ \phi \\ \theta \end{bmatrix} + \begin{bmatrix} 0 \\ 0 \\ 1/(2I_{cmg}) \\ 0 \\ 0 \end{bmatrix} \cdot \tau_{sp} \quad (60) \dots\dots 52$$

$$\mathbf{H}_b = \mathbf{H}_j = \mathbf{I}_b \cdot \boldsymbol{\omega}^{B/N} \quad (61) \dots\dots 54$$

$$\dot{\mathbf{H}}_b^N = \mathbf{I}_b \cdot \dot{\boldsymbol{\omega}}^{B/N} + \boldsymbol{\omega}^{B/N} \times (\mathbf{I}_b \cdot \boldsymbol{\omega}^{B/N}) \quad (62) \dots\dots 54$$

$$\tau_j = I_b \cdot \boldsymbol{\omega}^{B/N} \cdot \hat{\mathbf{t}} + \left[\boldsymbol{\omega}^{B/N} \times (I_b \cdot \boldsymbol{\omega}^{B/N}) \right] \cdot \hat{\mathbf{t}} \quad (63) \dots\dots 55$$

$$\mathbf{H}_c = \mathbf{H}_b + \mathbf{h}_{cmg1} + \mathbf{h}_{cmg2} \quad (64) \dots\dots 55$$

$$\mathbf{H}_c = I_b \cdot \boldsymbol{\omega}^{B/N} + I_{cmg} \cdot (\boldsymbol{\omega}^{G1/B} + \boldsymbol{\omega}^{B/N}) + \mathbf{h}_{r1} + I_{cmg} \cdot (\boldsymbol{\omega}^{G2/B} + \boldsymbol{\omega}^{B/N}) + \mathbf{h}_{r2}$$

$$\mathbf{h}_{r1} + \mathbf{h}_{r2} = 2h_r \sin \phi \hat{\mathbf{t}} \quad (65) \dots\dots 55$$

$$\mathbf{H}_c = I_b \cdot \boldsymbol{\omega}^{B/N} + 2h_r \sin \phi \hat{\mathbf{t}} \quad (66) \dots\dots 55$$

$$\dot{\mathbf{H}}_c^N = I_b \cdot \dot{\boldsymbol{\omega}}^{B/N} + \boldsymbol{\omega}^{B/N} \times (I_b \cdot \boldsymbol{\omega}^{B/N}) + 2h_r \dot{\phi} \cos \phi \hat{\mathbf{t}} + \boldsymbol{\omega}^{B/N} \times 2h_r \sin \phi \hat{\mathbf{t}} \quad (67) \dots\dots 55$$

$$0 = I_b \cdot \dot{\boldsymbol{\omega}}^{B/N} \cdot \hat{\mathbf{t}} + (\boldsymbol{\omega}^{B/N} \times (I_b \cdot \boldsymbol{\omega}^{B/N})) \cdot \hat{\mathbf{t}} + 2h_r \dot{\phi} \cos \phi \quad (68) \dots\dots 56$$

$$\dot{\phi} = \frac{-\tau_j}{2h_r \cos \phi} \quad (69) \dots\dots 56$$

$$\boldsymbol{\omega}^{B/N} \cdot \hat{\mathbf{t}} = \dot{\theta} \quad (70) \dots\dots 56$$

$$P_j = |\tau_j \dot{\theta}| \quad (71) \dots\dots 56$$

$$P_{cmg} = \left| \left(2I_{cmg} \ddot{\phi} - 2\dot{\theta} h_r \cos \phi \right) \frac{-\tau_j}{2h_r \cos \phi} \right| \quad (72) \dots\dots 56$$

$$P_{cmg} \approx |\tau_j \dot{\theta}| \quad (73) \dots\dots 56$$

$$\frac{d}{dt} (\mathbf{H}_c \cdot \hat{\mathbf{t}}) = \frac{d}{dt} (\mathbf{H}_c) \cdot \hat{\mathbf{t}} + \mathbf{H}_c \cdot \frac{d}{dt} (\hat{\mathbf{t}}) \quad (74) \dots\dots 57$$

$$\frac{d}{dt} (\mathbf{H}_c \cdot \hat{\mathbf{t}}) = (I_b \cdot \boldsymbol{\omega}^{B/N} + 2h_r \sin \phi \hat{\mathbf{t}}) \cdot (\boldsymbol{\omega}^{B/N} \times \hat{\mathbf{t}}) \quad (75) \dots\dots 58$$

$$\left[\boldsymbol{\omega}^{B/N} \times (I_b \cdot \boldsymbol{\omega}^{B/N}) \right] \cdot \hat{\mathbf{t}} = 0 \quad (76) \dots\dots 58$$

$$\mathbf{H}_c \cdot \hat{\mathbf{t}} = I_{b,i} \dot{\theta} + 2h_r \sin \phi = 0 \quad (77) \dots\dots 58$$

$$\tau_j = I_{b,i} \ddot{\theta} \quad (78) \dots\dots 59$$

$$|\dot{\phi}| < \ddot{\theta}_{max} \tan(\phi_{max}) / \dot{\theta}_{max} \quad (79) \dots\dots 59$$

$$\tau_{cmg} / \tau_g \gg 1 \quad (80) \dots\dots 59$$

$$\dot{\phi} / \dot{\theta} \gg 1 \quad (81) \dots\dots 59$$

$$\frac{\tau_{cmg}}{\tau_g} = \frac{I_{b,i} \ddot{\theta}}{2I_{cmg} \dot{\phi} - 2\dot{\theta} h_r \cos \phi} \quad (82) \dots\dots 60$$

$$\frac{\tau_{cmg}}{\tau_{sp}} = \frac{I_{b,i} \ddot{\theta}}{2\dot{\theta} h_r \cos \phi} \quad (83) \dots\dots 60$$

$$\tau_{sp} = (2h_r)^2 \sin \phi \cos \phi / I_{b,i} \quad (84) \dots\dots 61$$

$$\frac{\partial \tau_{sp}}{\partial \phi} = 0 = (2h_r)^2 (\cos^2 \phi - \sin^2 \phi) / I_{b,i} \quad (85) \dots\dots 61$$

$$h_r = \sqrt{I_{b,i} \tau_{sp} / 2} \quad (86) \dots\dots 61$$

$$\dot{\theta}_{max} = \sqrt{2\tau_{sp} / I_{b,i}} \sin \phi_{max} \quad (87) \dots\dots 61$$

$$\ddot{\phi} = \frac{-I_{b,i} \ddot{\theta} + 2h_r \dot{\phi}^2 \sin \phi}{2h_r \cos \phi} \quad (88) \dots\dots 62$$

$$\tilde{P}_{rel} = \frac{P_{cmg} - P_j}{P_j} \quad (89) \dots\dots 63$$

$$\tilde{P}_{rel} = \frac{-I_{cmg} \ddot{\phi}}{\dot{\theta} h_r \cos \phi} \quad (90) \dots\dots 63$$

$$\tilde{P}_{rel} = \frac{I_{cmg} I_{b,i}}{2\dot{\theta} h_r^2 \cos^2 \phi} \left(\ddot{\theta} - \frac{I_{b,i} \ddot{\theta}^2 \sin \phi}{2h_r \cos^2 \phi} \right) \quad (91) \dots\dots 63$$

$$\tilde{P}_{rel} \Big|_{\phi=\phi_{max}} = \frac{I_{cmg} I_{b,i} \ddot{\theta}_{max}}{2\dot{\theta}_{max} h_r^2 \cos^2 \phi_{max}} \quad (92) \dots\dots 64$$

$$\tilde{P}_{rel} \Big|_{\phi=\phi_{max}} = \frac{2I_{cmg} I_{b,\hat{t}} \ddot{\theta}_{max}}{h_r^2 - (I_{b,\hat{t}} \dot{\theta}_{max})^2} \quad (93) \dots\dots 65$$

$$\ddot{\theta}_{max}^2 = \ddot{\theta}_{max} \cdot \dot{\theta}_{max} \quad (94) \dots\dots 66$$

$$\Delta\theta = \dot{\theta}_{max} \left(\frac{\dot{\theta}_{max}}{\ddot{\theta}_{max}} + \frac{\ddot{\theta}_{max}}{\ddot{\theta}_{max}} \right) \quad (95) \dots\dots 66$$

$$\Delta t = 4\ddot{\theta}_{max} / \ddot{\theta}_{max} \quad (96) \dots\dots 66$$

$$E_j = \int_0^{\Delta t} |\tau_j \dot{\phi}| dt \quad (97) \dots\dots 67$$

$$E_{cmg} = \int_0^{\Delta t} |\tau_{sp} \dot{\phi}| dt \quad (98) \dots\dots 67$$

$$\mathbf{H}_c \Big|_{\dot{\theta}=\dot{\theta}_{max}} \approx \mathbf{H}_c \Big|_{t=0} + \left[\frac{d\mathbf{H}_c}{dt} \cdot t \right]_{max} \quad (99) \dots\dots 70$$

$$\mathbf{I}_b \cdot \boldsymbol{\omega}_{max}^{Bi/N} \cdot \hat{\mathbf{t}} + 2h_r \sin \phi_{max} \approx 0 - \left[\boldsymbol{\omega}^{Bi/N} \times (\mathbf{I}_b \cdot \boldsymbol{\omega}^{Bi/N}) \cdot \hat{\mathbf{t}} \right]_{max} \cdot \Delta t / 2 \quad (100) \dots\dots 71$$

$$\sum_{i=1}^n \left(m_i \mathbf{v}_i^N - \mathbf{F}_i^a \right) \cdot \frac{\partial \mathbf{v}_i}{\partial \dot{q}_k} + \sum_{i=1}^n \left(\mathbf{H}_i^N - \mathbf{M}_i^a \right) \cdot \frac{\partial \boldsymbol{\omega}^{Bi/N}}{\partial \dot{q}_k} = 0 \text{ for } k = 1..n \quad (101) \dots\dots 75$$

$$\boldsymbol{\omega}^{Bi/N} = \dot{q}_i \hat{\mathbf{t}}_i + \boldsymbol{\omega}^{Bi-1/N} \quad (102) \dots\dots 76$$

$$\boldsymbol{\omega}^{Bi/N} = \ddot{q}_i \hat{\mathbf{t}}_i - \dot{q}_i \hat{\mathbf{t}}_i \times \boldsymbol{\omega}^{Bi-1/N} + \boldsymbol{\omega}^{Bi-1/N} \quad (103) \dots\dots 76$$

$$\frac{\partial \boldsymbol{\omega}^{Bi/N}}{\partial \dot{q}_k} = \begin{cases} \hat{\mathbf{t}}_k & k \leq i \\ 0 & k > i \end{cases} \quad (104) \dots\dots 77$$

$$\mathbf{H}_{j,i}^N = \mathbf{I}_i \boldsymbol{\omega}^{Bi/N} + \boldsymbol{\omega}^{Bi/N} \times \mathbf{I}_i \boldsymbol{\omega}^{Bi/N} \quad (105) \dots\dots 77$$

$$\mathbf{M}_{j,i}^a = \tau_{j,i} \hat{\mathbf{t}}_i - \tau_{j,i+1} \hat{\mathbf{t}}_{i+1} \quad (106) \dots\dots 77$$

$$\sum_{i=1}^N \mathbf{M}_{j,i}^a \cdot \frac{\partial \boldsymbol{\omega}^{Bi/N}}{\partial \dot{q}_k} = \sum_{i=k}^N \left\{ (\tau_{j,i} \hat{\mathbf{t}}_i - \tau_{j,i+1} \hat{\mathbf{t}}_{i+1}) \cdot \hat{\mathbf{t}}_k \right\} \quad (107) \dots\dots 77$$

$$\sum_{i=1}^N \mathbf{M}_{j,i}^a \cdot \frac{\partial \boldsymbol{\omega}^{\text{Bi}/N}}{\partial \dot{q}_k} = \tau_{j,k} \quad (108) \dots 77$$

$$\mathbf{R}_i = \sum_{m=1}^{i-1} \mathbf{l}_m + \mathbf{r}_i \quad (109) \dots 78$$

$$\mathbf{v}_i = \mathbf{R}_i = \sum_{m=1}^N \boldsymbol{\omega}^{\text{Bj}/N} \times \mathbf{l}_m + \boldsymbol{\omega}^{\text{Bi}/N} \times \mathbf{r}_i \quad (110) \dots 78$$

$$\mathbf{v}_i = \sum_{m=1}^N \left\{ \boldsymbol{\omega}^{\text{Bm}/N} \times \mathbf{l}_m + \boldsymbol{\omega}^{\text{Bm}/N} \times (\boldsymbol{\omega}^{\text{Bm}/N} \times \mathbf{l}_j) \right\} + \boldsymbol{\omega}^{\text{Bi}/N} \times \mathbf{r}_i + \boldsymbol{\omega}^{\text{Bi}/N} \times (\boldsymbol{\omega}^{\text{Bi}/N} \times \mathbf{r}_i) \quad (111) \dots 78$$

$$\frac{\partial \mathbf{v}_i}{\partial \dot{q}_k} = \begin{cases} \hat{\mathbf{t}}_k \times \left(\mathbf{r}_i + \sum_{\substack{m=k \\ k \neq i}}^{i-1} \mathbf{l}_m \right) & i \geq k \\ 0 & i < k \end{cases} \quad (112) \dots 78$$

$$\sum_{i=1}^N \mathbf{M}_i^a \cdot \frac{\partial \boldsymbol{\omega}^{\text{Bi}/N}}{\partial \dot{q}_k} = 0 \quad (113) \dots 78$$

$$\mathbf{H}_{c,i}^N = \mathbf{I}_i \cdot \boldsymbol{\omega}^{\text{Bi}/N} + \boldsymbol{\omega}^{\text{Bi}/N} \times (\mathbf{I}_i \cdot \boldsymbol{\omega}^{\text{Bi}/N}) + 2h_{r,i} \dot{\phi}_i \cos \phi_i \hat{\mathbf{t}}_i + \boldsymbol{\omega}^{\text{Bi}/N} \times 2h_{r,i} \sin \phi_i \hat{\mathbf{t}}_i \quad (114) \dots 79$$

$$\sum_{i=1}^n \mathbf{H}_{c,i}^N \cdot \frac{\partial \boldsymbol{\omega}^{\text{Bi}/N}}{\partial \dot{q}_k} = \sum_{i=1}^n \mathbf{H}_{j,i}^N \cdot \frac{\partial \boldsymbol{\omega}^{\text{Bi}/N}}{\partial \dot{q}_k} + 2h_r \dot{\phi}_i \cos \phi_i \hat{\mathbf{t}}_i \cdot \hat{\mathbf{t}}_k + \boldsymbol{\omega}^{\text{Bi}/N} \cdot (2h_r \sin \phi_i \hat{\mathbf{t}}_i \times \hat{\mathbf{t}}_k) \quad (115) \dots 79$$

$$M(\Theta, \dot{\Theta}) \ddot{\Theta} + V(\Theta, \dot{\Theta}) = T \quad (116) \dots 79$$

$$M(\Theta, \dot{\Theta}) \ddot{\Theta} + V(\Theta, \dot{\Theta}) = -B(\Theta, \dot{\Theta}, \Phi) - P(\Theta, \Phi) \dot{\Phi} \quad (117) \dots 79$$

$$T = -B(\Theta, \dot{\Theta}, \Phi) - D(\Theta, \Phi) \dot{\Phi} \quad (118) \dots 79$$

$$\sum_{i=1}^N (m_i \mathbf{a}_i - \mathbf{F}_i^a) \cdot \frac{\partial \mathbf{v}_i}{\partial \dot{q}_k} + \sum_{i=1}^N (\dot{\mathbf{H}}_i - \mathbf{M}_i^a) \cdot \frac{\partial \boldsymbol{\omega}_i}{\partial \dot{q}_k} = 0 \quad (119) \dots 87$$

$$A(\ddot{\theta}, \dot{\theta}, \theta, t) - T_j = 0 \quad (120) \dots 88$$

$$A(\ddot{\theta}, \dot{\theta}, \theta, t) - \mathbf{B}(\theta) T_c = 0 \quad (121) \dots 88$$

$$\mathbf{T}_j = \mathbf{B}(\theta)\mathbf{T}_c \quad (122) \dots 88$$

$$\frac{\partial \boldsymbol{\omega}_i}{\partial \dot{q}_k} = \begin{cases} \hat{\mathbf{t}}_k & k \leq i \\ 0 & k > i \end{cases} \quad (123) \dots 88$$

$$\mathbf{M}_{j,i}^a = \tau_{j,i} \hat{\mathbf{t}}_i - \tau_{j,i+1} \hat{\mathbf{t}}_{i+1} \quad (124) \dots 89$$

$$\sum_{i=1}^N \mathbf{M}_{j,i}^a \cdot \frac{\partial \boldsymbol{\omega}_i}{\partial \dot{q}_k} = \sum_{i=k}^N \left\{ (\tau_{j,i} \hat{\mathbf{t}}_i - \tau_{j,i+1} \hat{\mathbf{t}}_{i+1}) \cdot \hat{\mathbf{t}}_k \right\} \quad (125) \dots 89$$

$$\sum_{i=1}^N \mathbf{M}_{j,i}^a \cdot \frac{\partial \boldsymbol{\omega}_i}{\partial \dot{q}_k} = \tau_{j,k} \quad (126) \dots 89$$

$$\mathbf{M}_{c,i}^a = \tau_{c,i} \hat{\mathbf{t}}_i \quad (127) \dots 89$$

$$\sum_{i=1}^N \mathbf{M}_{c,i}^a \cdot \frac{\partial \boldsymbol{\omega}_i}{\partial \dot{q}_k} = \sum_{i=k}^N \tau_{c,i} \hat{\mathbf{t}}_i \cdot \hat{\mathbf{t}}_k \quad (128) \dots 89$$

$$\sum_{i=1}^N \mathbf{M}_{c,i}^a \cdot \frac{\partial \boldsymbol{\omega}_i}{\partial \dot{q}_k} = \begin{bmatrix} 1 & \hat{\mathbf{t}}_1 \cdot \hat{\mathbf{t}}_2 & \hat{\mathbf{t}}_1 \cdot \hat{\mathbf{t}}_3 \\ 0 & 1 & \hat{\mathbf{t}}_2 \cdot \hat{\mathbf{t}}_3 \\ 0 & 0 & 1 \end{bmatrix} \cdot \begin{bmatrix} \tau_{c1} \\ \tau_{c2} \\ \tau_{c3} \end{bmatrix} \quad (129) \dots 89$$

$$\mathbf{A}(\ddot{\theta}, \dot{\theta}, \theta, t) - \mathbf{B}(\theta)\mathbf{T}_c^* - \mathbf{T}_j^* = 0 \quad (130) \dots 90$$

$$\mathbf{T}_j^* = \text{diag}(\alpha_i)\mathbf{T}_j \quad (131) \dots 90$$

$$\mathbf{B}(\theta)\mathbf{T}_c^* = (\mathbf{I} - \text{diag}(\alpha_i))\mathbf{T}_j \quad (132) \dots 90$$

$$\begin{bmatrix} \dot{\theta}_{c1} \\ \dot{\theta}_{c2} \\ \dot{\theta}_{c3} \end{bmatrix} = \begin{bmatrix} 1 & 0 & 0 \\ \hat{\mathbf{t}}_1 \cdot \hat{\mathbf{t}}_2 & 1 & 0 \\ \hat{\mathbf{t}}_1 \cdot \hat{\mathbf{t}}_3 & \hat{\mathbf{t}}_2 \cdot \hat{\mathbf{t}}_3 & 1 \end{bmatrix} \cdot \begin{bmatrix} \dot{\theta}_1 \\ \dot{\theta}_2 \\ \dot{\theta}_3 \end{bmatrix} \quad (133) \dots 91$$

$$\dot{\boldsymbol{\theta}}_c = \mathbf{B}^T \dot{\boldsymbol{\theta}}_j \quad (134) \dots 91$$

$$P_{j,C} = \dot{\boldsymbol{\theta}}_j \cdot \mathbf{T}_j \quad (135) \dots 92$$

$$P_{c,C} = \dot{\boldsymbol{\theta}}_c \cdot \mathbf{T}_c \quad (136) \dots 92$$

$$P_{c,C} = \mathbf{\Theta}_j^T \mathbf{B} \mathbf{B}^{-1} \mathbf{T}_j \quad (137) \dots 92$$

$$P_j = \sum_{i=1}^N |\tau_{j,i} \dot{\theta}_i| \quad (138) \dots 92$$

$$P_c = \sum_{i=1}^N |\tau_{c,i} \dot{\theta}_{c,i}| \quad (139) \dots 92$$

$$P_H = \sum_{i=1}^N |(1-\alpha) \tau_{c,i} \dot{\theta}_{c,i}| + \sum_{i=1}^N |\alpha \tau_{j,i} \dot{\theta}_i| \quad (140) \dots 93$$

$$P_c = |(\tau_{j1} - \tau_{j2}) \dot{\theta}_1| + |\tau_{j2} (\dot{\theta}_1 + \dot{\theta}_2)| \quad (141) \dots 93$$

$$P_{j,i} = \tau_{j,i} \dot{\theta}_i \quad (142) \dots 94$$

$$P_c = |P_{j1} - \tau_{j2} \dot{\theta}_1| + |P_{j2} + \tau_{j2} \dot{\theta}_2| \quad (143) \dots 94$$

$$P_H = |(1-\alpha_1) \tau_{j1} \dot{\theta}_1 + c_1| + |\alpha_1 \tau_{j1} \dot{\theta}_1| + c_2 \quad (144) \dots 95$$

$$P_H \geq |(1-\alpha_1) \tau_{j1} \dot{\theta}_1 + c_1 + \alpha_1 \tau_{j1} \dot{\theta}_1| + c_2 \quad (145) \dots 96$$

$$E_x = \int P_x \quad (146) \dots 96$$

$$P_H = \min_{\alpha_2} |\tau_{j1} \dot{\theta}_1 - (1-\alpha_2) \tau_{j2} \dot{\theta}_1| \quad (148) \dots 97$$

$$+ |(1-\alpha_2) \tau_{j2} (\dot{\theta}_1 + \dot{\theta}_2)| + |\alpha_2 \tau_{j2} \dot{\theta}_2|$$

$$\alpha_2 = 1 - \tau_{j1} / \tau_{j2} \quad (149) \dots 97$$

$$P_H = \min_{\alpha_2, \alpha_3} |\tau_1 \dot{\theta}_1 - (1-\alpha_2) \tau_2 \dot{\theta}_1| \quad (150) \dots 101$$

$$+ |[(1-\alpha_2) \tau_2 - (1-\alpha_3) \tau_3] (\dot{\theta}_1 + \dot{\theta}_2)|$$

$$+ |(1-\alpha_3) \tau_3 (\dot{\theta}_1 + \dot{\theta}_2 + \dot{\theta}_3)| + |\alpha_2 \tau_2 \dot{\theta}_2| + |\alpha_3 \tau_3 \dot{\theta}_3|.$$

$$I_i = m_i \cdot l_i^2 / 12 \quad (151) \dots 102$$

REFERENCES

- Albertos, P. and A. Salas (2004), *Multivariable Control Systems : An Engineering Approach*, Advanced Textbooks in Control and Signal Processing, 340-76 pp., Springer, London.
- Alexander, R. M. N. (1997), A minimum energy cost hypothesis for human arm trajectories, *Biol. Cybern.*, 76, 97-105.
- Aubrun, J. N. and G. Margulies (1979), Gyrodampers for Large Space Structures, 159171.
- Bar-Cohen, Y. (2004), *Electroactive Polymer (EAP) Actuators as Artificial Muscles: Reality, Potential, and Challenges*, SPIE Press.
- Bedford, A. and W. L. Fowler (2005), *Engineering Mechanics: Dynamics*, 4th ed. ed., 622-431 pp., Pearson Prentice Hall, Upper Saddle River, N.J.
- Bedrossian, N. S., J. Paradiso, E. V. Bergmann, and D. Rowell (1990), Steering Law Design for Redundant Single-Gimbal Control Moment Gyroscopes, *Journal of Guidance, Control, and Dynamics*, 13, 1083–1089.
- Berkowitz, K. (2008), Weightless Wonder: Cornell students test new robotic arm in NASA's "Vomit Comet", *Cornell Engineering Magazine*, 6-11.
- Billing-Ross, J. A. and J. F. Wilson (1988), Pointing System Design for Low-Disturbance Performance, AIAA Guidance, Navigation, and Control Conference, Minneapolis, MN, Aug. 15-17, 1988.
- Brennan, L. (1903), Improvements in and Relating to the Imparting of Stability to otherwise Unstable Bodies, Structures or Vehicles.
- Brennan, L. (1905), Means for Imparting Stability to Unstable Bodies.
- Brown, D. and M. A. Peck (in review), Control Moment Gyros as Space-Robotics Actuators, *Journal of Guidance, Control, and Dynamics*.
- Brown, D. and M. A. Peck (2008), Scissored-Pair Control Moment Gyros: A Mechanical Constraint Saves Power, *Journal of Guidance, Control, and Dynamics*, 31, 1823-1826.
- Carpenter, M. D. and M. A. Peck (2008), Dynamics of a High-Agility, Low-Power Imaging Payload, *IEEE Transactions on Robotics*, 24, 666-675.

- Carpenter, M. D. and M. A. Peck (in review), Reducing base reactions with gyroscopic actuation of robotic systems, *IEEE Transactions on Robotics*.
- Cornell CMG Team (2006), CMG Research Project: Spring Project Report, http://www.mae.cornell.edu/cmgi/media/Spring_2006_Report.pdf.
- Cornell CMG Team (2007), CMG Research Team: Final Report, <http://www.mae.cornell.edu/cmgi/media/Spring2007Report.pdf>.
- Craig, J. J., 1955- (2005), *Introduction to Robotics : Mechanics and Control*, 3rd ed. ed., 400 pp., Pearson Education, Upper Saddle River, N.J.
- Cunningham, D. C. and G. W. Driskill (1972), A Torque Balance Control Moment Gyroscope Assembly for Astronaut Maneuvering, NASA Ames Research Center 6th Aerospace Mechanisms Symposium.
- Duindam, V. and S. Stramigioli (2008), Singularity-Free Dynamic Equations of Open-Chain Mechanisms With General Holonomic and Nonholonomic Joints, *Robotics, IEEE Transactions on [see also Robotics and Automation, IEEE Transactions on]*, 24, 517-526.
- Elgersma, M. R., D. P. Johnson, M. A. Peck, B. K. Underhill, G. Stein, B. G. Morton, and B. J. Hamilton (2007), Method and System for Controlling Sets of Collinear Control Moment Gyroscopes, *20070124032 A1*.
- Hall, J. S. (2006), Design and Integration of a Three Degrees-of-Freedom Robotic Vehicle with Control Moment Gyro for the Autonomous Multi-Agent Physically Interacting Spacecraft (AMPHIS) Testbed, MS thesis, Naval Postgraduate School, Monterey, CA.
- Havill, J. R. and J. W. Ratcliff (1964), A Twin-Gyro Attitude Control System for Space Vehicles, *Tech. Rep. NASA TN D-2419*.
- Jung, D. and P. Tsiotras (2003), A 3-DoF Experimental Test-Bed for Integrated Attitude Dynamics and Control Research, AIAA Guidance, Navigation and Control Conference.
- Kane, T. R. and D. A. Levinson (1985), *Dynamics: Theory and Applications*, McGraw-Hill, New York.
- Kim, K. J. and S. Tadokoro (2007), *Electroactive Polymers for Robotic Applications : Artificial Muscles and Sensors; Electroactive Polymers for Robotics Applications*, 281 pp., Springer, London.

- Koh, S. K., J. P. Ostrowski, and G. K. Ananthasuresh (2002), Control of Micro-Satellite Orientation Using Bounded-Input, Fully-Reversed MEMS Actuators, *The International Journal of Robotics Research*, 21, 591.
- Kurokawa, H. (2007), Survey of Theory and Steering Laws of Single-Gimbal Control Moment Gyros, *Journal of Guidance, Control, and Dynamics*, 30.
- Lappas, V. J., W. H. Steyn, and C. I. Underwood (2002), Attitude Control for Small Satellites Using Control Moment Gyros, *Acta Astronaut.*, 51, 101-111.
- Lappas, V., W. H. Steyn, and C. Underwood (2005), Design and Testing of a Control Moment Gyroscope Cluster for Small Satellites, *J. Spacecraft Rockets*, 42, 729.
- Lappas, V. J., W. H. Steyn, and C. I. Underwood (2002), Torque Amplification of Control Moment Gyros, *Electron. Lett.*, 38, 837-839.
- Liden, S. P. (1974), Precision CMG Control for High-Accuracy Pointing, *J. Spacecraft Rockets*, 11, 236.
- Liska, D. (1968), A Two-Degree-of-Freedom Control Moment Gyro for High-Accuracy Attitude Control, *Journal of Spacecraft and Rockets*, 5, 74-83.
- Longman, R. W., R. E. Lindberg, and M. F. Zedd (1987), Satellite-Mounted Robot Manipulators--New Kinematics and Reaction Moment Compensation, *International Journal of Robotics Research*, 6, 87-103.
- Margulies, G. and J. N. Aubrun (1978), Geometric Theory of Single-Gimbal Control Moment Gyro Systems, *J. Astronaut. Sci.*, 26, 159-191.
- Maruo, S., K. Ikuta, and H. Korogi (2003), Force-controllable, optically driven micromachines fabricated by single-step two-photon microstereolithography, *Microelectromechanical Systems, Journal of*, 12, 533-539.
- Mita, M., M. Arai, S. Tensaka, D. Kobayashi, and H. Fujita (2003), A micromachined impact microactuator driven by electrostatic force, *Microelectromechanical Systems, Journal of*, 12, 37-41.
- Moon, F. C. (1998), *Applied Dynamics: With Applications to Multibody and Mechatronic Systems*, 269-271 pp., Wiley, New York.
- Moosavian, S. A. A. and E. Papadopoulos (2007), Free-flying robots in space: an overview of dynamics modeling, planning and control, *Robotica*, 25, 537-547.
- Murray, R. M., Z. Li, and S. Sastry (1994), *A Mathematical Introduction to Robotic Manipulation; Robotic Manipulation.*, 456-293-296 pp., CRC Press, Boca Raton.

- Murtagh, T. B., C. E. Whitsett, M. A. Goodwin, and J. E. Greenlee (1974), Automatic Control of the Skylab Astronaut Maneuvering Research Vehicle, *J. Spacecraft Rockets*, 11, 321-326.
- Nakamura, Y. and R. Mukherjee (1991), Nonholonomic path planning of space robots via a bidirectional approach, *IEEE Transactions on Robotics and Automation*, 7, 500-514.
- Notti, J. E., A. Cormack, and W. J. Klein (1975), Integrated Power and Attitude Control with Spacecraft Flywheels and Control Moment Gyroscopes, *J. Spacecraft Rockets*, 12, 485-491.
- Oh, H. S., S. R. Vadali, and J. L. Junkins (1992), Use of the Work-Energy Rate Principle for Designing Feedback Control Laws, *Journal of Guidance, Control, and Dynamics*, 15, 275-277.
- Osuka, K., K. Yoshida, and T. Ono (1994), New Design Concept of Space Manipulator: A Proposal of Torque-Unit Manipulator, 33rd IEEE Conference on Decision and Control, Lake Buena Vista, Florida, December 1994.
- Parviz, B. A., T. - Allen Chou, C. Zhang, K. Najafi, M. O. Muller, P. D. Washabaugh, and L. P. Bernal (2001), Performance of ultrasonic electrostatic resonators for use in micro propulsion, *Micro Electro Mechanical Systems, 2001. MEMS 2001. The 14th IEEE International Conference on*, 586-589.
- Peck, M. A. (2005), Low-Power, High-Agility Space Robotics, AIAA Guidance, Navigation, and Control Conference, San Francisco, CA.
- Peck, M. A. (2006), Uncertainty Models for Physically Realizable Inertia Dyadics, *The Journal of the Astronautical Sciences*, 54.
- Peck, M. A. and A. R. Cavender (2004), Practicable Gyroelastic Technology, AAS Guidance Control Conference, Breckinridge, Colorado, February 2004.
- Peck, M. A., M. A. Paluszek, S. J. Thomas, and J. B. Mueller (2005), Control-Moment Gyroscopes for Joint Actuation: A New Paradigm in Space Robotics, AIAA 1st Space Exploraton Conference: Continuing the Voyage of Discovery.
- Roithmayr, C. M., C. D. Karlgaard, R. R. Kumar, and D. M. Bose (2004), Integrated Power and Attitude Control with Spacecraft Flywheels and Control Moment Gyroscopes, *JOURNAL OF GUIDANCE CONTROL AND DYNAMICS*, 27, 859-873.
- Romano, M. and B. N. Agrawal (2004), Attitude Dynamics/Control of Dual-Body Spacecraft with Variable-Speed Control Moment Gyros, *Journal of Guidance, Control, and Dynamics*, 27, 513-525.

- Schaub, H., S. R. Vadali, and J. L. Junkins (1998), Feedback control law for variable speed control moment gyros, *J. Astronaut. Sci.*, 46, 307-328.
- Schaub, H. and J. L. Junkins (2003), *Analytical Mechanics of Space Systems*, 438-440 pp., American Institute of Aeronautics and Astronautics, Inc., Reston, Virginia.
- Schwartz, J. L., M. A. Peck, and C. D. Hall (2003), Historical Review of Air-Bearing Spacecraft Simulators, *JOURNAL OF GUIDANCE CONTROL AND DYNAMICS*, 26, 513-522.
- Shanno, D. F. and R. L. Weil (1971), 'Linear' Programming with Absolute-Value Functionals, *Operations Research*, 19, 120-124.
- Thornton, B., T. Ura, Y. Nose, and S. Turnock (2005), Internal actuation of underwater robots using control moment gyros, *Oceans-Europe*, 1, 591-598.
- Vadali, S. R., S. R. Walker, and H. S. Oh (1990), Preferred Gimbal Angles for Single Gimbal Control Moment Gyros, *Journal of Guidance, Control, and Dynamics*, 13, 1090-1095.
- van Ingen Schenau, G. J., M. F. Bobbert, and R. H. Rozendal (1987), The unique action of bi-articular muscles in complex movements., *J. Anat.*, 155, 1-5.
- Van Riper, R. V. and S. P. Liden (1971), A New Fail Operational Control Moment Gyro Configuration, AIAA Guidance, Control, and Flight Mechanics Conference.
- Webster III, R. J., J. S. Kim, N. J. Cowan, G. S. Chirikjian, and A. M. Okamura (2006), Nonholonomic Modeling of Needle Steering, *Int. J. Robotics Res.*, 25, 509-525.
- Wie, B., D. Bailey, and C. Heiberg (2002), Rapid Multitarget Acquisition and Pointing Control of Agile Spacecraft, *Journal of Guidance, Control, and Dynamics*, 25, 96-104.
- Yang, L. F. and W. H. Chang (1996), Synchronization of Twin-Gyro Precession Under Cross-Coupled Adaptive Feedforward Control, *Journal of Guidance, Control, and Dynamics*, 19, 534-539.
- Yang, L. F., M. M. Mikulas Jr, K. C. Park, and R. Su (1995), Slewing Maneuvers and Vibration Control of Space Structures by Feedforward/Feedback Moment-Gyro Controls, *Journal of dynamic systems, measurement, and control*, 117, 343-351.